



UNIVERSITATEA DIN BUCUREŞTI
Facultatea de Fizică



Mircea DOLINEANU

**Studies of Laser Wakefield Acceleration and γ -Ray
Generation by Laser-Irradiated Structured Targets
using Particle-in-Cell Numerical Simulations**

BACHELOR THESIS

Scientific Advisers
Conf. dr. Alexandru NICOLIN
Dr. Carina Mihaela RAPORTARU, IFIN-HH

Bucharest, 2020

Contents

Introduction	1
1 Electromagnetism and Laser Profiles	3
1.1 Classical Electrodynamics	3
1.1.1 Maxwell's Equations	3
1.1.2 The Scalar and Vector Potentials	4
1.1.3 Gauge Transformation	5
1.1.4 The Poynting Theorem	6
1.1.5 Momentum of a System of Fields and Field Sources	10
1.2 Electromagnetic Waves	11
1.2.1 Maxwell's Equations in Vacuum	12
1.2.2 Plane Waves	13
1.2.3 Paraxial Approximation	15
1.2.4 Gaussian Beams	16
1.2.5 Gaussian Beam Packets	19
1.2.6 Laguerre-Gauss Beams	24
1.2.7 Other Types of Beams	27
1.3 Angular Momentum of Electromagnetic Waves	28
2 The Interaction Between Electromagnetic Radiation and Matter	29
2.1 Electron Dynamics in Electromagnetic Fields	29
2.1.1 Classical Treatment	29
2.1.2 Relativistic Treatment	31
2.2 The Ponderomotive Force	36
2.2.1 Classical Derivation	36
2.2.2 Relativistic Ponderomotive Force	37
3 Plasma Physics	41
3.1 The Definition of Plasma	41
3.2 Temperature	42
3.3 Debye Shielding	43
3.4 Plasma Frequency	44
3.5 Electromagnetic Waves in Plasma	46
3.6 The Vlasov Equation	47
3.7 Two Stream Instability	50
3.8 Laser Wakefield Acceleration	55

4 Numerical Methods and Particle in Cell Simulations	56
4.1 Numerical Methods	56
4.1.1 Introduction to Numerical Methods for Solving Differential Equations . .	56
4.1.2 One-Step Methods	57
4.1.3 Error Estimation	58
4.1.4 Runge-Kutta Methods	59
4.1.5 Leapfrog Algorithm	59
4.1.6 Stability	61
4.2 The Relevant Equations	66
4.2.1 The Connection with the Vlasov Equation	67
4.3 Methods used in Particle-in-cell simulations	68
4.3.1 The Boris Push	68
4.3.2 Symplecticity and Volume Conservation Theory	71
4.3.3 Conservation Properties of the Boris push	74
4.3.4 The FDTD Maxwell Solver	76
4.3.5 Stability of the FDTD Scheme	79
4.4 Particle-in-cell in Practice	80
4.4.1 Conditions and Restrictions for a Successful Simulation	81
4.4.2 Currently Available PIC Codes and High Performance Computing	82
4.5 EPOCH	83
4.5.1 Software Input	83
5 Results	84
5.1 Low intensity laser simulations	84
5.2 Higher intensity laser simulations	93
5.3 Structured targets	100
6 Conclusions	105
Appendix	106
Bibliography	120

Introduction

Taking into consideration the new innovations in laser technology and the infrastructures built in the past couple of years to make these available for experimental use, it is now an important time to study and understand the applications that will become more accessible and greatly improvable in this context, as well as the physical processes, new or old, that we will be able to study. The motivation for this work is the development of the Extreme Light Infrastructure for Nuclear Physics (ELI-NP) facility, which is at the moment being finalized within the “Horia Hulubei” National Institute for Physics and Nuclear Engineering together with the other two ELI facilities in the Czech Republic and Hungary, all three of which host PW-level laser infrastructures. In particular, on one hand, we are interested in the projects related to laser wakefield acceleration (LWFA) using laser-plasma interaction to accelerate electron beams. Such experiments are greatly anticipated, since at the intensities achievable with the new infrastructure, QED effects are relevant (Tanaka *et al.* 2020), and there will be a chance to test various QED theories as well as a possibility to discover new physics. On the second hand, there is also a promising alternative that uses overdense structured plasma targets to generate photon beams through synchrotron emission. For these purposes, a good understanding of laser-matter interaction together with specific aspects of LWFA is necessary in order to design good experiments and efficiently analyze the results. A powerful tool in this regard are numerical simulations, or particular to this field of research, Particle-in-Cell codes. These are readily available large scale software that have been used for decades to study plasma related phenomena. We chose to use EPOCH (Arber *et al.* 2015), which is one of the codes that implements multiple ionization mechanisms and has also QED routines available for use.

In this thesis, after a comprehensive theoretical presentation and after explaining the inner workings and the validity of the numerical method used, we study the fundamentals of LWFA and offer results from simulations that aim to do a comparative study of using different laser profiles, the main focus being the Laguerre-Gauss modes. We will also present the use of structured targets together with normal Gaussian lasers through a couple simulations concerning the study of the photon yield as a function of target geometry. In the first chapter we shortly review basic concepts of electromagnetism and electromagnetic wave theory in order to end up studying the mathematical approaches to modeling laser beams. In the second chapter we discuss light-matter interaction with a great focus on the ponderomotive force, an essential piece in the explanation of LWFA. The third chapter is solely dedicated to understanding plasma specific mechanisms, and provides a few examples. In the fourth chapter we discuss the basic notions regarding numerical simulations of physical systems and then we particularize the ideas in the concrete case of the Particle-in-Cell method. The fifth chapter covers our numerical simulations and results. Finally, we provide a short conclusive chapter that aims to summarize the results obtained. An appendix is added containing various codes used for small numerical studies made along the way in the more theoretical chapters as well as the EPOCH input files used for the simulations presented in the results chapter.

Acknowledgments

I would like to thank my adviser, Conf. Dr. Alexandru Nicolin, for his help and support, and for providing me with the tools, the resources and the proper environment that I needed for accomplishing my work. The simulations were performed using the computing cluster at Department of Computational Physics and Information Technologies of the National Institute of Physics and Nuclear Engineering in close collaboration with Dr. Mihaela Carina Raportaru. I would also like to thank the PhD student Sebastian Micluță-Câmpeanu, whithout the help and assistance of whom I would have been lost in the plethora of technical difficulties I have encountered along the way. I also must thank Lect. Dr. Mădălina Boca and Conf. Dr. Mihai Dondera for the fuitful discussions I had with them, which helped me better understand the mathematics and physics behind laser wave modeling.

Chapter 1

Electromagnetism and Laser Profiles

1.1 Classical Electrodynamics

The main principles and laws that govern the phenomena behind lasers, plasma and their interaction are those of classical electrodynamics. As such, like many others tackling this area of research, I find that adding an overview of electrodynamics is simply mandatory. My aim when it comes to differentiating this introductory review from the millions of others out there, if at all possible, is to offer thorough calculations and explanations on some aspects where I personally felt like I wanted to see things from a clearer perspective.

1.1.1 Maxwell's Equations

The Maxwell equations are (Jackson 1999):

$$\nabla \cdot \mathbf{D} = \rho \quad (1.1a)$$

$$\nabla \cdot \mathbf{B} = 0 \quad (1.1b)$$

$$\nabla \times \mathbf{E} = -\frac{\partial \mathbf{B}}{\partial t} \quad (1.1c)$$

$$\nabla \times \mathbf{H} = \mathbf{j} + \frac{\partial \mathbf{D}}{\partial t}. \quad (1.1d)$$

In the absence of magnetic and polarizable media, $\mathbf{D} = \epsilon_0 \mathbf{E}$ and $\mathbf{B} = \mu_0 \mathbf{H}$ these equations become:

$$\nabla \cdot \mathbf{E} = \frac{\rho}{\epsilon_0} \quad (1.2a)$$

$$\nabla \cdot \mathbf{B} = 0 \quad (1.2b)$$

$$\nabla \times \mathbf{E} = -\frac{\partial \mathbf{B}}{\partial t} \quad (1.2c)$$

$$\nabla \times \mathbf{B} = \mu_0 \mathbf{j} + \frac{1}{c^2} \frac{\partial \mathbf{E}}{\partial t}, \quad (1.2d)$$

While most readers probably already had at least a basic introduction to the phenomena from which these equations arise and are well endowed with the practical use of these equations, I would direct those who haven't towards the book by Fleisch 2008.

By extracting the current density from equation (1.2d), computing its divergence and then replacing the electric field term using equation (1.2a), one obtains the continuity equation, which relates only the field sources to one another:

$$\nabla \cdot \mathbf{j}(\mathbf{r}, t) + \frac{\partial \rho(\mathbf{r}, t)}{\partial t} = 0. \quad (1.3)$$

These equations are also complemented by the Lorentz force, which describes how the fields act on the sources. The expression of the Lorentz force in the continuous case is:

$$\mathbf{F} = \int_{\mathcal{V}} d\mathbf{r}' \left[\rho(\mathbf{r}', t) \mathbf{E}(\mathbf{r}', t) + \frac{1}{c} \mathbf{j}(\mathbf{r}', t) \times \mathbf{B}(\mathbf{r}', t) \right].$$

1.1.2 The Scalar and Vector Potentials

Since the electric (**E**) and magnetic (**B**) fields are vectors, they can be described together by a total of six quantities. The sources on the other hand can be described using only four quantities: the electric charge density ρ and the three components of the electric current density \mathbf{j} . This points to the fact that there is a more convenient way to describe the fields. In finding this alternative, we shall employ the following basic results from algebra:

$$\nabla \cdot (\nabla \times \mathbf{v}) = 0 \quad (1.4a)$$

$$\nabla \times (\nabla \cdot \mathbf{v}) = 0 \quad (1.4b)$$

$$\nabla \times (\nabla f) = 0, \quad (1.4c)$$

which are valid for any vector function \mathbf{v} and for any scalar function f .

From equations (1.2b) and (1.4a), one can define the vector potential **A** such that

$$\mathbf{B}(\mathbf{r}, t) = \nabla \times \mathbf{A}(\mathbf{r}, t). \quad (1.5)$$

By substituting (1.5) in (1.2c) one obtains

$$\nabla \times \left(\mathbf{E} + \frac{\partial \mathbf{A}}{\partial t} \right) = 0 \quad (1.6)$$

which together with equation (1.4c) defines the scalar potential ϕ

$$\nabla \phi(\mathbf{r}, t) = -\mathbf{E}(\mathbf{r}, t) - \frac{\partial \mathbf{A}}{\partial t}. \quad (1.7)$$

Using this in equation (1.2a)

$$\nabla^2 \phi + \frac{\partial}{\partial t} \nabla \cdot \mathbf{A} = -\frac{\rho}{\epsilon_0}. \quad (1.8)$$

Similarly, using equation (1.7) in equation (1.2d) and making use of the following vector identity

$$\nabla \times (\nabla \times \mathbf{v}) = \nabla(\nabla \cdot \mathbf{v}) - \nabla^2 \mathbf{v}, \quad (1.9)$$

another equation for the potentials is obtained

$$\nabla^2 \mathbf{A} - \frac{1}{c^2} \frac{\partial^2 \mathbf{A}}{\partial t^2} = -\mu_0 \mathbf{j} + \nabla \left(\nabla \cdot \mathbf{A} + \frac{1}{c^2} \frac{\partial \phi}{\partial t} \right). \quad (1.10)$$

Considering that at every step in the derivation of equations (1.8) and (1.10) we only imposed the Maxwell equations and basic algebraic identities, it follows that equations (1.8)

and (1.10) and equation (1.2) are completely equivalent. We now have reduced the six quantities describing the fields to only four: the scalar potential ϕ and the three components of the vector potential \mathbf{A} . This description of the fields through the potentials is quite useful since it is easily integrated in the formalism of special relativity. One can define the electromagnetic potential 4-vector such that the scalar field is the time-like component and the vector field is the space-like component.

In general, when studying the dynamics of particles in an electromagnetic field, once the potentials are computed using equations (1.8) and (1.10) the fields are obtained from equations (1.5) and (1.7) and can be used further in the expression of the Lorentz force.

1.1.3 Gauge Transformation

By a direct application of equation (1.4) one can show that a simultaneous transformation by an arbitrary well-behaved (continuous with continuous derivatives) scalar function $f = f(\mathbf{r}, t)$ of the potentials:

$$\phi \rightarrow \phi + \frac{\partial f}{\partial t} \quad (1.11a)$$

$$\mathbf{A} \rightarrow \mathbf{A} - \nabla f, \quad (1.11b)$$

leaves the electric and magnetic fields unchanged. This is actually a quite natural equivalent of the intuitive fact that any potential is defined up to a constant. In the particular case of the electromagnetic potential, equation (1.11) defines a gauge transformation. There are two widely used gauges:

Lorenz gauge

$$\nabla \cdot \mathbf{A} + \frac{1}{c^2} \frac{\partial \phi}{\partial t} = 0 \quad (1.12)$$

This gauge cancels the gradient in equation (1.10). If one works in the usual Mikovski metric (Weinberg 1972)

$$\eta_{\mu\nu} = \begin{pmatrix} -1 & 0 & 0 & 0 \\ 0 & 1 & 0 & 0 \\ 0 & 0 & 1 & 0 \\ 0 & 0 & 0 & 1 \end{pmatrix} \quad (1.13)$$

the d'Alembert operator is then defined as

$$\square = \partial^\mu \partial_\mu = \eta^{\mu\nu} \partial_\nu \partial_\mu = \nabla^2 - \frac{1}{c^2} \frac{\partial^2}{\partial t^2},$$

where $\mu, \nu = \overline{0, 3}$ with 0 being the temporal index and 1, 2, 3 being the spatial indices (note: in this thesis I use Einstein's summation convention whenever there is an index repeated once up and down, *i.e.* it appears as both variant and covariant in a product). By replacing this definition in equations (1.8) and (1.10), it is easy to see that both \mathbf{A} and ϕ obey a free wave equation:

$$\square \mathbf{A} = -\mu_0 \mathbf{j} \quad (1.14a)$$

$$\square \phi = -\frac{\rho}{\varepsilon_0}. \quad (1.14b)$$

Coulomb Gauge (sometimes found as transversal/velocity gauge)

$$\nabla \cdot \mathbf{A} = 0 \quad (1.15)$$

Under this gauge, the potential equations (1.8) and (1.10) take the form:

$$\square \mathbf{A} = -\mu_0 \mathbf{j} + \frac{1}{c^2} \nabla \frac{\partial \phi}{\partial t} \quad (1.16a)$$

$$\nabla^2 \phi = -\frac{\rho}{\epsilon_0}. \quad (1.16b)$$

Getting Back the Fields

In principle, one can choose the most convenient gauge for his system, solve the corresponding potential equations, then recover the electric and magnetic fields with

$$\mathbf{E} = -\frac{\partial \mathbf{A}}{\partial t} - \nabla \phi \quad (1.17a)$$

$$\mathbf{B} = \nabla \times \mathbf{A}. \quad (1.17b)$$

1.1.4 The Poynting Theorem

The Poynting theorem is the form of the conservation of energy in the case of electromagnetic fields interacting with charges and currents. Since it is such an important and general result, this presentation of it will start from the more general form of the Maxwell equations(see equation (1.1)).

In the derivation of this theorem, one usually starts from the local form of the Lorentz force (Griffiths 1999):

$$\mathbf{F} = \delta q \mathbf{E} + \delta q \mathbf{v} \times \mathbf{B}$$

The work done by the electric field part of the force on the volume element with charge δq and velocity $\mathbf{v} = \frac{d\mathbf{l}}{dt}$ is

$$dW_e = q d\mathbf{l} \cdot \mathbf{E}$$

and the corresponding rate of work done is

$$\frac{dW_e}{dt} = q \mathbf{v} \cdot \mathbf{E}$$

while for the magnetic part we have (as expected)

$$dW_m = d\mathbf{l} \cdot \mathbf{F}_b = q d\mathbf{l} \cdot (\mathbf{v} \times \mathbf{B})$$

$$\frac{dW_b}{dt} = q \mathbf{v} \cdot (\mathbf{v} \times \mathbf{B}) = 0.$$

Adding these contributions and generalizing for the case of a distribution of charges and currents one obtains

$$\frac{dW}{dt} = \int_V d\mathbf{r} \mathbf{E} \cdot \mathbf{j} \quad (1.18)$$

By extracting \mathbf{j} from equation (1.1d) and replacing in the above equation we have

$$\frac{dW}{dt} = \int_V d\mathbf{r} \left[\mathbf{E} \cdot (\nabla \times \mathbf{H}) - \mathbf{E} \cdot \frac{\partial \mathbf{D}}{\partial t} \right]$$

Employing here the vector identity

$$\nabla(\mathbf{u} \times \mathbf{v}) = \mathbf{v} \cdot (\nabla \times \mathbf{u}) - \mathbf{u} \cdot (\nabla \times \mathbf{v}) \quad (1.19)$$

gives

$$\frac{dW}{dt} = \int_V d\mathbf{r} \left[\mathbf{H} \cdot (\nabla \times \mathbf{E}) - \nabla(\mathbf{E} \times \mathbf{H}) - \mathbf{E} \cdot \frac{\partial \mathbf{D}}{\partial t} \right].$$

Replacing the curl of \mathbf{E} using Faraday's law (1.1c) we finally obtain

$$\frac{dW}{dt} = - \int_V d\mathbf{r} \left[\nabla(\mathbf{E} \times \mathbf{H}) + \mathbf{E} \cdot \frac{\partial \mathbf{D}}{\partial t} + \mathbf{H} \cdot \frac{\partial \mathbf{B}}{\partial t} \right].$$

If we restrict the discussion now only to linear media (*i.e.* $\mathbf{D} = \epsilon \mathbf{E}$ and $\mathbf{B} = \mu \mathbf{H}$) a new important quantity can be defined

$$w_{em} = \frac{1}{2} (\mathbf{E} \cdot \mathbf{D} + \mathbf{H} \cdot \mathbf{B}) \quad (1.20)$$

which leads to a new way to write the expression of the rate of work done by the electromagnetic field

$$\frac{dW}{dt} = - \int_V d\mathbf{r} \left[\nabla(\mathbf{E} \times \mathbf{H}) + \frac{\partial w_{em}}{\partial t} \right], \quad (1.21)$$

where the Poynting vector is defined to be

$$\mathbf{S} = \mathbf{E} \times \mathbf{H}. \quad (1.22)$$

In order to complete the derivation of Poynting's theorem, we can physically interpret the new quantities we introduced. As such, a short parenthesis concerning w_{em} is in order.

Electrostatic field energy density

For a system of N stationary point-like charged particles of charges q_i placed at \mathbf{r}_i , $i = \overline{1, N}$ in a medium with permittivity ϵ , the total potential energy of the system, when neglecting the infinite self-interaction terms, is (Jackson 1999)

$$W_e = \frac{1}{2} \sum_{i,j=1, i \neq j}^N \frac{q_i q_j}{4\pi \epsilon |\mathbf{r}_i - \mathbf{r}_j|}$$

or, factoring out the scalar potential $\phi(\mathbf{r}_i)$ generated by all the other particles at the position of particle i ,

$$W_e = \frac{1}{2} \sum_{i=1}^N q_i \phi(\mathbf{r}_i)$$

This is easily generalized in integral form

$$W_e = \frac{1}{2} \int_V d\mathbf{r} \rho(\mathbf{r}) \phi(\mathbf{r}),$$

where we use the delta-Dirac function for pointlike particles if needed.

Using the fact that the electrostatic potential is defined by $\mathbf{E} = -\nabla\phi$ and replacing this in equation (1.1a) one obtains the poisson equation

$$\nabla^2 \phi = -\frac{\rho}{\epsilon}. \quad (1.23)$$

With this, the integral above becomes

$$W_e = \frac{\epsilon}{2} \int_V d\mathbf{r} \phi \nabla^2 \phi = -\frac{\epsilon}{2} \int_V d\mathbf{r} \phi \nabla \phi + \frac{\epsilon}{2} \int_V d\mathbf{r} |\nabla \phi|^2,$$

where integration by parts has been used.

In order to reach the desired result, we still have to perform one more integration by parts

$$\int_V d\mathbf{r} \phi \nabla \phi = \frac{1}{2} \int_V d\mathbf{r} \nabla \phi^2 = \int_{S_V} d\mathbf{a} \phi^2,$$

where in the last step we used Gauss' theorem. Now, if we integrate over the entire space and keep in mind that the electrostatic potential should be zero at infinity, the above integral becomes null. Using again the relation between the gradient of the potential and the electric field we get

$$W_e = \frac{\epsilon}{2} \int_V d\mathbf{r} \mathbf{E}^2 \quad (1.24)$$

or, equivalently,

$$W_e = \frac{1}{2} \int_V d\mathbf{r} \mathbf{E} \cdot \mathbf{D}. \quad (1.25)$$

This leads to the definition of the energy density of the electrostatic field

$$w_e = \frac{1}{2} \mathbf{E} \cdot \mathbf{D}. \quad (1.26)$$

Magnetostatic field energy density

This time around we start with a current loop in the case of magnetostatics ($\nabla \cdot \mathbf{j} = 0$). No matter the current distribution in space, since the current density is rotational, we can always divide it in individual infinitesimal current loops. A change in the magnetic flux through such a loop is given by the integral form of Faraday's law (1.1c)

$$e = \oint_{\gamma} d\mathbf{l} \cdot \mathbf{E} = -\frac{d\phi_B}{dt}, \quad (1.27)$$

where γ is the closed curve describing the loop and ϕ_B is the magnetic flux through the loop.

Since the selfinduced magnetic flux is $\phi_B = LI$, where L is the inductance of the loop and I the intensity of the electric current flowing in it, the electromotive force caused by selfinduction is

$$e = -L \frac{dI}{dt}.$$

Thus, the rate of work done against the increasing of the current is

$$\frac{dW_B}{dt} = -Ie = LI \frac{dI}{dt} = \frac{d}{dt} \left(\frac{LI^2}{2} \right).$$

With this result we obtain the energy necessary to get a current of intensity I starting through a loop:

$$W_B = \frac{LI^2}{2}.$$

We will now eliminate L the same way we introduced it

$$\phi_B = LI = \int_{S_\gamma} d\mathbf{a} \cdot \mathbf{B} = \int_{S_\gamma} d\mathbf{a} \cdot (\nabla \times \mathbf{A}) = \oint_\gamma dl \cdot \mathbf{A},$$

where the vector potential was introduced and Stokes' theorem was applied.

$$W_B = \frac{1}{2} I \oint_\gamma dl \cdot \mathbf{A} = \frac{1}{2} \int_V d\mathbf{r} \mathbf{j} \cdot \mathbf{A}.$$

Here we naturally introduced the electric current density in our calculations. It can be replaced though using equation (1.1d) (we work in the confinements of magnetostatics, so there is no time dependent electric field)

$$W_B = \frac{1}{2} \int_V d\mathbf{r} \mathbf{A} \cdot (\nabla \times \mathbf{H}).$$

We employ here the identity (1.19) to reach

$$W_B = \frac{1}{2} \int_V d\mathbf{r} \mathbf{H} \cdot (\nabla \times \mathbf{A}) - \frac{1}{2} \int_V d\mathbf{r} \nabla \cdot (\mathbf{A} \times \mathbf{H}) = \frac{1}{2} \int_V d\mathbf{r} \mathbf{H} \cdot \mathbf{B} - \frac{1}{2} \int_{S_V} d\mathbf{a} \cdot (\mathbf{A} \times \mathbf{H}).$$

The same trick as in the previous subsection is applicable here. By extending the integration volume over the entire space and using the fact that the vector potential should be zero at infinity, the second integral vanishes:

$$W_B = \frac{1}{2} \int_V d\mathbf{r} \mathbf{H} \cdot \mathbf{B} \tag{1.28}$$

The energy density of the magnetostatic field is defined to be

$$w_B = \frac{1}{2} \mathbf{H} \cdot \mathbf{B}. \tag{1.29}$$

Interpretation of the Poynting theorem

We can see now that (1.20) is simply the sum of equation (1.26) and equation (1.29). Bringing together all the previous considerations, we conclude that w_{em} holds the meaning of the energy density of the electromagnetic field itself, that is, the energy density present in space due to the presence of the electric and magnetic fields.

The Poynting theorem (1.21) can be rewritten using Gauss' theorem in its integral form

$$\frac{dW}{dt} = - \int_{S_V} d\mathbf{a} \cdot \mathbf{S} - \frac{d}{dt} \int_V d\mathbf{r} w_{em} \tag{1.30}$$

or in its differential form by eliminating the integrals

$$\mathbf{E} \cdot \mathbf{j} = -\nabla \cdot \mathbf{S} - \frac{\partial w_{em}}{\partial t}. \quad (1.31)$$

The Poynting vector has units of $\frac{J}{m^2 s}$ and describes the flux of energy through a surface. From this, we can conclude that the physical meaning behind equations (1.30) and (1.31) is that the rate of change in time of the energy inside a volume added with the flow of energy in and out of that volume is equal to minus the work done by the fields on the sources inside the volume.

1.1.5 Momentum of a System of Fields and Field Sources

By taking the vector product of \mathbf{D} with equation (1.1c) and of \mathbf{B} with equation (1.1d) and then adding them up the following equality can be obtained:

$$\mathbf{D} \times (\nabla \times \mathbf{E}) + \mathbf{B} \times (\nabla \times \mathbf{H}) = -\mathbf{j} \times \mathbf{B} - \frac{\partial}{\partial t}(\mathbf{D} \times \mathbf{B}). \quad (1.32)$$

We will restrict this discussion to the case where there is no polarizable or magnetic media:

$$\varepsilon_0 \mathbf{E} \times (\nabla \times \mathbf{E}) + \frac{1}{\mu_0} \mathbf{B} \times (\nabla \times \mathbf{B}) = -\mathbf{j} \times \mathbf{B} - \varepsilon_0 \frac{\partial}{\partial t}(\mathbf{E} \times \mathbf{B}). \quad (1.33)$$

Considering that the speed of light in vacuum is $c = \frac{1}{\sqrt{\varepsilon_0 \mu_0}}$, equation (1.34) becomes

$$\varepsilon_0(\mathbf{E} \times (\nabla \times \mathbf{E}) + c^2 \mathbf{B} \times (\nabla \times \mathbf{B})) = -\mathbf{j} \times \mathbf{B} - \varepsilon_0 \frac{\partial}{\partial t}(\mathbf{E} \times \mathbf{B}). \quad (1.34)$$

In order to proceed, some vector algebra must be discussed. In particular, we would like to evaluate the following expression:

$$\mathbf{v}(\nabla \cdot \mathbf{v}) - \mathbf{v} \times (\nabla \times \mathbf{v})$$

We have

$$\begin{aligned} \mathbf{v} \times (\nabla \times \mathbf{v}) &= \mathbf{e}^i \varepsilon_{ijk} v^j (\nabla \times \mathbf{v})_k = \mathbf{e}^i \varepsilon_{ijk} v^j \varepsilon^{lmk} \partial_l v_m = \\ &= \mathbf{e}^i (\delta_i^l \delta_j^m - \delta_i^m \delta_j^l) v^j \partial_l v_m = \mathbf{e}^i [v^j \partial_i v_j - v^j \partial_j v_i] \end{aligned}$$

and

$$\mathbf{v}(\nabla \cdot \mathbf{v}) = \mathbf{e}^i v_i \partial_j v^j,$$

where ε_{ijk} is the Levi-Civita tensor, δ_i^j is the Kronecker-delta symbol and \mathbf{e}^i , $i = \overline{1,3}$ are the Cartesian versors. Subtracting these two expressions leads to

$$\mathbf{v}(\nabla \cdot \mathbf{v}) - \mathbf{v} \times (\nabla \times \mathbf{v}) = \mathbf{e}^i [v_i \partial_j v^j - v^j \partial_i v_j + v^j \partial_j v_i] = \mathbf{e}^i [\partial_j(v_i v^j) - v^j \partial_i v_j].$$

Since

$$\partial_i(v^j v_j) = 2v^j \partial_i v_j,$$

we have

$$\mathbf{v}(\nabla \cdot \mathbf{v}) - \mathbf{v} \times (\nabla \times \mathbf{v}) = \mathbf{e}^i \left[\partial_j(v_i v^j) - \frac{1}{2} \partial_i(v_j v^j) \right],$$

The second term can be stylized by introducing a Kronecker-delta and writing $v_j v^j$ as \mathbf{v}^2 , which leads to the desired final result

$$\mathbf{v}(\nabla \cdot \mathbf{v}) - \mathbf{v} \times (\nabla \times \mathbf{v}) = \mathbf{e}^i \partial_j \left[v_i v^j - \frac{1}{2} \mathbf{v}^2 \delta_i^j \right] = \mathbf{e}_i \partial_j \left[v^i v^j - \frac{1}{2} \mathbf{v}^2 \delta^{ij} \right]. \quad (1.35)$$

The last step is possible due to the fact that we only work with space-like components and is easy to perform because we chose the convenient metric (1.13).

By defining the Maxwell stress tensor as

$$T^{ij} = \epsilon_0 \left[E^i E^j + c^2 B^i B^j - \frac{1}{2} (\mathbf{E}^2 + c^2 \mathbf{B}^2) \delta^{ij} \right] \quad (1.36)$$

and using it along with equation (1.35) in equation (1.34) one gets

$$\mathbf{e}_i \partial_j T^{ij} = \epsilon_0 \mathbf{E}(\nabla \cdot \mathbf{E}) + \frac{1}{\mu_0} \mathbf{B}(\nabla \cdot \mathbf{B}) + \mathbf{j} \times \mathbf{B} + \epsilon_0 \frac{\partial}{\partial t} (\mathbf{E} \times \mathbf{B})$$

Using Maxwell's equations (1.2a) and (1.2b) together with the definition of the Poynting vector (1.22) the above expression is simplified to the law of momentum conservation

$$\mathbf{e}_i \partial_j T^{ij} = \rho \mathbf{E} + \mathbf{j} \times \mathbf{B} + \frac{1}{c^2} \frac{\partial \mathbf{S}}{\partial t} \quad (1.37)$$

or

$$\mathbf{e}_i \partial_j T^{ij} = \rho \mathbf{E} + \mathbf{j} \times \mathbf{B} + \frac{\partial \mathbf{g}}{\partial t}, \quad (1.38)$$

where the volumic density of the fields' electromagnetic momentum \mathbf{g} is defined to be

$$\mathbf{g} = \frac{1}{c^2} \mathbf{S} = \mathbf{D} \times \mathbf{B}. \quad (1.39)$$

By observing that when integrating over a volume, the $\rho \mathbf{E} + \mathbf{j} \times \mathbf{B}$ is simply the Lorentz force and that $\mathbf{e}_i \partial_j T^{ij} = \nabla \cdot \hat{T}$ we reach an integral form of the momentum conservation

$$\frac{d}{dt} (\mathbf{P}_{\text{em}} + \mathbf{P}_{\text{mech}}) = \int_V d\mathbf{r} \nabla \cdot \hat{T} = \int_{S_V} d\mathbf{a} \cdot \hat{T}, \quad (1.40)$$

where \mathbf{P}_{em} and \mathbf{P}_{mech} are the electromagnetic and mechanical momenta, respectively. If we integrate over the entire space and use the fact that the stress tensor vanishes at infinity, we obtain

$$\frac{d}{dt} (\mathbf{P}_{\text{em}} + \mathbf{P}_{\text{mech}}) = 0. \quad (1.41)$$

1.2 Electromagnetic Waves

The short review of classical electrodynamics had as an ultimate goal to introduce the definitions, equations and formalism required in order to study electromagnetic waves. In this section I will start from the definition and properties of an electromagnetic wave and I will follow up with how one can describe laser pulses. The second part will contain a short introduction to the laser profiles used in practical applications.

1.2.1 Maxwell's Equations in Vacuum

The concept of electromagnetic waves arises naturally from the Maxwell equations equation (1.1) if we consider them in the absence of any sources

$$\nabla \cdot \mathbf{D} = 0 \quad (1.42a)$$

$$\nabla \cdot \mathbf{B} = 0 \quad (1.42b)$$

$$\nabla \times \mathbf{E} = -\frac{\partial \mathbf{B}}{\partial t} \quad (1.42c)$$

$$\nabla \times \mathbf{H} = \frac{\partial \mathbf{D}}{\partial t}. \quad (1.42d)$$

The last equation (1.42d) can be rewritten using $\mathbf{H} = \frac{1}{\mu} \mathbf{B}$ and $\mathbf{D} = \epsilon \mathbf{E}$ as

$$\nabla \times \mathbf{B} = \epsilon \mu \frac{\partial \mathbf{E}}{\partial t} \quad (1.43)$$

By taking the curl of equation (1.42c) one gets

$$\nabla \times (\nabla \times \mathbf{E}) + \frac{\partial}{\partial t} (\nabla \times \mathbf{B}) = 0,$$

which, using the vector identity

$$\nabla \times (\nabla \times \mathbf{v}) = \nabla(\nabla \cdot \mathbf{v}) - \nabla^2 \mathbf{v} \quad (1.44)$$

and equation (1.42a), becomes

$$\left[\nabla^2 - \epsilon \mu \frac{\partial^2}{\partial t^2} \right] \mathbf{E} = 0. \quad (1.45)$$

Through an analogous procedure, one obtains that the magnetic field \mathbf{B} satisfies the same equation. Using the D'Alembertian defined in section 1.1.3 we can conclude that both the electric and magnetic fields satisfy the Helmholtz equation

$$\square \mathbf{E} = 0 \quad (1.46a)$$

$$\square \mathbf{B} = 0, \quad (1.46b)$$

with $v^2 = \frac{1}{\epsilon \mu}$ giving the speed of the wave (also called phase velocity) and $c^2 = \frac{1}{\epsilon_0 \mu_0}$ the speed of electromagnetic waves in vacuum.

The reader most probably has encountered waves in various contexts before, but I will add a reminder of the relevant parameters describing solutions of the Helmholtz equation just for the sake of completeness:

- if \mathbf{n} is the unit vector along the direction of propagation, the wave vector is defined as $\mathbf{k} = \mathbf{n}k$, where $k = \frac{2\pi}{\lambda}$ is the wave number and λ is the wavelength;
- if T is the period in time of the wave, the frequency is defined as $\nu = \frac{1}{T}$ and, equivalently, the angular frequency is defined as $\omega = 2\pi\nu$;
- $v = \lambda\nu = \frac{\omega}{k} = \frac{1}{\sqrt{\epsilon\mu}}$ is the phase velocity and $v_g = \frac{\partial\omega}{\partial k}$ is the group velocity.

There is one more property we can derive before discussing the particular solutions of equation (1.46), namely the transverse character of electromagnetic waves in vacuum.

A very general form for a solution of equation (1.46) can be written as

$$\mathbf{E} = \mathbf{E}_0 f(\mathbf{k} \cdot \mathbf{r} - \omega t),$$

where \mathbf{E}_0 is a constant vector. Using it in equation (1.42c) leads to the following development

$$0 = \nabla \cdot \mathbf{E} = \nabla \cdot [\mathbf{E}_0 f(\mathbf{k} \cdot \mathbf{r} - \omega t)] = \mathbf{E}_0 \nabla f(\mathbf{k} \cdot \mathbf{r} - \omega t) = \mathbf{k} \cdot \mathbf{E}_0 f'(\mathbf{k} \cdot \mathbf{r} - \omega t)$$

which concludes that

$$\mathbf{k} \cdot \mathbf{E} = 0. \quad (1.47)$$

Similarly, equation (1.42c) leads to

$$-\frac{\partial \mathbf{B}}{\partial t} = \nabla \times \mathbf{E} = \nabla \times [\mathbf{E}_0 f(\mathbf{k} \cdot \mathbf{r} - \omega t)] = \mathbf{k} \times \mathbf{E}_0 f'(\mathbf{k} \cdot \mathbf{r} - \omega t),$$

where in the last step this identity was used

$$\nabla \times (a\mathbf{v}) = a(\nabla \times \mathbf{v}) + (\nabla a) \times \mathbf{v}. \quad (1.48)$$

This suggests that

$$\mathbf{B} \propto \mathbf{k} \times \mathbf{E}. \quad (1.49)$$

Looking at equations (1.47) and (1.49) it is easy to conclude that the electromagnetic waves are transverse and that at any moment, the magnetic and electric fields are perpendicular to one another.

Note: Electromagnetic waves can only be transversal in “free space” or homogeneous media (Heaviside 1971). Longitudinal modes can also be achieved in special conditions, like inside confined spaces and in plasmas (Jackson 1999; Griffiths 1999). However, there has been work done on the production of longitudinal waves in vacuum (H. Wang *et al.* 2008) as a consequence of theoretical work showing the possibility of having a small longitudinal component in electromagnetic waves in vacuum (Cicchitelli, Hora, and Postle 1990) using an improved paraxial approximation.

1.2.2 Plane Waves

The simplest solution to the Helmholtz equation (1.46) is the plane wave

$$\sin(\mathbf{k} \cdot \mathbf{r} - \omega t + \delta) \quad (1.50)$$

In the research literature it is common to employ a complex formulation (Vrejoiu 1987). Thus, the complex fields are defined as

$$\tilde{\mathbf{E}}(\mathbf{r}, t) = E_0 \mathbf{s} e^{i(\mathbf{k} \cdot \mathbf{r} - \omega t)} \quad (1.51a)$$

$$\tilde{\mathbf{B}}(\mathbf{r}, t) = B_0 \mathbf{n} \times \mathbf{s} e^{i(\mathbf{k} \cdot \mathbf{r} - \omega t)}, \quad (1.51b)$$

where E_0 and B_0 are the real amplitudes and \mathbf{s} is a complex vector of norm one

$$\mathbf{s} = \mathbf{s}_r + i\mathbf{s}_i, \quad |\mathbf{s}|^2 = \mathbf{s}^* \cdot \mathbf{s} = \mathbf{s}_r^2 + \mathbf{s}_i^2 = 1$$

With this setup, the real fields are to be obtained as

$$\mathbf{E}(\mathbf{r}, t) = \operatorname{Re}\left\{\tilde{\mathbf{E}}(\mathbf{r}, t)\right\} = E_0 [\mathbf{s}_r \cos(\mathbf{k} \cdot \mathbf{r} - \omega t) - \mathbf{s}_i \sin(\mathbf{k} \cdot \mathbf{r} - \omega t)] \quad (1.52a)$$

$$\mathbf{B}(\mathbf{r}, t) = \operatorname{Re}\left\{\tilde{\mathbf{B}}(\mathbf{r}, t)\right\} = B_0 \mathbf{n} \times [\mathbf{s}_r \cos(\mathbf{k} \cdot \mathbf{r} - \omega t) - \mathbf{s}_i \sin(\mathbf{k} \cdot \mathbf{r} - \omega t)]. \quad (1.52b)$$

In what follows we are interested in analyzing the plane wave solution from the perspective of energy in the formalism developed in sections 1.1.4 and 1.1.5.

From the discussion in the previous subsection it is easy to deduce the relation between the magnetic and electric fields of a wave (it is the same for both the real and complex fields)

$$\tilde{\mathbf{B}} = \frac{1}{c} \mathbf{n} \times \tilde{\mathbf{E}}. \quad (1.53)$$

With this, the energy density (1.20) of the fields is

$$w_{em} = \frac{1}{2} \varepsilon_0 \mathbf{E}^2 + \frac{1}{2\mu_0} \mathbf{B}^2 = \varepsilon_0 \mathbf{E}^2, \quad (1.54)$$

which can be computed using equation (1.52a) to be

$$w_{em} = \varepsilon_0 E_0^2 [\mathbf{s}_r^2 \cos^2(\mathbf{k} \cdot \mathbf{r} - \omega t) + \mathbf{s}_i^2 \sin^2(\mathbf{k} \cdot \mathbf{r} - \omega t) - \mathbf{s}_r \cdot \mathbf{s}_i \sin(2\mathbf{k} \cdot \mathbf{r} - 2\omega t)]. \quad (1.55)$$

This quantity could vary quite wildly in time depending on the wave's frequency, so we would rather compute a quantity that can be measured experimentally, which is of course the time average of the energy density

$$\langle w_{em} \rangle = \frac{1}{T} \int_0^T dt w_{em} = \frac{\varepsilon_0 E_0^2}{T} \int_0^T dt [\mathbf{s}_r^2 \cos^2(\mathbf{k} \cdot \mathbf{r} - \omega t) + \mathbf{s}_i^2 \sin^2(\mathbf{k} \cdot \mathbf{r} - \omega t) - \mathbf{s}_r \cdot \mathbf{s}_i \sin(2\mathbf{k} \cdot \mathbf{r} - 2\omega t)] \quad (1.56)$$

Since we know that the average of sine over one period is zero and the averages of both sine and cosine squared over one period are one half, we get

$$\langle w_{em} \rangle = \frac{\varepsilon_0 E_0^2}{2}. \quad (1.57)$$

But looking at definition (1.51a) we see that

$$\langle w_{em} \rangle = \frac{\varepsilon_0}{2} \tilde{\mathbf{E}}^* \cdot \tilde{\mathbf{E}}. \quad (1.58)$$

In a very similar way we have for the Poynting vector the following development

$$\mathbf{S} = \frac{1}{\mu_0} \mathbf{E} \cdot \mathbf{B} = \frac{1}{\mu_0 c} \mathbf{n} \mathbf{E}^2 \quad (1.59)$$

$$\langle \mathbf{S} \rangle = \sqrt{\frac{\varepsilon_0}{\mu_0}} \langle \mathbf{E}^2 \rangle \mathbf{n} = \frac{1}{2} \sqrt{\frac{\varepsilon_0}{\mu_0}} E_0^2 \mathbf{n} = c \langle w_{em} \rangle \mathbf{n} \quad (1.60)$$

$$\langle \mathbf{S} \rangle = \frac{1}{2\mu_0} \tilde{\mathbf{E}} \times \tilde{\mathbf{B}}^*. \quad (1.61)$$

And, obviously, the electromagnetic momentum (1.39) is

$$\langle \mathbf{g} \rangle = \left\langle \frac{1}{c^2} \mathbf{S} \right\rangle = \frac{\langle w_{em} \rangle}{c^2} \mathbf{n}. \quad (1.62)$$

Polarization of Plane Waves

For any arbitrary complex field we can find a decomposition of the real field in orthogonal components. In order to do that, we make the following notations concerning the complex vector of (1.51a)

$$\mathbf{s} \cdot \mathbf{s} = \alpha^2 e^{2i\theta} \text{ with } \alpha, \theta \in \mathbb{R}. \quad (1.63)$$

We can define $\mathbf{u} = \mathbf{s} e^{-i\theta}$ such that $\mathbf{u}_r \cdot \mathbf{u}_i = 0$. In this way the orthogonal coordinates system can be chosen as

$$\mathbf{e}_x = \frac{\mathbf{u}_r}{|\mathbf{u}_r|}, \mathbf{e}_y = \pm \frac{\mathbf{u}_i}{|\mathbf{u}_i|}, \mathbf{e}_z = \mathbf{n}, \quad (1.64)$$

with the sign of \mathbf{e}_y being conveniently chosen in order to have a right-handed system (*i.e.* $\mathbf{e}_x \times \mathbf{e}_y = \mathbf{e}_z$).

The real field (1.52a) is in this basis

$$\mathbf{E} = E_0 [u_r \mathbf{e}_x \cos(\mathbf{k} \cdot \mathbf{r} - \omega t + \theta) \mp u_i \mathbf{e}_y \sin(\mathbf{k} \cdot \mathbf{r} - \omega t + \theta)]. \quad (1.65)$$

For time-independent \mathbf{e}_x , \mathbf{e}_y and \mathbf{e}_z , the following cases are to be distinguished:

- u_r, u_i arbitrary and non-zero: elliptically polarized wave;
- $u_r = u_i \neq 0$: circularly polarized wave;
- either $u_r = 0$ or $u_i = 0$: linearly polarized wave.

1.2.3 Paraxial Approximation

This and the next section discuss the ways in which we can describe beams of electromagnetic waves (like, say, laser beams) and follows ideas from Goldsmith 1998.

The paraxial approximation aims to simplify the Helmholtz equation

$$\left[\nabla^2 - \frac{1}{c^2} \frac{\partial^2}{\partial t^2} \right] \psi = 0. \quad (1.66)$$

We can treat this equation by the method of separation of variables $\psi = \zeta(\mathbf{r})T(t)$ in order for it to become

$$\frac{1}{\zeta} \nabla^2 \zeta = \frac{1}{c^2} \frac{T''}{T} = -k^2, \quad (1.67)$$

where k is simply the wave number. It is clear that the solution of the time equation is a combination of sine and cosine functions, so the real problem consists in solving the spatial equation

$$\nabla^2 \zeta + k^2 \zeta = 0. \quad (1.68)$$

In the particular case of electromagnetic waves, this equation must hold for the complex vector $\tilde{\mathbf{E}}$, so it must hold for each of its components. The Helmholtz equation for the electric field can be reduced by considering a solution of the form

$$\zeta(\mathbf{r}) = u(\mathbf{r}) e^{-ikz}, \quad (1.69)$$

where the z-axis was chosen as the propagation direction for the wave.

Inserting (1.69) in equation (1.68) we get

$$\begin{aligned} 0 &= \nabla^2 \zeta + k^2 \zeta = (\partial_x^2 u + \partial_y^2 u) e^{-ikz} + \partial_z^2 (u e^{-ikz}) + k^2 u e^{-ikz} = \\ &= (\partial_x^2 u + \partial_y^2 u) e^{-ikz} + (\partial_z^2 u) e^{-ikz} - 2ik(\partial_z u) e^{-ikz} - k^2 u e^{-ikz} + k^2 u e^{-ikz} = \\ &= e^{-ikz} \nabla^2 u - 2ik e^{-ikz} \partial_z u. \end{aligned}$$

Multiplying with e^{ikz} leads to

$$\nabla^2 u - 2ik \partial_z u = 0. \quad (1.70)$$

The first paraxial approximation argument says that, due to diffraction, the variation of the amplitude u along the direction of propagation is very small compared to distances of the order of the wave's wavelength. This can be summarized by the mathematical condition

$$\lambda \frac{\Delta(\partial_z u)}{\Delta z} \ll \partial_z u, \quad (1.71)$$

which indicates that the double partial derivative with respect to z (the propagation axis) is negligible compared to the $2ik\partial_z u$ term. The second argument says that in the Laplacian, the double partial derivative with respect to the z coordinate can be neglected, such that one obtains

$$\partial_x^2 u + \partial_y^2 u - 2ik \partial_z u = 0. \quad (1.72)$$

which is the paraxial wave equation.

1.2.4 Gaussian Beams

One can find solutions to equation (1.72) working in various coordinate systems, but the most convenient and useful for our purpose (and in practical applications in general) is to work in cylindrical coordinates. In this case, the equation becomes

$$\partial_r^2 u + \frac{1}{r} \partial_r u + \frac{1}{r} \partial_\varphi^2 u - 2ik \partial_z u = 0. \quad (1.73)$$

To simplify our calculations even more, we can remove the φ dependence of u , which means to imply axial symmetry for the wave. This gives

$$\partial_r^2 u + \frac{1}{r} \partial_r u - 2ik \partial_z u = 0. \quad (1.74)$$

The radial part of the equation suggests that we should have a dependence proportional to a complex exponential of r^2 . An educated guess would be a Gaussian distribution-like function of the form

$$u(r, z) = G(z) e^{-i \frac{kr^2}{2q(z)}}, \quad (1.75)$$

where the complex functions $G(z)$ and $q(z)$ are to be determined. Let us do just that by inserting (1.75) in equation (1.74):

$$\partial_r u = -\frac{ikr}{q(z)} G(z) e^{-i \frac{kr^2}{2q(z)}}.$$

$$\begin{aligned}\partial_r^2 u &= -\frac{ik}{q(z)} G(z) \left[1 - \frac{ikr^2}{q(z)} \right] e^{-i\frac{kr^2}{2q(z)}} \\ \partial_z u &= \left[G'(z) + \frac{ikr^2}{2q^2(z)} G(z) q'(z) \right] e^{-i\frac{kr^2}{2q(z)}}.\end{aligned}$$

Replacing these results and ridding ourselves of the exponential leads to

$$-2ik \left(\frac{G}{q} + G' \right) + \frac{k^2 r^2 G}{q^2} (q' - 1) = 0, \quad (1.76)$$

which gives the following differential equations for G and q :

$$\frac{dq}{dz} = 1 \quad (1.77a)$$

$$\frac{dG}{dz} = -\frac{G}{q}. \quad (1.77b)$$

The solution of equation (1.77a) is trivial

$$q(z) = q(z_0) + z - z_0,$$

and can be simplified by choosing our origin at z_0

$$q(z) = q(0) + z. \quad (1.78)$$

The quantity q (which is actually complex) is often called *Gaussian beam parameter*. Since it appears in (1.75) as $\frac{1}{q}$, it is convenient to express it in the form

$$\frac{1}{q} = \left(\frac{1}{q} \right)_r - i \left(\frac{1}{q} \right)_i. \quad (1.79)$$

If we now substitute this in the guessed solution (1.75) we obtain

$$u(r, z) = G(z) e^{-\frac{ikr^2}{2} \left[\left(\frac{1}{q} \right)_r - i \left(\frac{1}{q} \right)_i \right]} = G(z) e^{-\frac{kr^2}{2} \left(\frac{1}{q} \right)_i} e^{-\frac{ikr^2}{2} \left(\frac{1}{q} \right)_r}. \quad (1.80)$$

The real part of $\frac{1}{q}$ has physical significance. In order to see this, imagine that at a point z on the propagation direction we draw a plane perpendicular to the z -axis. If R would be the radius of curvature of the wavefront at point z (with respect to the position of the source), we can define $\phi(r) = k\delta x$ to be the difference in phase between the wavefront and the plane as a function of r . Since we work in the paraxial approximation, we can consider that $r \ll R$, such that, using as reference figure 1.1, we have

$$\alpha \approx \frac{r}{R} \quad (1.81a)$$

$$\delta x = -R(1 - \cos(\alpha)) \approx R \frac{\alpha^2}{2} \quad (1.81b)$$

$$\phi(r) \approx -\frac{kr^2}{2} \frac{1}{R}. \quad (1.81c)$$

We can conclude now that

$$\left(\frac{1}{q} \right)_r = \frac{1}{R}. \quad (1.82)$$

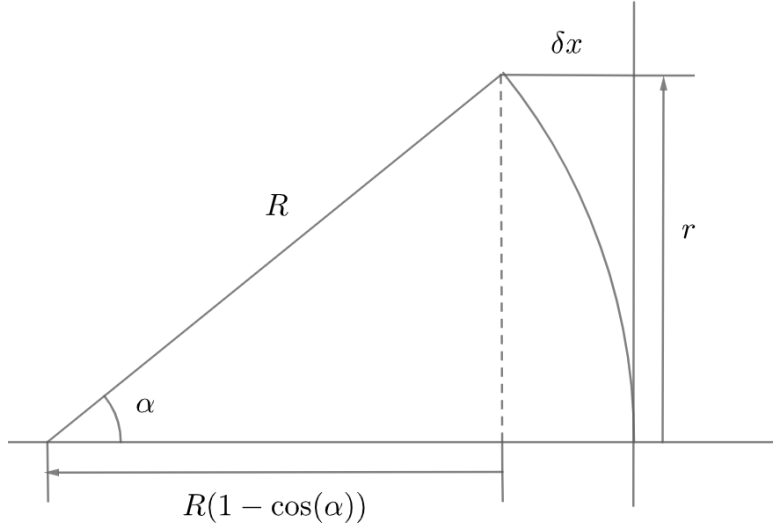


Figure 1.1: A drawing showing how to compute $\phi(r)$

The imaginary part of $\frac{1}{q}$ appears in the real exponential. This exponential should thus give the Gaussian distribution form of the wave, which means that it should look like

$$e^{-\left(\frac{r}{r_0}\right)^2}, \quad (1.83)$$

where r_0 is proportional to the standard deviation. In this case we can write

$$\left(\frac{1}{q}\right)_i = \frac{2}{kw^2(z)} = \frac{\lambda}{\pi w^2(z)}. \quad (1.84)$$

This defines the *beam radius* $w(z)$ as the value of r at which the field falls to $\frac{1}{e}$ of its value on the z-axis. Putting these results together, we reach a final formula for $\frac{1}{q}$

$$\frac{1}{q} = \frac{1}{R(z)} - i \frac{\lambda}{\pi w^2(z)}. \quad (1.85)$$

It is conventional to take $\lim_{z \rightarrow 0} R(z) \rightarrow \infty$, such that $\frac{1}{q(0)} = -i \frac{\lambda}{\pi w_0^2}$, and $w_0 = w(0)$ is usually interpreted as the *beam waist radius*. If we look back at the solution (1.78), we can rewrite q in this formalism as

$$q = z + i \frac{\pi w_0^2}{\lambda}. \quad (1.86)$$

Playing around with equations (1.85) and (1.86) we have the following development

$$\frac{1}{q} = \frac{1}{R} - i \frac{\lambda}{\pi w^2} = \frac{1}{z + i \frac{\pi w_0}{\lambda}} = \frac{z - i \frac{\pi w_0}{\lambda}}{z^2 + \left(\frac{\pi w_0^2}{\lambda}\right)^2}$$

$$\frac{1}{R} = \frac{z}{z^2 + \left(\frac{\pi w_0^2}{\lambda}\right)^2} \Rightarrow R = z + \frac{1}{z} \left(\frac{\pi w_0^2}{\lambda}\right)^2$$

$$\frac{1}{w^2} = \frac{\frac{\pi^2 w_0^2}{\lambda^2}}{z^2 + \left(\frac{\pi w_0^2}{\lambda}\right)^2} \Rightarrow w = w_0 \sqrt{1 + \left(\frac{\lambda z}{\pi w_0^2}\right)^2}.$$

For the sake of clarity, I write again the expressions obtained for the radius of curvature and the beam radius

$$R = z + \frac{1}{z} \left(\frac{\pi w_0^2}{\lambda} \right)^2 \quad (1.87)$$

$$w = w_0 \sqrt{1 + \left(\frac{\lambda z}{\pi w_0^2} \right)^2}. \quad (1.88)$$

Turning back now to equation (1.77b), using (1.86), we can rewrite it as

$$\frac{dG}{G} = - \frac{d\left(z + i\frac{\pi w_0^2}{\lambda}\right)}{z + i\frac{\pi w_0^2}{\lambda}},$$

which, after integration, becomes

$$\ln \frac{G(z)}{G(0)} = \ln \frac{z + i\frac{\pi w_0^2}{\lambda}}{i\frac{\pi w_0^2}{\lambda}}$$

or

$$\frac{G(z)}{G(0)} = \frac{1}{1 - i\frac{\lambda z}{\pi w_0^2}} = \frac{1 + i\frac{\lambda z}{\pi w_0^2}}{1 + \left(\frac{\lambda z}{\pi w_0^2}\right)^2}. \quad (1.89)$$

For convenience, this is usually expressed in terms of a phasor (commonly called Gouy phase) defined as

$$\tan(\phi_0) = \frac{\lambda z}{\pi w_0^2}. \quad (1.90)$$

Now the solution for G is stylized to be

$$\frac{G(z)}{G(0)} = \frac{w_0}{w} e^{i\phi_0}. \quad (1.91)$$

Putting together equations (1.75), (1.85) and (1.91) we finally find u

$$u(r, z) = G(0) \frac{w_0}{w} \exp\left(-\frac{r^2}{w^2} - i\frac{\pi r^2}{\lambda R} + i\phi_0\right) \quad (1.92)$$

and, consequently, the solution to the paraxial wave equation with axial symmetry

$$\zeta(r, z) = G(0) \frac{w_0}{w} \exp\left(-\frac{r^2}{w^2} - ikz - i\frac{\pi r^2}{\lambda R} + i\phi_0\right). \quad (1.93)$$

1.2.5 Gaussian Beam Packets

In the research literature, it is a custom to use a parameter called *confocal distance* or *Reyleigh range*

$$z_0 = \frac{\pi w_0^2}{\lambda}. \quad (1.94)$$

Including it, all the relevant auxiliary functions become

$$R(z) = z + \frac{z_0^2}{z} \quad (1.95a)$$

$$w(z) = w_0 \sqrt{1 + \left(\frac{z}{z_0}\right)^2} \quad (1.95b)$$

$$\phi_0(z) = \arctan\left(\frac{z}{z_0}\right). \quad (1.95c)$$

We can immediately observe that $w(z)$ at $z = z_0$ is actually equal to $\sqrt{2}w_0$. From this we can deduce that the z_0 indicates how far from the origin the beam is collimated. It is very simple to understand by looking at figure 1.2

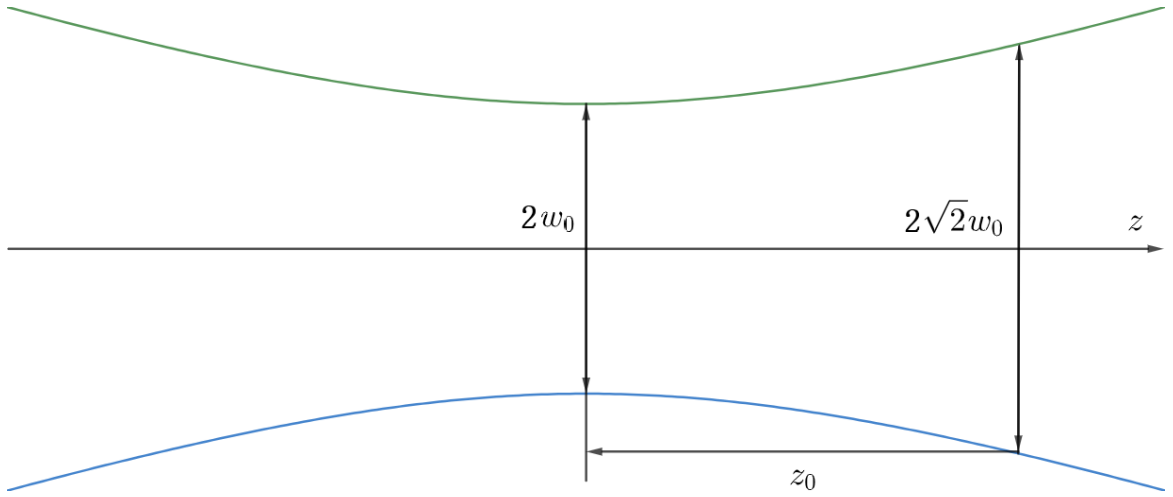


Figure 1.2: Gaussian beam radius w as a function of z

We can also differentiate three cases of interest for the curvature radius $R(z)$. At $z \rightarrow 0$, i.e. near the waist, $R \rightarrow \infty$, so the profile is that of a plane wave. At the Rayleigh range, the curvature ($\frac{1}{R}$) is maximum and, consequently, the radius itself is minimum ($2z_0$). Finally, at very large distances away from the waist, the radius is equal to z , so the profile is spherical.

The Gouy phase is an important parameter in theoretical considerations, especially when it comes to higher order Gaussian modes, but is hard to observe experimentally. Physically, it modifies the wavelength near the waist (Paschotta 2020). This results also in a change of the phase velocity. As a consequence, the phase velocity near the waist can exceed the velocity of light in the medium, just as it might inside a waveguide.

Now that we understood the shape and behaviour of the Gauss beam, we are almost ready to define the electric and magnetic fields. But before that we must talk about normalization. While a look at (1.93) might not suggest the need for any normalization, physical arguments request it. We would like to not have unexplained losses of power as a function of z (remember that we are basically just setting the dependence of the fields on position right now). As such, a normalization of $\zeta(r, z)$ over the transversal surface is necessary. That is, we want the intensity as a function of z to be just a constant. While in literature is very common to impose norm 1, I find it more useful to norm it to πw_0^2 , as suggested by Dondero 2020, such that the final result is adimensional and it is easier to introduce the amplitude of the field. We have

$$\frac{1}{2}\pi w_0^2 = \iint dr d\varphi r |\zeta|^2 = 2\pi |G(0)|^2 \int dr \left|\frac{w_0}{w}\right|^2 r e^{-2\frac{r^2}{w^2}} =$$

$$\begin{aligned}
&= \frac{1}{2}\pi \left(\frac{w_0}{w}\right)^2 |G(0)|^2 w^2 \int d \left(2\frac{r^2}{w^2}\right) e^{-2\frac{r^2}{w^2}} = \\
&= \frac{1}{2}\pi w_0^2 G^2(0)
\end{aligned}$$

which gives the normalization constant

$$G(0) = 1. \quad (1.96)$$

The Electric Field

The x and y components of the electric field are now expressed using equation (1.93) as

$$E_x(r, z) = \alpha_x E_0 \frac{w_0}{w} \exp\left(-\frac{r^2}{w^2} - ikz - i\frac{kr^2}{2R} + i\phi_0\right) \quad (1.97a)$$

$$E_y(r, z) = \alpha_y E_0 \frac{w_0}{w} \exp\left(-\frac{r^2}{w^2} - ikz - i\frac{kr^2}{2R} + i\phi_0\right), \quad (1.97b)$$

where we choose $\alpha_x = 1$, $\alpha_y = 0$ for linear polarization, and $\alpha_x = \frac{1}{\sqrt{2}}$, $\alpha_y = \pm\frac{i}{\sqrt{2}}$ for right and left-handed circular polarization, respectively. We see that E_0 is simply the value of the field at $z = 0$ and $t = 0$. In order to obtain the z component, we have to impose the condition $\nabla \cdot \mathbf{E} = 0$ and to use the approximation $\partial_z E_z \approx -ikE_z$ (which holds if the pulse is long enough or quasi-rectangular). The immediate result is

$$E_z(r, z) = -\frac{i}{k} (\partial_x E_x(r, z) + \partial_y E_y(r, z)), \quad (1.98)$$

or, explicitly

$$E_z(r, z) = \frac{2\left(i - \frac{z}{z_0}\right)}{kw^2(z)} [xE_x(r, z) + yE_y(r, z)]. \quad (1.99)$$

The Magnetic Field

In order to derive the magnetic field, one can impose the relation (1.53)

$$\mathbf{B} = \frac{1}{c} \mathbf{n} \times \mathbf{E} = \frac{1}{c} \mathbf{e}_z \times \mathbf{E} = \frac{1}{c} E_x \mathbf{e}_z \times \mathbf{e}_x + \frac{1}{c} E_y \mathbf{e}_z \times \mathbf{e}_y = -\frac{1}{c} E_y \mathbf{e}_x + \frac{1}{c} E_x \mathbf{e}_y,$$

which indicates that

$$B_x(r, z) = -\frac{1}{c} E_y(r, z) \quad (1.100a)$$

$$B_y(r, z) = \frac{1}{c} E_x(r, z). \quad (1.100b)$$

The third component is found exactly in the same way as for the electric field, taking into account that $\nabla \cdot \mathbf{B} = 0$ and using the same approximation $\partial_z B_z \approx -ikB_z$ (the conditions for its validity are the same):

$$B_z(r, z) = -\frac{i}{k} (\partial_x B_x(r, z) + \partial_y B_y(r, z)) = -\frac{i}{ck} (\partial_y E_x(r, z) - \partial_x E_y(r, z)) , \quad (1.101)$$

or rather

$$B_z(r, z) = \frac{2 \left(i - \frac{z}{z_0} \right)}{ckw^2(z)} [yE_x(r, z) - xE_y(r, z)] . \quad (1.102)$$

The Temporal Profile

One observation must be made now. These expressions only describe the spatial part of the field. In order to give the exact field we must add the time-dependent part of the solution $e^{i\omega t}$. However, this is not all there is to it. Since we are interested in describing laser beams, we must take into consideration the fact that the pulse has a finite duration. One does this by adding a Gaussian envelope over time. The time-dependent part will now be

$$g(z, t) = \exp \left(i\omega t - \left(\frac{t - \frac{z-z_F}{c}}{\tau_0} \right)^2 \right) , \quad (1.103)$$

where τ_0 is the duration of the pulse and z_F is the original position of the intensity peak.

In what follows, I aim to provide a short proof of the fact that even with this envelope, the final fields are still solutions of Helmholtz equation under the paraxial approximation.

Let $f(r, z)$ be the solution for

$$\partial_r^2 f + \frac{1}{r} \partial_r f - 2ik \partial_z f = 0 . \quad (1.104)$$

The solution for the complete Helmholtz equation

$$\partial_r^2 u + \frac{1}{r} \partial_r u + \partial_z^2 u - \frac{1}{c^2} \partial_t^2 u = 0 \quad (1.105)$$

is proposed to be $u(r, z) = f(r, z)g(z, t)e^{-ikz}$ such that we have

$$\partial_r^2(fg e^{-ikz}) + \frac{1}{r} \partial_r(fg e^{-ikz}) + \partial_z^2(fg e^{-ikz}) - \frac{1}{c^2} \partial_t^2(fg e^{-ikz}) = 0$$

$$(\partial_r^2 f + \frac{1}{r} \partial_r f)g e^{-ikz} + (\partial_z^2 f)g e^{-ikz} + 2(\partial_z f)\partial_z(g e^{-ikz}) + f\partial_z^2(g e^{-ikz}) - \frac{1}{c^2} f\partial_t^2(g e^{-ikz}) = 0 .$$

The paraxial approximation allows us to ignore the $\partial_z^2 f$ term

$$(\partial_r^2 f + \frac{1}{r} \partial_r f)g e^{-ikz} + 2(\partial_z f)\partial_z(g e^{-ikz}) + f\partial_z^2(g e^{-ikz}) - \frac{1}{c^2} f\partial_t^2(g e^{-ikz}) = 0$$

$$(\partial_r^2 f + \frac{1}{r} \partial_r f - 2ik \partial_z f)g e^{-ikz} + 2(\partial_z f)e^{-ikz} \partial_z g + f\partial_z^2(g e^{-ikz}) - \frac{1}{c^2} f\partial_t^2(g e^{-ikz}) = 0$$

$$(\partial_r^2 f + \frac{1}{r} \partial_r f - 2ik \partial_z f)g e^{-ikz} + f \left[2 \frac{\partial_z f}{f} e^{-ikz} \partial_z g + \partial_z^2(g e^{-ikz}) - \frac{1}{c^2} \partial_t^2(g e^{-ikz}) \right] = 0 .$$

The first term is zero since f is a solution, so we must have the second term also equal to zero

$$2\frac{\partial_z f}{f} e^{-ikz} \partial_z g + \partial_z^2(g e^{-ikz}) - \frac{1}{c^2} \partial_t^2(g e^{-ikz}) = 0$$

$$2\frac{\partial_z f}{f} e^{-ikz} \partial_z g + (\partial_z^2 g) e^{-ikz} - 2ik(\partial_z g) e^{-ikz} - k^2 g e^{-ikz} - \frac{1}{c^2} (\partial_t^2 g) e^{-ikz} = 0$$

and eliminating the exponential

$$2\frac{\partial_z f}{f} \partial_z g + \partial_z^2 g - 2ik\partial_z g - k^2 g - \frac{1}{c^2} \partial_t^2 g = 0$$

or, using $ck = \omega$

$$2i\omega c \partial_z g + \partial_t^2 g + \omega^2 g = c^2 \partial_z^2 g + 2c^2 \frac{\partial_z f}{f} \partial_z g. \quad (1.106)$$

Based on equation (1.103) we have

$$\partial_z g = \frac{2}{c} \frac{t - \frac{z-z_F}{c}}{\tau_0^2} g \Rightarrow 2i\omega c \partial_z g = 4i\omega \frac{t - \frac{z-z_F}{c}}{\tau_0^2} g \quad (1.107)$$

$$\partial_z^2 g = -\frac{2}{c^2} \frac{1}{\tau_0^2} g + \frac{4}{c^2} \left(\frac{t - \frac{z-z_F}{c}}{\tau_0^2} \right)^2 g \Rightarrow c^2 \partial_z^2 g = -2 \frac{1}{\tau_0^2} g + 4 \left(\frac{t - \frac{z-z_F}{c}}{\tau_0^2} \right)^2 g \quad (1.108)$$

$$\partial_t g = \left(i\omega - 2 \frac{t - \frac{z-z_F}{c}}{\tau_0^2} \right) g \quad (1.109)$$

$$\partial_t^2 g = -2 \frac{1}{\tau_0^2} g + \left(i\omega - 2 \frac{t - \frac{z-z_F}{c}}{\tau_0^2} \right)^2 g = -4i\omega \frac{t - \frac{z-z_F}{c}}{\tau_0^2} g - 2 \frac{1}{\tau_0^2} g - \omega^2 g + 4 \left(\frac{t - \frac{z-z_F}{c}}{\tau_0^2} \right)^2 g \quad (1.110)$$

Summing everything up, we still remain with a

$$\frac{\partial_z f}{f} \partial_z g = 0, \quad (1.111)$$

which is true under the paraxial approximation.

It is important to mention that this profile is not always usable. According to Quesnel and Mora 1998 finite pulse effects are important for $c\tau_0 \lesssim 2w_0$, and in this situation we must put an additional $2\partial_z g \partial_z \mathbf{E}$ in the paraxial wave equation.

The Final Fields

The final relations are straightforward

$$\mathbf{E}(r, z, t) = \mathbf{E}(r, z)g(t, z) \quad (1.112a)$$

$$\mathbf{B}(r, z, t) = \mathbf{B}(r, z)g(t, z). \quad (1.112b)$$

1.2.6 Laguerre-Gauss Beams

This type of beam represents a correction for the Gauss one in order to remove the axial symmetry approximation. That is, we want to find a function $f(r, z, \varphi) = \zeta(r, z)s(r, z, \varphi)$ which is intended to be a solution of

$$\partial_r^2 f + \frac{1}{r} \partial_r f + \frac{1}{r} \partial_\varphi^2 f - 2ik\partial_z f = 0, \quad (1.113)$$

where ζ is found in (1.93). Actually, we would rather make an educated guess for a trial solution

$$f(r, z, \varphi) = \zeta(r, z)S(r) e^{im\varphi}, \quad (1.114)$$

with m can be a real number. In this case, it is straightforward to find that $S(r)$ turns out to satisfy an equation similar to that of the associated Laguerre polynomials. One can reach through not so short computations the expression

$$S(r) = \left(\frac{\sqrt{2r}}{w(z)} \right)^m L_{pm} \left(\frac{2r^2}{w^2(z)} \right) \exp \left(i(2p+m) \arctan \left(\frac{z}{z_0} \right) \right). \quad (1.115)$$

The associated (or sometimes also called generalized) Laguerre polynomials are a solution of (Abramowitz and Stegun 2013)

$$xL''_{pm}(x) + (m+1-x)L'_{pm}(x) + pL_{pm}(x) = 0, \quad (1.116)$$

where $p \in \mathbb{N}$ and $m \in \mathbb{R}$. Their expression can be obtained using the Rodrigues formula

$$L_{pm}(x) = \frac{x^{-m} e^x}{p!} \frac{d^p}{dx^p} (e^{-x} x^{m+p}). \quad (1.117)$$

We will now apply the same normalization criterion we used for the Gauss mode for $f(r, z, \varphi)$

$$\frac{1}{2}\pi w_0^2 = \iint dr d\varphi r |f|^2. \quad (1.118)$$

The integration is done as such

$$\begin{aligned} \iint dr d\varphi r |f|^2 &= 2\pi \int dr r |\zeta|^2 |S|^2 = 2\pi |G(0)|^2 \left(\frac{w_0}{w} \right)^2 \int dr r e^{-\frac{2r^2}{w^2}} \left(\frac{2r^2}{w^2} \right)^m L_{pm}^2 \left(\frac{2r^2}{w^2} \right) = \\ &= \frac{1}{2}\pi |G(0)|^2 \left(\frac{w_0}{w} \right)^2 w^2 \int d \left(\frac{2r^2}{w^2} \right) e^{-\frac{2r^2}{w^2}} \left(\frac{2r^2}{w^2} \right)^m L_{pm}^2 \left(\frac{2r^2}{w^2} \right) = \\ &= \frac{\pi w_0^2}{2} |G(0)|^2 \int_0^\infty dx x^m e^{-x} L_{pm}^2(x). \end{aligned}$$

The remaining integral is trivial if we take a look at the orthogonality relation of the associated Laguerre polynomials

$$\int_0^\infty dx x^m e^{-x} L_{pm}(x) L_{p'm}(x) = \frac{(p+m)!}{p!} \delta_{pp'}. \quad (1.119)$$

This gives the result

$$G(0) = \sqrt{\frac{p!}{(p+m)!}}. \quad (1.120)$$

The final expressions for the electric field, after dealing with normalization, are simply

$$E_x^{pm}(r, z, \varphi) = E_x(r, z) \sqrt{\frac{p!}{(|m|+p)!}} \left(\frac{\sqrt{2}r}{w(z)} \right)^{|m|} L_{p|m|} \left(\frac{2r^2}{w^2(z)} \right) \exp \left(i(2p+|m|) \arctan \left(\frac{z}{z_0} \right) \right) e^{-im\varphi} \quad (1.121a)$$

$$E_y^{pm}(r, z, \varphi) = E_y(r, z) \sqrt{\frac{p!}{(|m|+p)!}} \left(\frac{\sqrt{2}r}{w(z)} \right)^{|m|} L_{p|m|} \left(\frac{2r^2}{w^2(z)} \right) \exp \left(i(2p+|m|) \arctan \left(\frac{z}{z_0} \right) \right) e^{-im\varphi} \quad (1.121b)$$

$$E_z^{pm}(r, z, \varphi) = -\frac{i}{k} (\partial_x E_x^{pm}(r, z, \varphi) + \partial_y E_y^{pm}(r, z, \varphi)), \quad (1.121c)$$

where $E_x(r, z)$ and $E_y(r, z)$ are to be taken from the Gaussian beam (1.97). For the sake of use in numerical simulations (mainly to eliminate the need for numerical differentiation) the z component of the field can be computed explicitly to be

$$\begin{aligned} E_z^{pm} = & -\frac{i}{k} \left(-2 \frac{1+i\frac{z}{z_0}}{w^2(z)} + \frac{\partial L_{p|m|} \left(\frac{2r^2}{w^2(z)} \right)}{L_{p|m|} \left(\frac{2r^2}{w^2(z)} \right)} \right) (xE_x^{pm} + yE_y^{pm}) - \\ & -\frac{i}{k} \sqrt{\frac{p!}{(|m|+p)!}} \left(\frac{\sqrt{2}}{w(z)} \right)^{|m|} L_{p|m|} \left(\frac{2r^2}{w^2(z)} \right) \exp \left(i(2p+|m|) \arctan \left(\frac{z}{z_0} \right) \right) (T_x E_x + T_y E_y), \end{aligned} \quad (1.122)$$

with

$$T_x = \begin{cases} l(x-iy)^{l-1}, & l > 0 \\ 0, & l = 0 \\ -l(x+iy)^{-l-1}, & l < 0 \end{cases} \quad (1.123a)$$

$$T_y = \begin{cases} -il(x-iy)^{l-1}, & l > 0 \\ 0, & l = 0 \\ -il(x+iy)^{-l-1}, & l < 0. \end{cases} \quad (1.123b)$$

The magnetic field is derived exactly as in the case of the Gaussian beam

$$B_x(r, z, \varphi) = -\frac{1}{c} E_y(r, z, \varphi) \quad (1.124a)$$

$$B_y(r, z, \varphi) = \frac{1}{c} E_x(r, z, \varphi) \quad (1.124b)$$

$$B_z(r, z, \varphi) = -\frac{i}{ck} [\partial_y E_x(r, z, \varphi) - \partial_x E_y(r, z, \varphi)]. \quad (1.124c)$$

The explicit third component of \mathbf{B} is

$$B_z^{pm} = -\frac{i}{ck} \left(-2 \frac{1 + i \frac{z}{z_0}}{w^2(z)} + \frac{\partial L_{p|m|} \left(\frac{2r^2}{w^2(z)} \right)}{L_{p|m|} \left(\frac{2r^2}{w^2(z)} \right)} \right) (y E_x^{pm} - x E_y^{pm}) - \\ - \frac{i}{ck} \sqrt{\frac{p!}{(|m|+p)!}} \left(\frac{\sqrt{2}}{w(z)} \right)^{|m|} L_{p|m|} \left(\frac{2r^2}{w^2(z)} \right) \exp \left(i(2p+|m|) \arctan \left(\frac{z}{z_0} \right) \right) (T_y E_x - T_x E_y). \quad (1.125)$$

These expressions are easier to derive if we bring together the terms $\left(\frac{\sqrt{2}r}{w(z)} \right)^{|m|}$ and $e^{-im\varphi}$ and replace $r e^{\pm i\varphi}$ with $x \pm iy$ before computing the derivatives. This step also helps to eliminate the apparent singularity that might appear on the z-axis.

Be aware that $\partial L_{p|m|}$ is not the derivative of the Laguerre generalized polynomial with respect to anything, but rather a notation for the common factor of the partial derivatives with respect to x and y . Its expression is

$$\partial L_{p|m|} \left(\frac{2r^2}{w^2(z)} \right) = \begin{cases} -\frac{4}{w^2(z)} L_{p-1,|m|+1} \left(\frac{2r^2}{w^2(z)} \right), & 1 \leq p \\ 0, & \text{otherwise.} \end{cases} \quad (1.126)$$

Of course, in order to use these relations in simulations involving laser beams, one must attach also the temporal profile (1.103).

It is important to mention that the Laguerre-Gauss laser beams are not simply a solution resulting from mathematical sleight of hand. They can be obtained in practice. Some examples of articles that deal with the production of Laguerre-Gauss modes (only a few selected from an expansive literature) are Bolze and Nuernberger 2018, Sueda *et al.* 2004 and Zeylikovich *et al.* 2007.

Just for the sake of completion, I have also added a couple of figures illustrating different Laguerre-Gauss profiles (1.3). The plots were obtained in Julia, with the help of the LaserTypes.jl package (available at <https://github.com/SebastianM-C/LaserTypes.jl>). The code is very similar to the examples used in the documentation of the package (which I helped designing). Note that for $m = p = 0$, the profile is the same as for a regular Gauss mode, so the illustrations provide an example for that as well.

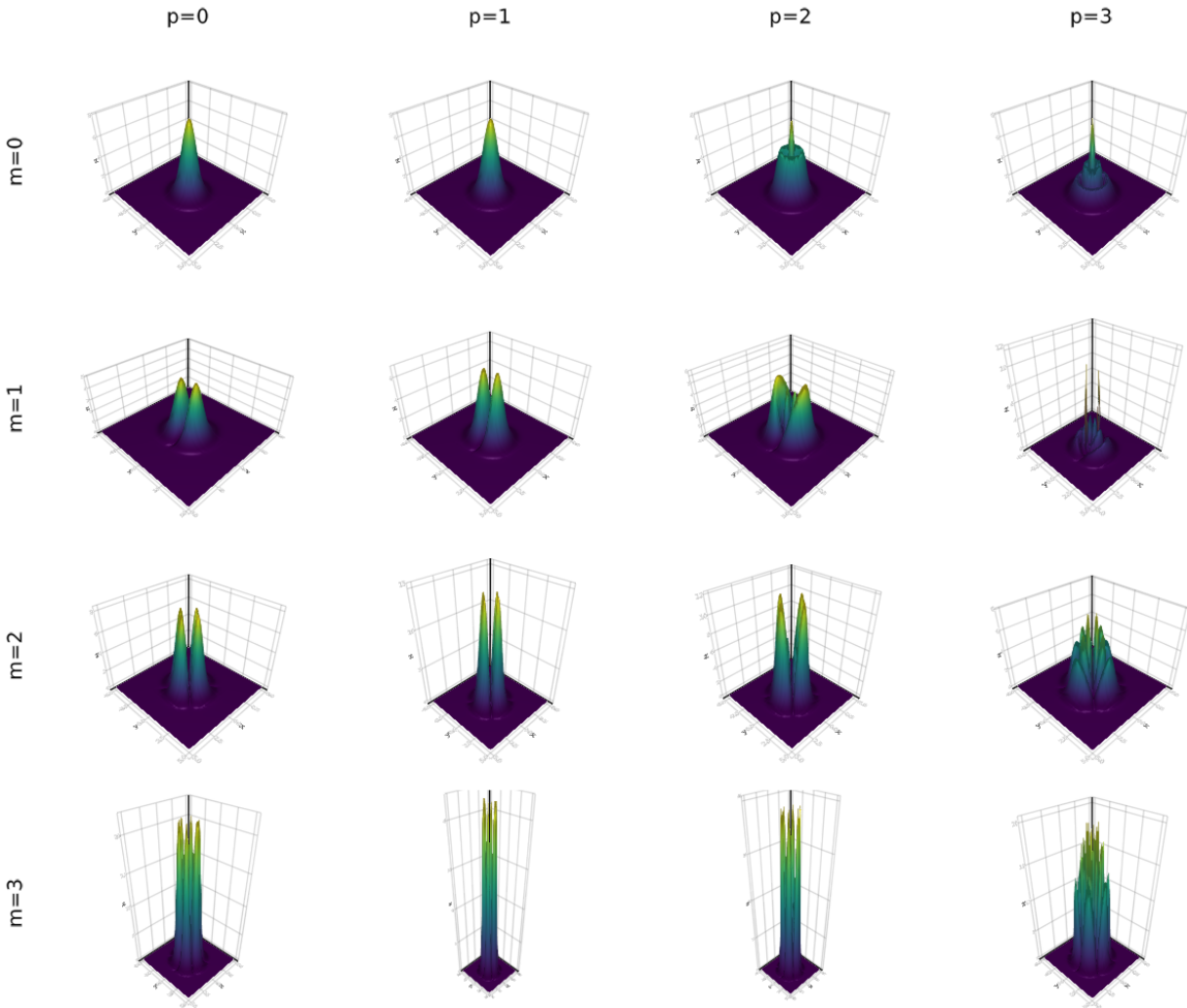


Figure 1.3: The surface plots of the modulus of the electric field vector evaluated at $z = z_0$ for different Laguerre-Gauss profiles

1.2.7 Other Types of Beams

Hermite-Gauss Beams

One can also work directly in Cartesian coordinates in order to solve the paraxial wave equation. This will lead to obtaining the rectangular Gauss beam mode. The extension of this solution, in the same manner used to extend the cylindrical mode to the Laguerre-Gauss mode, is the Hermite-Gauss beam and, as the name suggests, uses the Hermite polynomials. However, these modes are not of interest in our endeavours. If the reader is interested to look upon them, the book by Goldsmith 1998 has a very concise and straightforward presentation of them in its first chapter.

Bessel Beams

These are a direct solution to the paraxial equation without axial symmetry. These beams have two noteworthy and peculiar properties: they are immune (at least to some degree) to diffraction and they can “heal” after being obstructed by an obstacle. A good summary on how

they are described and how their properties manifest are found in the fifth chapter of S Simon 2016.

1.3 Angular Momentum of Electromagnetic Waves

In this section I will simply mention how the orbital angular momentul can be defined. A thorough derivation of its expression for each of the presented laser profiles is simple, but rather lengthy and redundant work. If one is interested in computing it in numerical simulations (which is the case for the present thesis), it can be computed from the values of the fields.

By having the electromagnetic momentum defined in (1.39), we can simply extend the expression of the angular momentum as is used in classical mechanics to our case, such that we have

$$\mathbf{J} = \varepsilon_0 \int d\mathbf{r} \mathbf{r} \times (\mathbf{E} \times \mathbf{B}) \quad (1.127)$$

Details about the actual derivation and how to apply this definition in particular cases are found in Belinfante 1940 and Humblet 1943.

Chapter 2

The Interaction Between Electromagnetic Radiation and Matter

Now that the aspects related to the formalism and theory behind the modeling of laser produced electromagnetic waves has been presented, we must naturally turn our attention towards the interaction of those wave pulses with matter. This chapter only deals with the dynamics of particles under the action of electromagnetic fields and the ponderomotive force, since these topics offer great insight and intuition for the physical behaviour of high intensity laser-plasma interaction. The specific phenomena arising from the properties of plasma as a medium are to be presented later.

2.1 Electron Dynamics in Electromagnetic Fields

This section deals with analyzing the motion of a single electron in the fields of a wave. For simplicity, I will only talk about the case of linearly polarized plane waves, since this entire discussion has the purpose of building up intuition and getting a feel for the scale of the relevant quantities. Most of what is to be presented is following the lecture notes of Karsch 2018.

The fact that we want to study dynamics and we are using a very simple type of wave means that it is actually more convenient this time around to work with real fields, rather than complex ones. As per usual, the direction of propagation is chosen to be the z-axis such that the fields are

$$\mathbf{E} = \mathbf{e}_x E_0 \cos(kz - \omega t) \quad (2.1a)$$

$$\mathbf{B} = \mathbf{e}_y B_0 \cos(kz - \omega t). \quad (2.1b)$$

Just as an exercise, it can be observed that these fields are generated by the following choice for the 4-potential

$$\begin{cases} \phi = 0 \\ \mathbf{A} = \mathbf{e}_x A_0 \sin(kz - \omega t), \end{cases} \quad (2.2)$$

where $A_0 = \frac{E_0}{\omega} = \frac{B_0}{k}$.

2.1.1 Classical Treatment

We start from the classical equation of motion given by Newton's second principle using the Lorentz force

$$\frac{d\mathbf{p}}{dt} = \frac{d(m_e \mathbf{v}_e)}{dt} = -e(\mathbf{E} + \mathbf{v}_e \times \mathbf{B}) , \quad (2.3)$$

with m_e and \mathbf{v}_e the mass and the velocity of the electron, respectively, and e the elementary charge. Since we have $B \propto \frac{E}{c}$ and also $v_e \ll c$ (which is implied in order to have a classical treatment), we can safely remove the second term in the right-hand side of the equation above, remaining with

$$\frac{d\mathbf{v}_e}{dt} = -\frac{e}{m_e} \mathbf{E} = -\frac{e}{m_e} E_0 \mathbf{e}_x \cos(kz - \omega t) . \quad (2.4)$$

Simply integrating with initial conditions $x_0, y_0, z_0 = 0$ and $\mathbf{v}_e(\mathbf{0}) = \mathbf{0}$ leads to

$$\mathbf{v}_e(t) = \frac{e}{\omega m_e} E_0 \mathbf{e}_x \sin(kz - \omega t) \quad (2.5a)$$

$$x(t) = \frac{e}{\omega^2 m_e} E_0 [\cos(kz - \omega t) - 1] . \quad (2.5b)$$

It is important now to see when the classical treatment breaks down. Let us impose that

$$v_e^{max} = c , \quad (2.6)$$

such that we have

$$a_0 \equiv \frac{eE_0}{\omega m_e c} = \frac{eA_0}{m_e c} = 1 . \quad (2.7)$$

The parameter a_0 is called the normalized or dimensionless vector potential. From its definition it is easy to see that it can only take values between 0 and 1 (In the classical case only. This definition can be used to compute intensity like described below in any regime.). We can use it to describe the amplitude of the electric field as such

$$E_0 = a_0 \frac{\omega m_e c}{e} . \quad (2.8)$$

It is very convenient in practice to use the wavelength and to extract the rest mass to charge ratio of the electron as follows

$$E_0 = \frac{a_0}{\lambda} 2\pi \frac{m_e c^2}{e} = \frac{a_0}{\lambda} 2\pi \cdot 511 kV . \quad (2.9)$$

The normalized vector field holds also an important significance. One can see that its definition actually boils down to

$$a_0 = \frac{v_{max}^{classical}}{c} , \quad (2.10)$$

so we can use it to find a boundary for the validity of the classical treatment. For simplicity, let's dissect the $a_0 = 1$ case, for which the motion should be completely relativistic, keeping in mind that the classical description stops being reliable well before that. From the result concerning the Poynting vector of a plane wave (1.60), we can find the intensity of the pulse in this limiting case to be

$$I = c \frac{\varepsilon_0}{2} E_0^2 \propto \frac{a_0^2}{\lambda^2} 10^{18} W \frac{\mu m^2}{cm^2} , \quad (2.11)$$

which says that already at intensities of $10^{18} \frac{W}{cm^2}$ the motion of the electron should be treated completely within the grounds of special relativity.

2.1.2 Relativistic Treatment

In the light of our discussion in the previous subsection, we see that in order to study how electrons interact with high-intensity laser beams (namely, terawatt and petawatt lasers), we should do all our calculations relativistically. The equation of motion remains the same, but the relativistic momentum is $\mathbf{p} = \gamma m_e \mathbf{v}_e$, where γ is the usual Lorentz factor. By taking the scalar product of equation (2.3) with \mathbf{p} we get

$$\frac{1}{2} \frac{d\mathbf{p}^2}{dt} = -e \mathbf{p} \cdot \mathbf{E}, \quad (2.12)$$

where we used the fact that $\mathbf{p} \cdot (\mathbf{v}_e \times \mathbf{B})$, since \mathbf{p} is proportional to \mathbf{v}_e . Now, it is useful to write the Lorenz factor in terms of momentum like this

$$\gamma = \frac{1}{\sqrt{1 - \frac{\mathbf{v}^2}{c^2}}} \Rightarrow \frac{1}{\gamma^2} = 1 - \frac{\mathbf{v}^2}{c^2} = 1 - \frac{1}{\gamma^2} \frac{\mathbf{p}^2}{m_e^2 c^2} \Rightarrow \gamma = \sqrt{1 + \left(\frac{\mathbf{p}}{m_e c}\right)^2}.$$

Now we can expect to find $\frac{d\mathbf{p}^2}{dt}$ by taking the derivative of γ with respect to time

$$\begin{aligned} \frac{d\gamma}{dt} &= \frac{d}{dt} \sqrt{1 + \left(\frac{\mathbf{p}}{m_e c}\right)^2} = \frac{1}{\sqrt{1 + \left(\frac{\mathbf{p}}{m_e c}\right)^2}} \frac{1}{m_e^2 c^2} \frac{1}{2} \frac{d\mathbf{p}^2}{dt} = \frac{1}{\gamma m_e^2 c^2} \frac{1}{2} \frac{d\mathbf{p}^2}{dt} \Rightarrow \\ &\Rightarrow m_e c^2 \frac{d\gamma}{dt} = -e \frac{\mathbf{p}}{\gamma m_e} \cdot \mathbf{E} = -e \mathbf{v}_e \cdot \mathbf{E}. \end{aligned}$$

Remembering that the kinetic energy in special relativity is obtained as $K = (\gamma - 1)m_e c^2$, we can reach an equation for it

$$\frac{dK}{dt} = -e \mathbf{v}_e \cdot \mathbf{E}. \quad (2.13)$$

This equation can also be rewritten as

$$\frac{d\gamma}{dt} = -\frac{e E_0}{m_e c} \frac{\mathbf{v}_e \cdot \mathbf{e}_x}{c} \cos(kz - \omega t) = -a_0 \omega \frac{v_x}{c} \cos(kz - \omega t). \quad (2.14)$$

In order to proceed, we should also take a better look at the equation of motion as it is

$$\begin{aligned} \frac{d}{dt} \left(\frac{\mathbf{p}}{m_e c} \right) &= -\frac{e}{m_e c} [E_0 \mathbf{e}_x + B_0 \mathbf{v} \times \mathbf{e}_y] \cos(kz - \omega t) = \\ &= -\frac{e E_0}{m_e c} \left[\mathbf{e}_x + \frac{\mathbf{v}}{c} \times \mathbf{e}_y \right] \cos(kz - \omega t) = \\ &= -a_0 \omega \left[\left(1 - \frac{v_z}{c}\right) \mathbf{e}_x + \frac{v_x}{c} \mathbf{e}_z \right] \cos(kz - \omega t). \end{aligned}$$

By defining $\tilde{\mathbf{p}} = \frac{\mathbf{p}}{m_e c}$ to be the normalized momentum, we can write the equations for its components as follows

$$\frac{d\tilde{p}_x}{dt} = -a_0\omega \left(1 - \frac{v_z}{c}\right) \cos(kz - \omega t) \quad (2.15a)$$

$$\frac{d\tilde{p}_y}{dt} = 0 \quad (2.15b)$$

$$\frac{d\tilde{p}_z}{dt} = -a_0\omega \frac{v_x}{c} \cos(kz - \omega t). \quad (2.15c)$$

The y is trivial, and since we took the initial velocity to be zero, the y -velocity will be zero at all times.

From equations (2.14) and (2.15c) we have the following development

$$\frac{d(\tilde{p}_z - \gamma)}{dt} = 0 \Leftrightarrow \tilde{p}_z - \gamma = C. \quad (2.16)$$

Again, making use of our choice of initial conditions, which translate here as $\gamma(0) = 1$ and $\tilde{p}_z(0) = 0$, we obtain C to be -1.

To summarize so far, we already know that

$$\tilde{p}_y = 0 \quad (2.17a)$$

$$\tilde{p}_z = \gamma - 1. \quad (2.17b)$$

By squaring up the very last equation, yet another useful relation can be derived

$$\gamma = 1 + \tilde{p}_z = \sqrt{1 + \tilde{\mathbf{p}}} \Rightarrow 1 + 2\tilde{p}_z + \tilde{p}_z^2 = 1 + \tilde{p}_x + \tilde{p}_y + \tilde{p}_z$$

$$\tilde{p}_z = \frac{1}{2}\tilde{p}_x^2. \quad (2.18)$$

Since p_z is the normalized momentum along the propagation direction of the wave, we can see that for $\tilde{p}_z = \frac{1}{2}\tilde{p}_x^2 \ll 1$ (classical regime) the transversal momentum is more important, while for $\tilde{p}_z = \frac{1}{2}\tilde{p}_x^2 \gg 1$ (highly relativistic regime) the longitudinal momentum is more important.

Now we would like to find p_x . There is actually a more efficient way to do so than solving equations (2.15a) and (2.15c) together. But for that we shall make use of the electromagnetic potential (2.2). We also need the relations that define the fields from the potential, as detailed in section (1.1.3). With this in mind, we return to the equation of motion

$$\frac{d\mathbf{p}}{dt} = -e(\mathbf{E} + \mathbf{v}_e \times \mathbf{B}) = -e(-\partial_t \mathbf{A} + \mathbf{v}_e \times (\nabla \times \mathbf{A})). \quad (2.19)$$

We make use of the vector identity

$$\mathbf{v} \times (\nabla \times \mathbf{u}) = \nabla(\mathbf{v} \cdot \mathbf{u}) - (\mathbf{v} \cdot \nabla)\mathbf{u}, \quad (2.20)$$

and the total derivative of A with respect to time

$$\frac{d\mathbf{A}}{dt} = \partial_t \mathbf{A} + \partial_{x_i} A^{x_i} \partial_t x_i = \frac{\partial \mathbf{A}}{\partial t} + (\mathbf{v}_e \cdot \nabla) \mathbf{A}. \quad (2.21)$$

Thus,

$$\frac{d\mathbf{p}}{dt} = -e \left[-\frac{d\mathbf{A}}{dt} + (\mathbf{v}_e \cdot \nabla) \mathbf{A} + \nabla(\mathbf{v}_e \cdot \mathbf{A}) - (\mathbf{v}_e \cdot \nabla) \mathbf{A} \right] = -e \left[-\frac{d\mathbf{A}}{dt} + \nabla(\mathbf{v}_e \cdot \mathbf{A}) \right]. \quad (2.22)$$

Since

$$\frac{d\mathbf{A}}{dt} = -\mathbf{e}_x \omega A_0 \cos(kz - \omega t)$$

$$\nabla(\mathbf{v}_e \cdot \mathbf{A}) = \mathbf{e}_z k v_x A_0 \cos(kz - \omega t),$$

we can extract the p_x equation

$$\frac{dp_x}{dt} = -e\omega A_0 \cos(kz - \omega t) = e \frac{dA}{dt}, \quad (2.23)$$

which gives

$$p_x = eA + C'. \quad (2.24)$$

With the initial conditions this becomes

$$p_x = eA = eA_0 \sin(kz - \omega t). \quad (2.25)$$

Bringing together equations (2.17b), (2.18) and (2.25), using the normalized vector potential $a = \frac{eA_0}{m_e c} \sin(kz - \omega t)$

$$K = (\gamma - 1)m_e c^2 = \frac{a^2}{2} m_e c^2 \Rightarrow \gamma = 1 + \frac{a^2}{2}. \quad (2.26)$$

With this, all the puzzle pieces are in place, so we can collect the following results concerning the motion of the electron

$$\gamma = 1 + \frac{a^2}{2} \quad (2.27a)$$

$$\tilde{p}_x = a \quad (2.27b)$$

$$\tilde{p}_y = 0 \quad (2.27c)$$

$$\tilde{p}_z = \frac{a^2}{2}. \quad (2.27d)$$

It is more convenient, and general, to work with the derivative with respect to $\tau = t - \frac{z(t)}{c}$, which is to choose the convenient reference frame of the wave to simplify the computations. This derivative is developed as such

$$\frac{d}{dt} = \frac{d\tau}{dt} \frac{d}{d\tau} = \left(1 - \frac{1}{c} \frac{dz}{dt} \right) \frac{d}{d\tau} = \left(1 - \frac{a^2}{2} \right) \frac{d}{d\tau} = \frac{1}{\gamma} \frac{d}{d\tau}. \quad (2.28)$$

We can also write the phase of a in terms of this time

$$kz - \omega t = kz - \omega\tau - \frac{\omega}{c}z = -\omega\tau. \quad (2.29)$$

A simple substitution gives the equations for the coordinates

$$\frac{dx}{d\tau} = ca \quad (2.30a)$$

$$\frac{dy}{d\tau} = 0 \quad (2.30b)$$

$$\frac{dz}{d\tau} = c \frac{a^2}{2}, \quad (2.30c)$$

which have the solutions (of course using the initial conditions we chose at the begining)

$$x(\tau) = \frac{ca_0}{\omega} [\cos(\omega\tau) - 1] \quad (2.31a)$$

$$y(\tau) = 0 \quad (2.31b)$$

$$z(\tau) = \frac{ca_0^2}{4} \left[\tau - \frac{1}{2\omega} \sin(2\omega\tau) \right]. \quad (2.31c)$$

These results show us that the motion in the transversal plane is the same as in the classical motion. However, the motion on the propagation direction is more complex, being a superposition of an oscillation and a drift motion. The drift velocity $v_{drift} = \langle v_z \rangle = \langle \dot{z} \rangle$ can be computed fairly easy

$$\begin{aligned} z_{drift} &= \frac{ca_0^2}{4}\tau = \frac{ca_0^2}{4} \left(t - \frac{z}{c} \right) = \frac{ca_0^2}{4}t - \frac{a_0^2}{4}z_{drift} \\ z_{drift} &= \frac{ca_0^2}{4} \frac{t}{1 + \frac{a_0^2}{4}} = \frac{ca_0^2}{4 + a_0^2}t \\ v_{drift} &= \frac{ca_0^2}{4 + a_0^2}. \end{aligned} \quad (2.32)$$

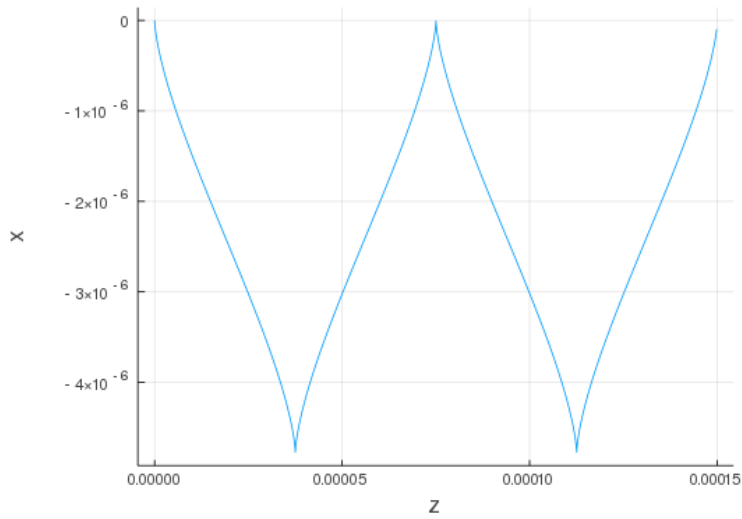


Figure 2.1: The motion in the laboratory frame over two periods of the pulse for some practical parameters: $a_0 = 20$ and $\nu = \frac{\omega}{2\pi} = 400$ THz

In finite length pulses, a certain phenomenon occurs. In order to obtain a finite plane wave pulse, we simply add a Gaussian envelope

$$a(\tau) = a_0 \exp\left(-\left(\frac{\tau}{\tau_0}\right)^2\right) \sin(\omega\tau). \quad (2.33)$$

Under the fields given by this potential, the electron starts moving, but it stops when the wave passes it. Thus, although the electron is moved forward, the net energy gain in its interaction with the field is zero. The theoretical calculations that prove this are quite lengthy, so, in order to visualize this effect, I offer a numerical solution of this motion solved using an explicit Euler method in figure 2.2. The step-size used was small enough that the instability of the method is not relevant. The Julia code used is available in the Appendix at the end of the thesis. We can see that the trajectory of the electron converges to a point after a time longer than the pulse duration.

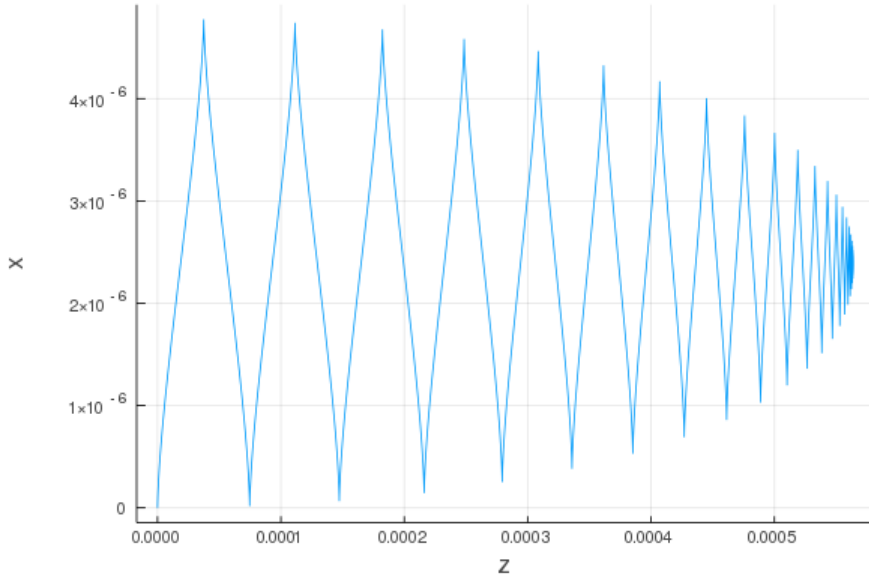


Figure 2.2: The motion in the laboratory frame over a long time compared to the pulse duration τ_0 . The parameters used were: $a_0 = 20$, $\tau_0 = 30$ fs and $\nu = \frac{\omega}{2\pi} = 400$ THz

While a rigorous and complete discussion on dynamics of electrons in wave fields can take an entire book, I will offer here the Lawson-Woodward theorem, which analyzes the possibility for an electron to be accelerated by an electromagnetic wave.

Theorem(Lawson-Woodward)

A relativistic electron does not gain energy from an electromagnetic wave if

- if the interaction takes place in vacuum, in the absence of any walls or any other particles;
- if the electron is in the highly relativistic regime during the entire acceleration process;
- if there are no static electromagnetic fields;
- if the interaction region is infinitely large;
- if the ponderomotive force can be neglected.

If at least one of these conditions are violated, acceleration can happen.

In laser-plasma interaction in particular, all the conditions of this theorem are not valid, which is why the possibility of developing a plasma based, laser powered accelerator is appealing. More on the prospects of this technology will be presented in the next sections.

2.2 The Ponderomotive Force

In this section we will delve into the most relevant physical phenomenon for our studies, namely the ponderomotive force. Intuitively, if we have a focused laser beam, its field will strongly vary in the transverse direction. For an electron that is initially found on the axis of the pulse, the deflection is stronger than the restoring force. Because of this, the electron will be completely removed from the focal region after a couple of oscillations and will retain a non-zero kinetic energy. This effect is called ponderomotive scattering.

2.2.1 Classical Derivation

We already solved the motion of the electron in a plane wave, but for our current purpose, we will need a more general expression for the field. Namely, we would like to have a periodic dependence on time and a spatial dependence of the amplitude

$$\mathbf{E} = \mathbf{E}_0(\mathbf{r}) \cos(\omega t). \quad (2.34)$$

Note that the plane wave field is just a particular case of this ansatz, but now the equation of motion (2.3) is valid only locally, at the electron position \mathbf{r}_0 . Let us approximate the field around \mathbf{r}_0 by Taylor expansion

$$\mathbf{E}_0(\mathbf{r}) = [\mathbf{E}_0(\mathbf{r})]_{\mathbf{r}=\mathbf{r}_0} + [(\delta\mathbf{r} \cdot \nabla)\mathbf{E}_0(\mathbf{r})]_{\mathbf{r}=\mathbf{r}_0} + \mathcal{O}(\delta\mathbf{r}^2). \quad (2.35)$$

From the Maxwell equation $\partial_t \mathbf{B} = -\nabla \times \mathbf{E}$, by integration over time, we can also find the magnetic field

$$\mathbf{B}(\mathbf{r}) = \frac{1}{c} [\mathbf{e}_z \times \mathbf{E}_0(\mathbf{r})]_{\mathbf{r}=\mathbf{r}_0} \cos(\omega t) - \frac{1}{\omega} [\nabla \times \mathbf{E}_0(\mathbf{r})]_{\mathbf{r}=\mathbf{r}_0} \sin(\omega t). \quad (2.36)$$

We can now write the equation of motion in first order and in second order, respectively

$$m_e \frac{d\mathbf{v}^{(0)}}{dt} = -e \left[\mathbf{E}_0(\mathbf{r}_0) \cos(\omega t) + \frac{\mathbf{v}^{(0)}}{c} \times (\mathbf{e}_z \times \mathbf{E}_0(\mathbf{r}_0)) \cos(\omega t) \right] \approx -e \mathbf{E}_0(\mathbf{r}_0) \cos(\omega t) \quad (2.37a)$$

$$m_e \frac{d\mathbf{v}^{(1)}}{dt} = -e [(\delta\mathbf{r} \cdot \nabla)\mathbf{E}_0(\mathbf{r})]_{\mathbf{r}=\mathbf{r}_0} \cos(\omega t) + e \frac{1}{\omega} \mathbf{v}^{(0)} \times [\nabla \times \mathbf{E}_0(\mathbf{r})]_{\mathbf{r}=\mathbf{r}_0} \sin(\omega t), \quad (2.37b)$$

where $\frac{d(\delta\mathbf{r})}{dt} = \mathbf{v}^{(0)}$ and we have used the fact that $v^{(0)} \ll c$. Equation (2.37a) is solved by direct integration

$$\mathbf{v}^{(0)} = -\frac{e}{m_e \omega} \mathbf{E}_0(\mathbf{r}_0) \sin(\omega t) \quad (2.38a)$$

$$\delta\mathbf{r} = \frac{e}{m_e \omega^2} \mathbf{E}_0(\mathbf{r}_0) \cos(\omega t). \quad (2.38b)$$

These are pretty much the results from the plane wave, that is, the oscillatory motion induced by the wave on the electron. The second order equation describes an additional effect that arises. Replacing the above solutions in equation (2.37b) leads to

$$m_e \frac{d\mathbf{v}^{(1)}}{dt} = -\frac{e^2}{m_e \omega^2} [(\mathbf{E}_0 \cdot \nabla) \mathbf{E}_0 \cos^2(\omega t) + \mathbf{E}_0 \times (\nabla \times \mathbf{E}_0) \sin^2(\omega t)]_{\mathbf{r}=\mathbf{r}_0}. \quad (2.39)$$

So far this discussion followed the microscopic motion. We are interested in average effects, so we should find the time average of the expression obtained. Keeping in mind that both the averages of sine squared and cosine squared over one period are one half, we can deduce that

$$\left\langle m_e \frac{d\mathbf{v}^{(1)}}{dt} \right\rangle_T = -\frac{e^2}{2m_e \omega^2} [(\mathbf{E}_0 \cdot \nabla) \mathbf{E}_0 + \mathbf{E}_0 \times (\nabla \times \mathbf{E}_0)]_{\mathbf{r}=\mathbf{r}_0}, \quad (2.40)$$

where $T = \frac{2\pi}{\omega}$. We apply now the vector identity (2.20) and the fact that $\nabla \mathbf{v}^2 = 2\mathbf{v}(\nabla \cdot \mathbf{v})$ to reach the final result

$$\left\langle m_e \frac{d\mathbf{v}^{(1)}}{dt} \right\rangle_T = -\frac{e^2}{4m_e \omega^2} \nabla \mathbf{E}_0^2 = \mathbf{F}_{\text{pond}}, \quad (2.41)$$

which gives the expression of the ponderomotive force \mathbf{F}_{pond} .

2.2.2 Relativistic Ponderomotive Force

We already saw that for high intensity lasers the classical treatment is insufficient. In the case of the ponderomotive force a relativistic derivation leads to the same dependence on the field. More precisely, the ponderomotive force is directly proportional to the gradient of the squared electric field. Nonetheless, I will try to present in this section a rigorous relativistic treatment based on the discussion in the 5th chapter of Mulser and Bauer 2010.

We will start with the Lagrangian for an electron in an arbitrary 4-vector potential (ϕ, \mathbf{A})

$$L(\mathbf{x}, \mathbf{v}, t) = -\frac{m_e c^2}{\gamma} - e\mathbf{v} \cdot \mathbf{A} + e\phi. \quad (2.42)$$

Since our system has an oscillatory part given by the periodic time dependence of the 4-vector potential of the driving electromagnetic wave, we can change to action-angle variables $S = S(\mathbf{x}, t)$ and $\eta = \eta(\mathbf{x}, t)$, which are Lorentz invariant, so the motion will be governed by Hamilton's principle

$$\delta S = \delta \int_{\eta_i}^{\eta_f} d\eta L(\mathbf{x}(\eta), \mathbf{v}(\eta), t(\eta)) \frac{dt}{d\eta}. \quad (2.43)$$

This change of variables introduces a new Lagrangian (a “Lagrangian angular density” if you want)

$$\mathcal{L}(\eta) = \frac{L(\eta)}{\frac{d\eta}{dt}}. \quad (2.44)$$

With all these things set up and choosing η to be normalized to 2π , we introduce the cycle averaged Lagrangian

$$\mathcal{L}_0(\eta) = \frac{1}{2\pi} \int_{\eta}^{\eta+2\pi} d\eta' \mathcal{L}(\eta'). \quad (2.45)$$

We denote by $N = \frac{n_f - n_i}{2\pi}$ to be the number of cycles over which \mathcal{L}_0 undergoes a significant change. We are interested now to see how N imposes a boundary on the action of \mathcal{L}_0 . From equations (2.43) and (2.44) we see that

$$\delta \int_{\eta_i}^{\eta_f} d\eta \mathcal{L} = 0,$$

which is useful in order to make the following mathematical arguments

$$\begin{aligned} \left| \delta \int_{\eta_i}^{\eta_f} d\eta \mathcal{L}_0 \right| &= \left| \delta \int_{\eta_i}^{\eta_f} d\eta (\mathcal{L}_0 - \mathcal{L}) \right| = \left| \int_{\eta_i}^{\eta_f} d\eta \delta(\mathcal{L}_0 - \mathcal{L}) \right| = \\ &= \left| \int_{\eta_i}^{\eta_f} d\eta [\mathcal{L}_0(\eta + \delta\eta) - \mathcal{L}(\eta + \delta\eta)] - \int_{\eta_i}^{\eta_f} d\eta [\mathcal{L}_0(\eta) - \mathcal{L}(\eta)] \right| \leq \\ &\leq \sum_{n=1}^N \left| \int_{\eta_n}^{\eta_n+2\pi} d\eta [\mathcal{L}_0(\eta + \delta\eta) - \mathcal{L}(\eta + \delta\eta)] - \int_{\eta_n}^{\eta_n+2\pi} d\eta [\mathcal{L}_0(\eta) - \mathcal{L}(\eta)] \right|, \end{aligned}$$

where we discretized the angle variable as $\eta_n = \eta_i + 2\pi n$, $n \in \mathbb{N}^*$ and used the triangle inequality for the modulus. We will now replace \mathcal{L} from equation (2.45) and continue our endeavours

$$\begin{aligned} \left| \delta \int_{\eta_i}^{\eta_f} d\eta \mathcal{L}_0 \right| &\leq \sum_{n=1}^N \left| \int_{\eta_n}^{\eta_n+2\pi} d\eta \mathcal{L}_0(\eta + \delta\eta) - 2\pi \mathcal{L}_0(\eta_n + \delta\eta_n) - \int_{\eta_n}^{\eta_n+2\pi} d\eta \mathcal{L}_0(\eta) - 2\pi \mathcal{L}_0(\eta_n) \right| = \\ &= \sum_{n=1}^N \left| \int_{\eta_n}^{\eta_n+2\pi} d\eta [\mathcal{L}_0(\eta + \delta\eta) - \mathcal{L}_0(\eta)] - 2\pi [\mathcal{L}_0(\eta_n + \delta\eta_n) - \mathcal{L}_0(\eta_n)] \right| \approx \\ &\approx \sum_{n=1}^N \left| \int_{\eta_n}^{\eta_n+2\pi} d\eta \frac{\partial \mathcal{L}_0(\eta)}{\partial \eta} \delta\eta - 2\pi \frac{\partial \mathcal{L}_0(\eta_n)}{\partial \eta_n} \delta\eta_n \right|, \end{aligned}$$

where we kept only the first terms in $\delta\eta$ and $\delta\eta_n$. Now, it is time to use the mean value theorem to evaluate the integral

$$\int_{\eta_n}^{\eta_n+2\pi} d\eta \frac{\partial \mathcal{L}_0(\eta)}{\partial \eta} \delta\eta = 2\pi \frac{\partial \mathcal{L}_0(\eta_n^c)}{\partial \eta_n^c} \delta\eta_n^c,$$

with $\eta_n^c \in (\eta_n, \eta_n + 2\pi)$, to obtain

$$\left| \delta \int_{\eta_i}^{\eta_f} d\eta \mathcal{L}_0 \right| \leq 2\pi \sum_{n=1}^N \left| \frac{\partial \mathcal{L}_0(\eta_n^c)}{\partial \eta_n^c} \delta\eta_n^c - \frac{\partial \mathcal{L}_0(\eta_n)}{\partial \eta_n} \delta\eta_n \right| = 2\pi \sum_{n=1}^N \left| \left[\frac{\partial \mathcal{L}_0(\eta)}{\partial \eta} \delta\eta \right]_{\eta=\eta_n^c} - \left[\frac{\partial \mathcal{L}_0(\eta)}{\partial \eta} \delta\eta \right]_{\eta=\eta_n} \right|.$$

We can also use a first order expansion to simplify the quantity in the modulus

$$\begin{aligned} &\left| \left[\frac{\partial \mathcal{L}_0(\eta)}{\partial \eta} \delta\eta \right]_{\eta=\eta_n^c} - \left[\frac{\partial \mathcal{L}_0(\eta)}{\partial \eta} \delta\eta \right]_{\eta=\eta_n} \right| = \\ &= \left| \left[\frac{\partial \mathcal{L}_0(\eta)}{\partial \eta} \delta\eta \right]_{\eta=\eta_n^c} - \left[\frac{\partial \mathcal{L}_0(\eta)}{\partial \eta} \delta\eta \right]_{\eta=\eta_n^c} - \left[\frac{\partial^2 \mathcal{L}_0(\eta)}{\partial \eta^2} \delta\eta \right]_{\eta=\eta_n^c} (\eta_n - \eta_n^c) \right| = \end{aligned}$$

$$\begin{aligned}
&= \left| \left[\frac{\partial^2 \mathcal{L}_0(\eta)}{\partial \eta^2} \delta \eta \right]_{\eta=\eta_n^c} \right| |\eta_n - \eta_n^c| \leq \\
&\leq 2\pi \left| \left[\frac{\partial^2 \mathcal{L}_0(\eta)}{\partial \eta^2} \delta \eta \right]_{\eta=\eta_n^c} \right|,
\end{aligned}$$

so that in the end we remain with

$$\left| \delta \int_{\eta_i}^{\eta_f} d\eta \mathcal{L}_0 \right| \leq (2\pi)^2 \sum_{n=1}^N \left| \left[\frac{\partial^2 \mathcal{L}_0(\eta)}{\partial \eta^2} \right]_{\eta=\eta_n^c} \right| |\delta \eta_n^c| \leq (2\pi)^2 N \max \left\{ \left| \left[\frac{\partial^2 \mathcal{L}_0(\eta)}{\partial \eta^2} \right]_{\eta=\eta_n^c} \right| \right\} \max \{ |\delta \eta_n^c| \}. \quad (2.46)$$

We would want now to impose the condition that \mathcal{L}_0^{\max} changes at most by \mathcal{L}_0 over N cycles, that is

$$N = \frac{1}{2\pi} \frac{|\mathcal{L}_0^{\max}|}{\max \left\{ \left| \left[\frac{\partial \mathcal{L}_0(\eta)}{\partial \eta} \right]_{\eta=\eta_n^c} \right| \right\}}. \quad (2.47)$$

By imposing a similar constraint on the first derivative

$$2\pi \frac{\max \left\{ \left| \left[\frac{\partial^2 \mathcal{L}_0(\eta)}{\partial \eta^2} \right]_{\eta=\eta_n^c} \right| \right\}}{\max \left\{ \left| \left[\frac{\partial \mathcal{L}_0(\eta)}{\partial \eta} \right]_{\eta=\eta_n^c} \right| \right\}} \leq \frac{1}{N}, \quad (2.48)$$

we obtain that the action of \mathcal{L}_0 is bounded by a function $\mathcal{O}(N^{-1})$

$$\left| \delta \int_{\eta_i}^{\eta_f} d\eta \mathcal{L}_0 \right| \leq \frac{|\mathcal{L}_0^{\max}|}{N} \max \{ |\delta \eta| \}. \quad (2.49)$$

Let us observe that for the regular averaged lagrangian defined by $L_0 = \mathcal{L}_0 \frac{d\eta}{dt}$ we have

$$\int_{\eta_i}^{\eta_f} d\eta \mathcal{L}_0 = \int_{t_i}^{t_f} dt L_0. \quad (2.50)$$

If this would be zero, we would get an Euler-Lagrange set of equations for L_0

$$\frac{d}{dt} \left(\frac{\partial L_0}{\partial \mathbf{v}_0} \right) - \frac{\partial L_0}{\partial \mathbf{x}_0} = 0, \quad (2.51)$$

where the coordinates \mathbf{x}_0 and \mathbf{v}_0 correspond to the oscillation center. However, working with the inequality (2.49) we would obtain an extra term in the right-hand side of equation (2.51) whose absolute value does not exceed

$$\frac{|\mathcal{L}_0^{\max}|}{N^2} \max \{ |\delta \eta| \}.$$

If the Lagrangian \mathcal{L}_0 doesn't depend on time, energy is conserved on average in time and the right-hand side of equation (2.51) is adiabatically zero. For $N \rightarrow \infty$ it is exactly zero. This extra term is the generalized force associated to the ponderomotive force.

The relativistic Hamiltonian obtained from equation (2.42) by the definition $H(\mathbf{x}, \mathbf{p}, t) = \mathbf{p}\mathbf{v} - L(H(\mathbf{x}, \mathbf{v}, t))$ is

$$H = \sqrt{m^2 c^4 + c^2 (\mathbf{p} + e\mathbf{A})^2} - e\phi, \quad (2.52)$$

with the canonical momentum defined as

$$\mathbf{p} = \frac{\partial L}{\partial \mathbf{v}} = \gamma m \mathbf{v} - e\mathbf{A}. \quad (2.53)$$

By defining the effective mass as

$$m_{eff} = \frac{\gamma_0 \mathcal{L}_0 \frac{d\eta}{dt}}{c^2} = \frac{\gamma_0 L_0}{c^2}, \quad (2.54)$$

we obtain that the Lagrangian and Hamiltonian in an arbitrary reference system in which the oscillation center moves with velocity \mathbf{v}_0 are those of a free particle with an effective mass that depends on space-time

$$L_0(\mathbf{x}_0, \mathbf{v}_0, t) = -\frac{m_{eff} c^2}{\gamma_0} \quad (2.55a)$$

$$H_0(\mathbf{x}_0, \mathbf{p}_0, t) = \gamma_0 m_{eff} c^2, \quad (2.55b)$$

with $\gamma_0 = \sqrt{1 - \frac{\mathbf{v}_0^2}{c^2}}$ and $\mathbf{p}_0 = \gamma_0 m_{eff} \mathbf{v}_0$. In the oscillation center system, the ponderomotive force is defined as

$$\mathbf{f}_p \equiv \frac{\partial L_0}{\partial \mathbf{x}_0} = -c^2 \nabla m_{eff}. \quad (2.56)$$

For a strong monochromatic electromagnetic wave the effective mass is

$$m_{eff} = m_e \sqrt{1 + \frac{4}{m_e c^2} \mathbf{A}^2}. \quad (2.57)$$

With this, the classical dependence obtained in the previous subsection still holds

$$\mathbf{F}_p \propto \nabla \mathbf{E}^2. \quad (2.58)$$

Chapter 3

Plasma Physics

3.1 The Definition of Plasma

It is common that people, when asked about what plasma is, their definition stops at the fact that it is a **partially ionized gas**. But this is just one of the three defining characteristics. After all, even the air is partially ionized. The other two properties that a medium should satisfy in order to be considered plasma are quasi-neutrality and collective behaviour.

To be **quasi-neutral** means that the medium has an equal number of positive and negative charges in its entire volume, but small deviations from neutrality are possible locally. That is, if n_p , n_e are the positive charge density and the electron density, respectively, in the whole region of the plasma we have $n_p = n_e$, yet in small regions in the space inside we have $n_p \approx n_e$. A small remark should be made here. While I say that the plasma as a whole is neutral, it is so by approximation still. If one starts building plasma by pumping energy into a gaseous medium for example, some of the first ionized electrons can actually escape the medium. It is only after a certain positive charge density has been achieved that no electrons can escape anymore due to Coulomb attraction. Once enough ionization electrons are produced, the charge imbalance becomes incredibly small (*i.e.* $\frac{n_p - n_e}{n_e} \ll 1$). It is though very hard to observe charge imbalance in practice, so we can say that plasma as a whole is neutral. The localized imbalance in turn is not constantly small; it can vary widely due to the disordered motion of the constituent particles, but statistically speaking neutrality is maintained locally when we look at the time averages.

Collective behaviour is a consequence of the fact that the main type of interaction between the particles constituting the plasma, namely Coulomb interaction, is long range. As such, we can say that any particle in the plasma feels all the other particles. This leads to many important properties specific to plasma, like particle and momentum transport. The simplest response is plasma oscillation, which arises when plasma is placed in a constant electric field. The electrons are pushed by the electric field, but the surplus of positive charge left behind pulls them back, creating an oscillatory motion (we should take into consideration that the positive ions are at least a couple thousand times heavier than the electrons, so it is harder to influence their motion). This property also influences the way in which plasma interacts with electromagnetic radiation, giving rise to radiation transport phenomena for example.

It is important to note from the very begining that in a plasma we have quite many different species of particles. The most simple model would only include electrons, neutral atoms and ions that have just one missing electron, but in reality we can have all the possible types of ions (so also with two or more missing electrons) and photons (which arise from the excitations and de-exitations that happen in this very energetic medium).

In the following sections we aim to go deeper into the parameters that characterize plasmas and the basic models for it. The discussion brings together ideas from Karsch 2018 and Mulser and Bauer 2010.

3.2 Temperature

We would like now to study the statistics of electrons. First of all, we should realize that the interparticle distances in plasmas are quite large, but also the temperature needed to sustain ionization is quite high. So high in fact, that working with the Fermi-Dirac statistics is not necessary, since this quantum mechanically derived distribution can be approximated very well by the classical Maxwell-Boltzmann distribution in this particular situation.

The number of electron with x-axis velocity between $v_{e,x}$ and $v_{e,x} + dv_{e,x}$ is then given by

$$f_e(v_{e,x}) dv_{e,x} = n_e \sqrt{\frac{m_e}{2\pi K_B T_e}} e^{-\frac{K_x}{K_B T_e}}, \quad (3.1)$$

where n_e , m_e and T_e are the electrons' density, mass and temperature, respectively, K_B is the Boltzmann constant and $K_x = \frac{m_e v_{e,x}^2}{2}$ is the kinetic energy of the photons. The normalization constant was obtained from the electron density, since $n_e = \int_{-\infty}^{+\infty} dv_{e,x} f_e(v_{e,x})$. This gives an average kinetic energy of

$$K_x^{avg} = \frac{\int_{-\infty}^{+\infty} dv_{e,x} K_x f_e(v_{e,x})}{\int_{-\infty}^{+\infty} dv_{e,x} f_e(v_{e,x})} = \frac{m_e}{2n_e} \int_{-\infty}^{+\infty} dv_{e,x} v_{e,x}^2 f_e(v_{e,x}) = \frac{1}{2} K_B T_e. \quad (3.2)$$

This is extended in 3D easily, since the distribution of velocity in this case should not have any preferential direction

$$K^{avg} = \frac{3}{2} K_B T_e. \quad (3.3)$$

As it can be seen, we can basically treat the electrons inside the plasma as we would an ideal gas and we have obtained that the average kinetic energy is proportional to the temperature.

A simple numerical application shows us that in order to have $K_B T_e = 1$ eV, the temperature would be around 11600 K. Thus, since the ionized electrons are above the energy level of outer bounded states (so above 1 eV), using Kelvin or degrees Celsius is not that handy. In practice, we will rather use eV (energy units) temperature, which is to be converted to the usual temperature by dividing to K_B .

We could actually treat the ions and the neutral atoms inside the plasma in the same manner. Considering this, we must make the remark that we can have different temperature scales in plasmas. While at thermodynamic equilibrium the system of electrons, ions and neutrals should have a uniform temperature, under the action of an electric field, lets say, the motion of the electrons is influenced more than that of the ions due to the difference in mass, while the neutrals are not affected at all, so we have $T_n \neq T_i \neq T_e$. Of course, equilibration between species can be achieved through collisions or radiation emission and absorption. In complete models, one should also consider the temperatures of photons and individual ion subtypes that can appear. Considering this, in general, thermal equilibration can take a long time (How long exactly is hard to say. Even a rough estimate should account for many types of collisions that take place in a plasma. A comprehensive list of the processes occurring can be found in Braithwaite 2000). It is also important to visualize that the temperature can be directional depending on the orientation of the fields we apply.

Regarding the photons in the system, we must point out that they never reach an equilibrium state. That is because photons are not maintained in the plasma like the other forces (say, electrons and ions pulled back in the plasma by Coulomb forces, neutral particles which have to deal with surface effects). This effect is easy to see in practice. Since the photons leave the plasma medium, the plasma itself is radiating light. This property is the basis for building plasma lamps and plasma displays.

3.3 Debye Shielding

In this section we will derive a common criterion for quasi-neutrality. Let us consider an infinite medium filled with plasma at thermal equilibrium, $T = T_e = T_i$ and with one ion species with charge Ze , such that we have $n_e = Zn_i$. We are interested to see what happens if we introduce an infinite plane with constant positive surface charge density σ in this system (see figure 3.1).

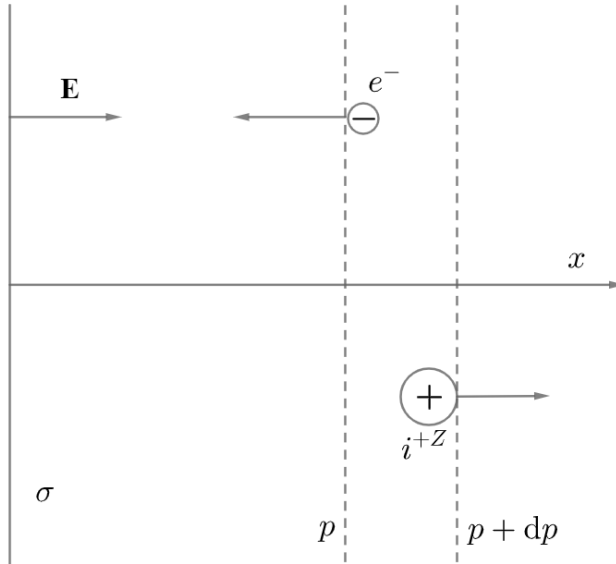


Figure 3.1: A schematic figure that shows the action of introducing the charged sheet in the plasma

The constant electric $E = \frac{\sigma}{2\epsilon_0}$ generated by the plate will act to locally separate sheets of electrons and ions as seen in the figure, until equilibrium between the pressures $p_e = n_e K_B T$ and $p_i = n_i K_B T$ is achieved. For the electrons in a sheet of thickness δx we have

$$dp_e = K_B T dn_e = -en_e E \delta x, \quad (3.4)$$

which can be rewritten as

$$\frac{1}{n_e} \partial_x n_e = -\frac{e}{K_B T} E = \frac{e}{K_B T} \partial_x \phi, \quad (3.5)$$

where ϕ is the electrostatic potential. Solving this equation for the density of electrons, we obtain

$$n_e(x) = \bar{n}_e e^{\frac{e\phi}{K_B T}}, \quad \bar{n}_e = n_e(x \rightarrow \infty). \quad (3.6)$$

In the same manner one obtains a similar expression for the ion density

$$n_i(x) = \frac{\bar{n}_e}{Z} e^{-\frac{Ze\phi}{K_B T}}. \quad (3.7)$$

Writing the Poisson equation in terms of these results gives us

$$\partial_x^2 \phi = \frac{e\bar{n}_e}{\varepsilon_0} \left(e^{\frac{e\phi}{K_B T}} - e^{-\frac{Ze\phi}{K_B T}} \right). \quad (3.8)$$

If the potential energy arising from the field is small compared to the kinetic energy of the particles in the plasma, *i.e.* $e\phi \ll K_B T$, the potential equation can be simplified in approximation to

$$\partial_x^2 \phi = \frac{e\bar{n}_e}{\varepsilon_0} \left(1 + \frac{e\phi}{K_B T} - 1 + \frac{Ze\phi}{K_B T} \right) = \frac{e^2 \bar{n}_e (Z+1)}{\varepsilon_0 K_B T} \phi. \quad (3.9)$$

Obtaining the solution of this differential equation is trivial

$$\phi(x) = \phi_0 e^{-\frac{x}{\lambda_D}}, \quad (3.10)$$

where we introduced the Debye length

$$\lambda_D = \sqrt{\frac{\varepsilon_0 K_B T}{\bar{n}_e e^2 (Z+1)}}. \quad (3.11)$$

This shows us that at a distance of λ_D away from the plate, the electric field generated by it, as well as the corresponding potential, is screened by about 63%. This offers us great insight in how to obtain quasi-neutrality.

From this discussion we can conclude that quasi-neutrality holds if the spatial extension of our ionized gas is at least a couple times larger than the Debye length, since in this case the local deviations from neutrality $n_p \approx n_e$ are screened. For dimensions smaller than λ_D , there is no quasi-neutrality very high-intensity localized fields can occur giving rise to interesting physical phenomena.

In practice, one uses another form for λ_D which neglects the Z and uses the temperature and particle density with more convenient units

$$\lambda_D = \sqrt{\frac{\varepsilon_0 K_B T}{\bar{n}_e e^2}} = 6.9 \sqrt{\frac{T_e [\text{K}]}{n_e [\text{cm}^3]}}, \quad (3.12)$$

the last expression giving λ_D in cm.

3.4 Plasma Frequency

The simplest plasma wave is a longitudinal oscillation of the electrons (caused by an external electric field). Considering how heavy all the other particle species are compared to them, we can treat this problem by considering the ions stationary (in this case the plasma is called a cold plasma). Thus, the electrons simply move in a static positive background. The local changes in electron density cause imbalance and, as we mentioned before, restoring Coulombian forces arise. In what follows we will work purely electrostatic by considering that the electric field is always parallel to the x-axis and the external electric field. We also consider that the electron temperature is close to zero.

We make use of the equation of motion for a single electron, the continuity equation and the Poisson equation

$$m_e \frac{dv_x}{dt} = m_e (\partial_t v_x + v_x \partial_x v_x) = -eE \quad (3.13a)$$

$$\partial_t n_e + \partial_x (n_e v_e) = 0 \quad (3.13b)$$

$$\partial_x E = \frac{e}{\varepsilon_0} (n_p - n_e), \quad (3.13c)$$

where n_p is the positive charge density divided by the unit charge. In equation (3.13a) we can neglect the second term by considering that the velocity is small. We have $v_x \partial_x v_x = \frac{1}{2} \partial_x v_x^2 \approx 0$, since $v_x^2 \ll v_x$ (remember that we work with $T_e \approx 0$), so

$$\partial_t v_x = -\frac{e}{m_e} E. \quad (3.14)$$

Similarly, considering that the particle density is also slowly changing around an equilibrium position $n_0 = n_p$ (*i.e.* $n_e = n_0 + n(x, t)$), we can simplify equation (3.13b)

$$\partial_t n_e + n_0 \partial_x v_x = 0. \quad (3.15)$$

These approximations also change equation (3.13c)

$$\partial_x E = -\frac{e}{\varepsilon_0} n. \quad (3.16)$$

Using a plane wave ansatz for E , v_x and n

$$E = E_0 e^{i(kx - \omega t)} \quad (3.17a)$$

$$v_x = v_0 e^{i(kx - \omega t)} \quad (3.17b)$$

$$n = n_{10} e^{i(kx - \omega t)}, \quad (3.17c)$$

The approximated equation becomes

$$-i\omega v_0 = -\frac{e}{m_e} E_0 \quad (3.18a)$$

$$-i\omega n_{10} + i n_0 k v_0 = 0 \quad (3.18b)$$

$$ikE_0 = -\frac{e}{\varepsilon_0} n_{10}. \quad (3.18c)$$

The frequency ω can be extracted from these relations as follows

$$-i\omega v_0 = -\frac{e}{m_e} E_0 = \frac{e^2}{i\varepsilon_0 k m_e} n_{10} = \frac{e^2}{i\varepsilon_0 k m_e} \frac{k n_0}{\omega} v_0, \quad (3.19)$$

or

$$\omega_p = \sqrt{\frac{n_0 e^2}{\varepsilon_0 m_e}}. \quad (3.20)$$

This is called the cold plasma frequency. This result can be used to derive the plasma waves dispersion relation for the thermal motion of electrons

$$\omega^2 = \omega_p^2 + 3k^2 \frac{K_B T_e}{m_e} = \omega_p^2 + \frac{3}{2} k^2 v_{th}^2, \quad (3.21)$$

where v_{th} is the thermal velocity. As usual, the dispersion relation is useful for finding the phase and group velocities

$$v_{ph} = \frac{\omega}{k} = \sqrt{\frac{\omega_p^2}{k^2} + \frac{3}{2} v_{th}^2} \quad (3.22a)$$

$$v_{gr} = \frac{\partial \omega}{\partial k} = \frac{3}{2} \frac{v_{th}^2}{v_{ph}}. \quad (3.22b)$$

All these velocities satisfy the inequality

$$v_{gr} < \sqrt{\frac{3}{2}} v_{th} < v_{ph}. \quad (3.23)$$

It is also important to remark that the cold plasma frequency (3.20) and the Debye length (3.12) can be related with each other

$$\omega_p \cdot \lambda_D = \sqrt{\frac{K_B T_e}{m_e}} \propto v_{th}. \quad (3.24)$$

3.5 Electromagnetic Waves in Plasma

We will now try to discuss how a plane wave interacts with a plasma medium. We shall start assuming that we have a wave that enters the plasma having the following initial properties

$$\mathbf{E}, \mathbf{B} \propto e^{i(\mathbf{kr} - \omega t)} \quad (3.25a)$$

$$\mathbf{B} = \frac{1}{c} \mathbf{k} \times \mathbf{E}. \quad (3.25b)$$

For simplicity, we will assume that no longitudinal field components arise from the interaction with the plasma. While this may not be a perfectly realistic assumption, the longitudinal components that appear would be very small and would not affect too much the result we obtain.

We will make use of the already familiar Maxwell equations (two of them, to be precise)

$$\nabla \times \mathbf{B} = \mu_0 \mathbf{j} + \frac{1}{c^2} \partial_t \mathbf{E} \Rightarrow \nabla \times (\partial_t \mathbf{B}) = \frac{1}{\epsilon_0 c^2} \partial_t \mathbf{j} + \partial_t^2 \mathbf{E} \quad (3.26a)$$

$$\nabla \times \mathbf{E} = -\partial_t \mathbf{B} \Rightarrow \nabla \times (\nabla \times \mathbf{E}) = \nabla (\nabla \cdot \mathbf{E}) - \nabla^2 \mathbf{E} = -\nabla \times (\partial_t \mathbf{B}). \quad (3.26b)$$

Bringing these results together gives

$$\nabla (\nabla \cdot \mathbf{E}) - \nabla^2 \mathbf{E} + \frac{1}{\epsilon_0 c^2} \partial_t \mathbf{j} + \partial_t^2 \mathbf{E} = 0. \quad (3.27)$$

From equation (3.25) we can compute the derivatives to obtain

$$i \nabla (\mathbf{k} \cdot \mathbf{E}) + k^2 \mathbf{E} - i \frac{\omega}{\epsilon_0 c^2} \mathbf{j} - \frac{\omega^2}{c^2} \mathbf{E} = 0. \quad (3.28)$$

Here the assumption of no longitudinal field component comes in handy and removes the first term, leaving us with

$$(\omega^2 - c^2 k^2) \mathbf{E} = -i \frac{\omega}{\epsilon_0} \mathbf{j}. \quad (3.29)$$

We shall deviate a bit in order to find an expression for the current density. We can find the average electron velocity from the force equation

$$m_e \partial_t \mathbf{v}_e = -e \mathbf{E} \Rightarrow \mathbf{v}_e = \frac{e}{i\omega m_e} \quad (3.30)$$

and introduce it in the definition of the current density in terms of drift velocity

$$\mathbf{j} = -en_0 \mathbf{v}_e. \quad (3.31)$$

By putting together these last three results we obtain the dispersion relation for plane electromagnetic waves in plasma

$$\omega^2 = \omega_p^2 + k^2 c^2. \quad (3.32)$$

From this, obtaining also the phase velocity is trivial

$$v_{ph} = \frac{c}{\sqrt{1 - \frac{\omega_p^2}{\omega^2}}} = \frac{c}{\eta}. \quad (3.33)$$

Here we have also defined the plasma refractive index $\eta = \frac{kc}{\omega}$. It gives very important criteria for propagation of waves in plasma. If $\omega > \omega_p$, then $\eta < 1$ and the wave can propagate through. Otherwise, when $\omega < \omega_p$ and η is imaginary, the wave can not propagate; it will drop exponentially after it enters the plasma medium. The group velocity is also obtained to be

$$v_{gr} = c\eta < c. \quad (3.34)$$

There is also a physical way to think about the possibility of propagation of a wave. If the electromagnetic oscillation occur at a faster rate than that to which the plasma can react, the charged particles in the plasma will not respond fast enough to shield the radiation and it will penetrate. In the oposite case, the incoming radiation is shielded and energy conservation dictates that the wave must be reflected. Whatever small part of the wave would enter the plasma will drop very fast.

3.6 The Vlasov Equation

There is an alternative way to treat the statistics of plasma populations without using the Maxwell-Boltzmann distribution. More precisely, one can derive an equation for the distribution function in phase space. In order to do that, we must start from the Liouville theorem (Arnold 1997, p. 68).

Theorem(Liouville)

The *phase flow* is the one-parameter group of transformations of phase space $g^t : (\mathbf{p}(0), \mathbf{q}(0)) \rightarrow (\mathbf{p}(t), \mathbf{q}(t))$, where $\mathbf{p}(t)$ and $\mathbf{q}(t)$ are solutions of the Hamilton equations. The phase flow preserves the volume of any region. That is, for any region D , $V(g^t D) = V(D)$.

In more layman terms, for a Hamiltonian system, the volume in phase space is conserved in time. In this theorem we also defined the time propagation transformation group $\{g^t\}$. Before delving into the proof of Liouville's theorem let us see that g^t is indeed a group (just as a warming up exercise).

Let $g^{t_a}, g^{t_b} \in \{g^t\}$ three arbitrary transformations (the time t is just a real parameter) and \mathbf{v}, \mathbf{p} solutions of Hamilton's equations. For the closure property we have

$$(g^{t_a} \cdot g^{t_b}) : (\mathbf{p}(0), \mathbf{q}(0)) \equiv g^{t_a} : (g^{t_b} : (\mathbf{p}(0), \mathbf{q}(0))) \equiv g^{t_a} : (\mathbf{p}(t_b), \mathbf{q}(t_b)) \equiv \\ \equiv (\mathbf{p}(t_b + t_a), \mathbf{q}(t_b + t_a)) \equiv g^{t_b + t_a} : (\mathbf{p}(0), \mathbf{q}(0)).$$

We can see from this that composing two transformations gives another transformation whose parameter is the sum of the parameters of the initial transformations. Now it is easy to argue that associativity holds because the parameters are real numbers and their addition is associative. The identity element is g^0 and the inverse of the element g^t is g^{-t} . Even more, this group is abelian. This is consistent to the physical reality of time evolution, since, starting from exactly the same initial conditions, progressing in time first up to t_a and then up to $t_a + t_b$ is equivalent to progressing in time first up to t_b and then up to $t_a + t_b$.

Now let us turn back to proving the theorem. I will denote by $V(t)$ the volume of $D(t)$, where $D(t) = g^t D$ and D is the initial volume. Supposing we have the set on n ordinary differential equations

$$\mathbf{u} = \mathbf{F}(\mathbf{u}), \quad \mathbf{u} = (u_1, u_2, \dots, u_n), \quad (3.35)$$

we can define the corresponding group of transformations $\{g^t\}$ for an infinitesimal time propagation $\delta t \rightarrow 0$ as

$$g^{\delta t} : \mathbf{u} = \mathbf{u} + \mathbf{F}(\mathbf{x})\delta t + \mathcal{O}(\delta t^2). \quad (3.36)$$

In the space of the solutions \mathbf{u} , the initial and final volumes can be written as

$$V(0) = \int_D d\mathbf{u} \quad (3.37a)$$

$$V(\delta t) = \int_{D(\delta t)} d\mathbf{u}(\delta t), \quad (3.37b)$$

with $d\mathbf{u} = du_1 du_2 \dots du_n$. The key argument of the proof is that we can write the integral at time δt using as integration variables the coordinates at time 0 through a change of variables, that is, employing the Jacobian $\frac{\partial g^{\delta t} : \mathbf{u}}{\partial \mathbf{u}}$

$$V(\delta t) = \int_D d\mathbf{u} \left| \frac{\partial g^{\delta t} : \mathbf{u}}{\partial \mathbf{u}} \right|. \quad (3.38)$$

This Jacobian can found from equation (3.36) to be

$$\frac{\partial g^{\delta t} : \mathbf{u}}{\partial \mathbf{u}} = I + \frac{\partial \mathbf{F}}{\partial \mathbf{u}} \delta t + \mathcal{O}(\delta t^2), \quad (3.39)$$

where we denoted with I the corresponding identity matrix.

Here it is obvious that we can employ the Cayley-Hamilton theorem, or rather a direct consequence of it

Theorem

For any matrix A

$$|I + \delta t A| = 1 + \delta t \operatorname{tr} A + \mathcal{O}(\delta t^2), \quad (3.40)$$

when $\delta t \rightarrow 0$.

This immediately gives

$$\left| \frac{\partial g^{\delta t} : \mathbf{u}}{\partial \mathbf{u}} \right| = 1 + \delta t \operatorname{tr} \frac{\partial \mathbf{F}}{\partial \mathbf{u}} + \mathcal{O}(\delta t^2). \quad (3.41)$$

Since $\operatorname{tr} \frac{\partial \mathbf{F}}{\partial \mathbf{u}} = \sum_{i=1}^n \partial_{x_i} F_i = \boldsymbol{\nabla} \cdot \mathbf{F}$, equation (3.38) can be rewritten as

$$V(\delta t) = \int_D d\mathbf{u} (1 + \delta t \boldsymbol{\nabla} \cdot \mathbf{F} + \mathcal{O}(\delta t^2)), \quad (3.42)$$

so the variation in volume in the solution space is (by taking the derivative)

$$\partial_t V = \int_D d\mathbf{u} \boldsymbol{\nabla} \cdot \mathbf{F}. \quad (3.43)$$

In the case of the Hamilton equations

$$\frac{d\mathbf{p}}{dt} = -\frac{\partial H}{\partial \mathbf{q}} \quad (3.44a)$$

$$\frac{d\mathbf{q}}{dt} = \frac{\partial H}{\partial \mathbf{p}}, \quad (3.44b)$$

we have

$$\boldsymbol{\nabla} \cdot \mathbf{F} = \frac{\partial}{\partial \mathbf{p}} \left(-\frac{\partial H}{\partial \mathbf{q}} \right) + \frac{\partial}{\partial \mathbf{q}} \left(\frac{\partial H}{\partial \mathbf{p}} \right) = 0, \quad (3.45)$$

which proves the Liouville theorem.

Now, finding the Vlasov equation is only a matter of using basic and principial statistical mechanics reasoning. If we have a system of particles obeying Hamiltonian dynamics, the probability to find the phase point of this system in a certain volume element $d\mathbf{p} d\mathbf{q}$ in phase space is denoted as $w(d\mathbf{p} d\mathbf{q})$. This can be written in terms of a distribution function ρ as $w(d\mathbf{p} d\mathbf{q}) = \rho(\mathbf{p}, \mathbf{q}, t) d\mathbf{p} d\mathbf{q}$. Since at equilibrium, w is constant, we can conclude that

$$\rho(\mathbf{p}, \mathbf{q}, t) d\mathbf{p} d\mathbf{q} = \rho(\mathbf{p}_0, \mathbf{q}_0, t_0) d\mathbf{p}_0 d\mathbf{q}_0, \quad (3.46)$$

or, using Liouville's theorem,

$$\frac{d\rho}{dt} = 0 = \frac{\partial \rho}{\partial t} + \frac{\partial \mathbf{p}}{\partial t} \frac{\partial \rho}{\partial \mathbf{p}} + \frac{\partial \mathbf{q}}{\partial t} \frac{\partial \rho}{\partial \mathbf{q}}. \quad (3.47)$$

While this equation is sometimes called the Liouville equation, Boltzmann was the first to use it for the purpose of statistical physics. In the original Boltzmann equation, a collision term is considered. For plasma, this collision term is neglected, since the intercation mechanism is the long range Coulomb force. The colisionless Boltzmann equation is named the Vlasov equation, since Anatoly Vlasov was the first to implement this formalism in studies of plasma physics.

Since \mathbf{p} and \mathbf{q} are functions of time only, their partial derivatives can be written as total derivatives. Using Newton's second principle and defining the forces acting on the particles as \mathbf{f} , we can stylize the Vlasov equation so it may look more familiar (Feix and Bertrand 2005)

$$\frac{\partial \rho}{\partial t} + \mathbf{f} \cdot \frac{\partial \rho}{\partial \mathbf{p}} + \mathbf{v} \cdot \frac{\partial \rho}{\partial \mathbf{r}} = 0. \quad (3.48)$$

An important remark must be made. The distribution function ρ is actually one that describes all the particles in the system together. In practice, in order to ease the process of solving this equation, one uses the approximation that this equation is valid for the single-particle distribution. The interaction between particles is reintroduced by including in the scalar potential the contribution of each particle (Silim and Büchner 2003). While this is a better way of describing the plasma system than using the Canonical ensemble (*i.e.* the Maxwell-Boltzmann statistics), this approximation neglects some inherent correlations that exist in real systems.

3.7 Two Stream Instability

In this chapter we present the results from a sample Particle in Cell simulation that can be found in the documentation (*Basic Examples of Using EPOCH* 2020) for the software we are using, EPOCH. The main purpose is to test that the code itself is working properly while also learning some extra stuff about plasma physics.

The figures 3.2 and 3.3 illustrate this effect in phase space. Two streams of electrons with the same drift velocity and particle densities are set to move in opposite directions. The images were obtained through a 1D Particle in Cell simulation in EPOCH with periodic boundary conditions. More on the EPOCH software and how to use it can be found in chapter 4. Red points represent the particles going to the right, while blue points represent the particles going to the left.

Before delving into the mathematical description of this phenomenon, I will present a qualitative explanation for it, as I understood it from the considerations I found in the seventh chapter of Stix and Stix 1992. Suppose we have two counter-flowing streams of charged particles (they can be both electrons, one electron and one ion, it doesn't make a difference). If a point of disturbance appears, a plasma wave will start emanating from it and it will propagate in the medium. The electric field of this wave accelerates the beam particles and some of those will be carried back to the initial disturbance center by the zero-order streaming motion. During the time it takes to reach the disturbance point, the coherent acceleration they are undergoing is generating a fluctuation in their density. When the phase of this fluctuation has the right value, the initial disturbance is amplified. The production of these fluctuations in density is named bunching and it distinguishes itself as a velocity dependent process. This means that plasma components with different velocities will be bunching with different amplitudes and phases.

For what follows, we will treat the beams as collisionless continuous cold fluids of charged particles. We will only deal with two beams, although an analogous treatment can be done for three or more. The electric field is assumed to have a null zero order approximation, since no external field is present in the system. The zero order particle densities and velocities will be denoted with capital letters (N and V , respectively), while the first order parts will be denoted with lowercase letters (n , v). The first order functions are assumed to have a dependence of the form

$$e^{i(\mathbf{k} \cdot \mathbf{r} - \omega t)}.$$

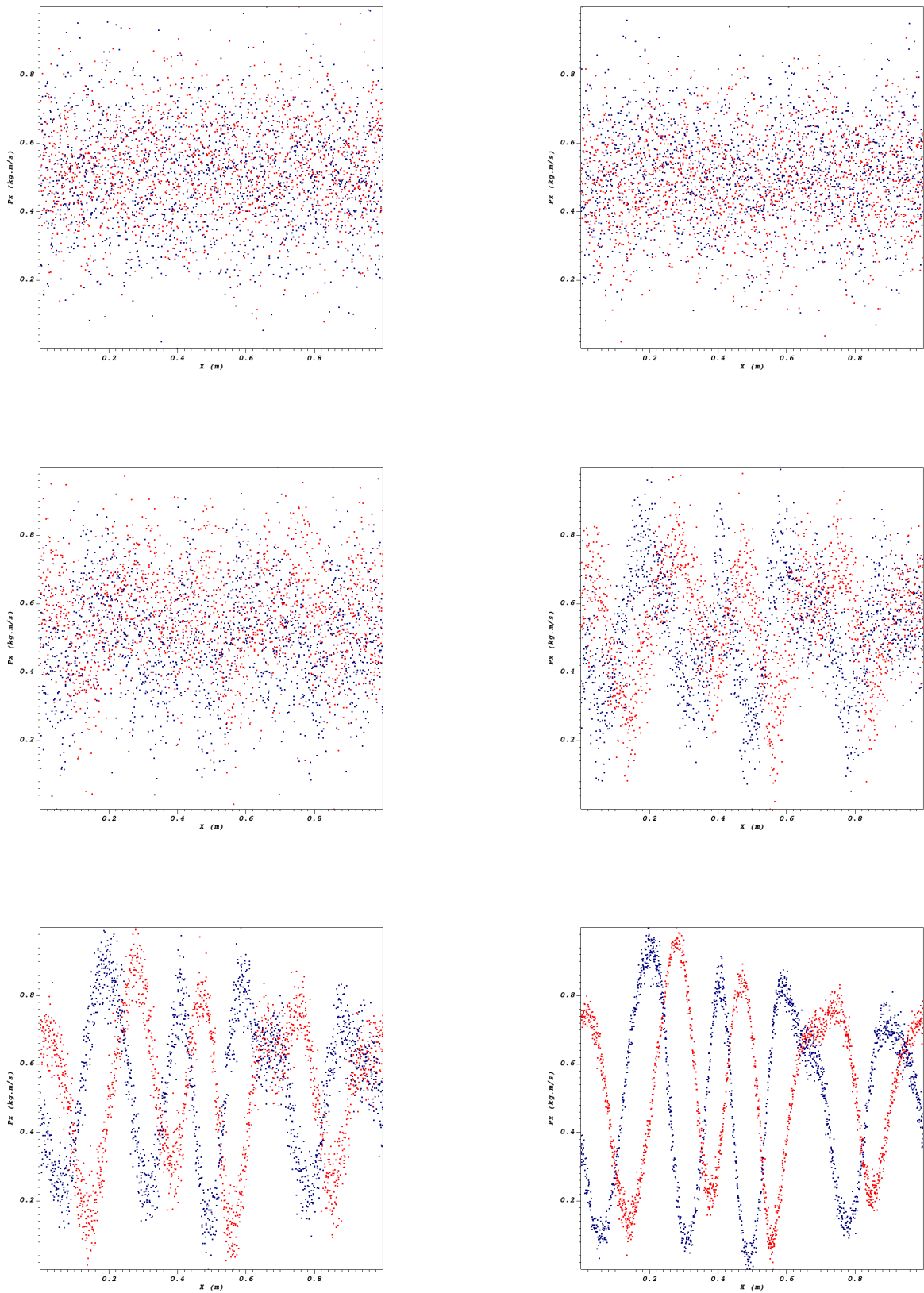


Figure 3.2: Particle in Cell simulation of the two stream instability effect - formation of the waves (phase space)

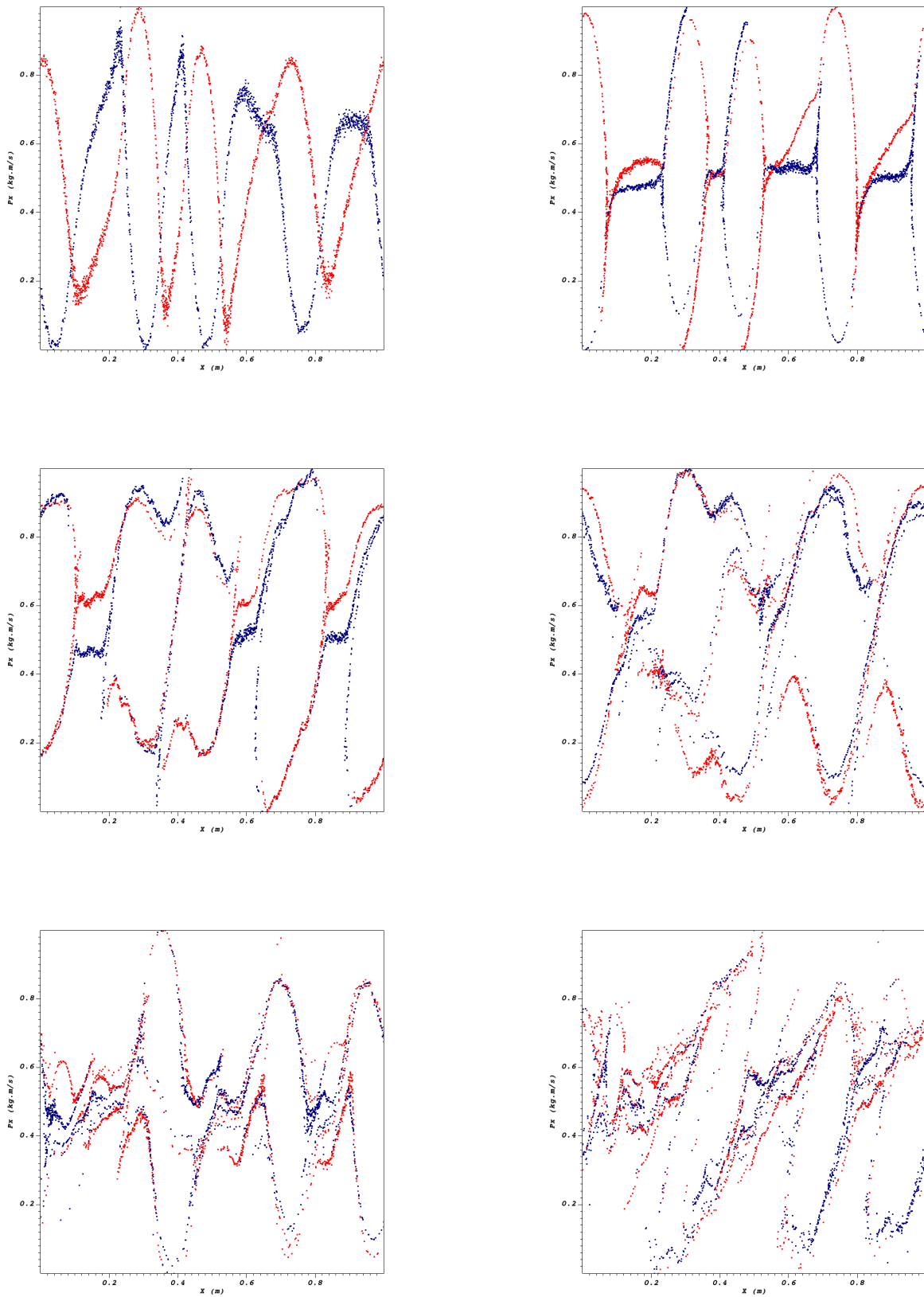


Figure 3.3: Particle in Cell simulation of the two stream instability effect - continuation (phase space)

For each stream we can write the cold fluid equations (continuity and dynamics) in the similar manner we did in the previous sections

$$-\omega n_{1,2} + N_{1,2} \mathbf{k} \cdot \mathbf{v}_{1,2} + n_{1,2} \mathbf{k} \cdot \mathbf{V}_{1,2} = 0 \quad (3.49a)$$

$$-\omega \mathbf{v}_{1,2} + \mathbf{v}_{1,2} (\mathbf{k} \cdot \mathbf{V}_{1,2}) = -i \frac{q_{1,2} \mathbf{E}}{m_{1,2}}, \quad (3.49b)$$

while the electric field is described by the Gauss law

$$i\mathbf{k} \cdot \mathbf{E} = 4\pi(n_1 q_1 + n_2 q_2). \quad (3.50)$$

In the last equation we assumed that the system was initially completely charge neutral. From equation (3.49b) the first order velocity can be immediately extracted

$$\mathbf{v}_{1,2} = i \frac{q_{1,2} \mathbf{E}}{m_{1,2}(\omega - \mathbf{k} \cdot \mathbf{V}_{1,2})}. \quad (3.51)$$

We can introduce this in equation (3.49a) to obtain also the density

$$n_{1,2} = i \frac{q_{1,2} N_{1,2} \mathbf{k} \cdot \mathbf{E}}{m_{1,2}(\omega - \mathbf{k} \cdot \mathbf{V}_{1,2})^2}. \quad (3.52)$$

This dependence showcases that the buncing phenomenon depends on the zero order velocity. Now, we substitute this in equation (3.50) to obtain

$$\mathbf{k} \cdot \mathbf{E} = 4\pi \mathbf{k} \cdot \mathbf{E} \left(\frac{q_1^2 N_1}{m_1(\omega - \mathbf{k} \cdot \mathbf{V}_1)^2} + \frac{q_2^2 N_2}{m_2(\omega - \mathbf{k} \cdot \mathbf{V}_2)^2} \right), \quad (3.53)$$

or, rather

$$\frac{q_1^2 N_1}{m_1(\omega - \mathbf{k} \cdot \mathbf{V}_1)^2} + \frac{q_2^2 N_2}{m_2(\omega - \mathbf{k} \cdot \mathbf{V}_2)^2} = \frac{1}{4\pi}. \quad (3.54)$$

This equation is harder to solve than one might guess from a first look. In order to get a feeling for how it behaves, I restrict the discussion to analyzing the particular case in which we have streams of equal strengths, *i.e.* that have the product of the total charge and the charge-to-mass ratio equal

$$N_1 \frac{q_1^2}{m_1} = N_2 \frac{q_2^2}{m_2} = \alpha. \quad (3.55)$$

An easy way to see why the terms in this equality characterize the strength of the beam is the following: suppose we look at how a beam's particles interact with themselves and we choose one while all the others are concentrated to one point. The acceleration that the lonely particle will get from the bunch of particles is proportional to $(N_1 - 1) \frac{q_1^2}{m_1} \approx N_1 \frac{q_1^2}{m_1}$ for large N_1 . We can say that this quantity reflects the maximum amount of acceleration that can be gained through self-interaction. Sure, since we also assumed the total system to be charge neutral, what we really equate is just the charge-to-mass ratio, but we should bear in mind that this is not a general occurrence, but rather a particular simplification in the case of just two beams. For more than two, the condition needs to be written similarly to equation (3.55).

We now get a biquadratic equation

$$\frac{1}{(\omega - \mathbf{k} \cdot \mathbf{V}_1)^2} + \frac{1}{(\omega - \mathbf{k} \cdot \mathbf{V}_2)^2} = \frac{1}{4\pi\alpha}. \quad (3.56)$$

The solution follows easily after some arithmetics

$$(\omega - \mathbf{k} \cdot \langle \mathbf{V} \rangle)^2 = \omega_{p0}^2 \left(\frac{1}{2} + x^2 \pm \frac{\sqrt{1+8x^2}}{2} \right), \quad (3.57)$$

where

$$\omega_{p0} = 4\pi\alpha \quad (3.58a)$$

$$\langle \mathbf{V} \rangle = \frac{\mathbf{V}_1 + \mathbf{V}_2}{2} \quad (3.58b)$$

$$x = \frac{\mathbf{k} \cdot (\mathbf{V}_1 - \mathbf{V}_2)}{2\omega_{p0}}. \quad (3.58c)$$

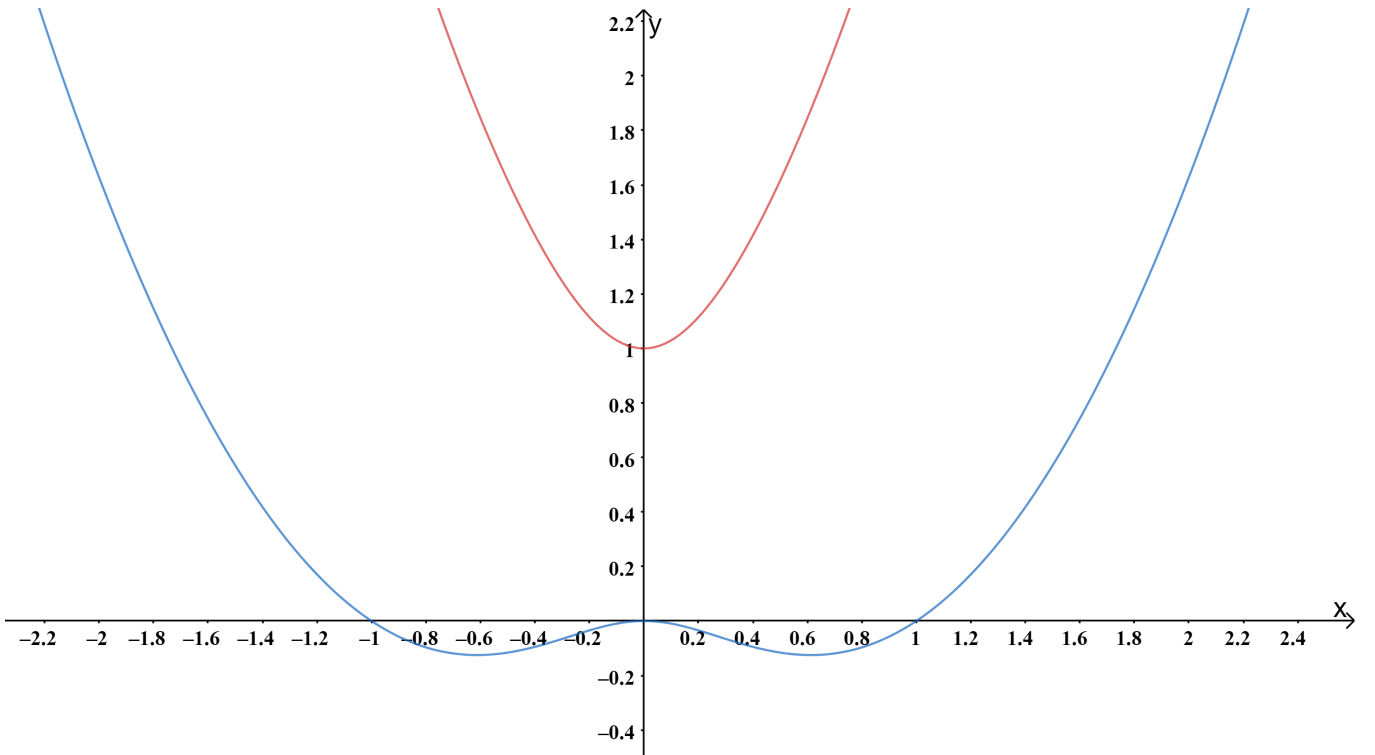


Figure 3.4: A plot of the quantity $\left(\frac{1}{2} + x^2 \pm \frac{\sqrt{1+8x^2}}{2} \right)$. With red is the expression with the plus sign, while with blue is the expression with the minus sign.

A quick look at figure 3.4 shows us that both solutions are stable for $|x| > 1$, that is for the case in which the zero order velocity of one stream is much larger than that of the other beam (on a scale of ω_{p0} , which is quite large for large N). The domain of interest in which the instability appears is $|x| > 1$. Here, the plus-sign solution gives the dispersion relation for longitudinal plasma waves. The minus-sign solution gives an unstable mode. In the simulation we see both these effect together. The instability evolves much slower than the longitudinal mode formation, so that is why in figures 3.2 and 3.3 we first see the formation of some plasma waves. But at some point the instability overtakes the oscillation and we see the formation of the characteristic cat-eye structures. An important thing to have in mind is that the growth rate of instability (which is derived from the imaginary part of the frequency in the minus-sign solution) is proportional to the wavelength.

3.8 Laser Wakefield Acceleration

While there have been many proposals for electron accelerators that use electromagnetic radiation, the most promising and reliable one is that by Tajima and Dawson 1979. The mechanism is the following (Mangles 2020): One shoots an intense laser pulse towards an underdense plasma. Since the ions are much heavier than the electrons, they will react much slower to the pulse. Thus, the drive pulse will push away electrons (mainly by the ponderomotive force), leaving behind the positively charged particles. At the same time, the positive charge accumulation will pull back the electrons. While returning, the electrons will overshoot, creating a plasma wave. Some electrons will be trapped in the wakefield of the pulse and will be pulled by it. A strong enough drive beam can expell all the electrons from the region in which the pulse is found. This situation corresponds to a so called blow-out regime. A bubble of just positive charges is formed and follows the laser. The high intensity laser will produce ionization in this bubble and thus electrons will be “injected” in it. This way the amount of accelerated electrons can be increased.

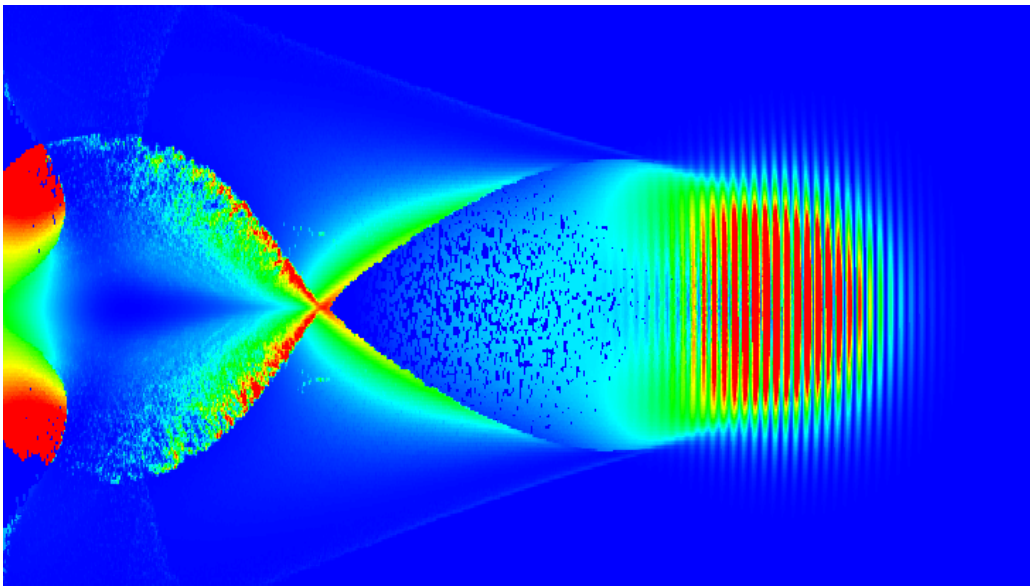


Figure 3.5: An illustrative picture of the laser wakefield acceleration effect obtained from a 3D particle in cell simulation showing the pseudocolor plot of the electron energy density inside the plasma. The laser pulse (modeled as a Gaussian pulse in this case) was traveling from left to right.

In figure 3.5 we can see to the right the profile of the laser beam since that region shows the electrons that are currently interacting with the pulse. We can also see quite clearly the formation of the plasma wave. The simulation was done with a low intensity laser, so we can see that the bubble regions are not completely empty in this case.

Classical particle accelerators can only transfer a certain amount of energy per meter. Because of this, in order to obtain high kinetic energies, their size must be very large. In a plasma based accelerator, the transfer of energy is much faster over small distances. Because of this they are of great interest especially for medical applications. Obviously, laser wake field acceleration is not perfect. It is limited by three effects: dephasing, pump depletion and diffraction. A concise and useful description of these limitations can be found in O’Neil 2017.

While, the mechanism is well understood, there is much work to be done in order to optimize it, mostly related to injection, the stability of the beam, and the understanding and exploitation of phenomena that arise at higher energies inside the plasma.

Chapter 4

Numerical Methods and Particle in Cell Simulations

The domain of numerical simulations for laser-plasma interaction is incredibly expansive, with many approaches one can choose from, like numerically solving the Vlasov equation or using Particle-in-cell methods, and many ways to implement and optimize them. I will focus in this thesis to the second option.

Even so, there are two key integration schemes that sit at the core of a Particle-in-cell software, the Maxwell solver and the particle pusher. In this chapter I aim to analyze in detail the most used schemes and their properties and eventually give a bird's eye view of the currently available PIC codes out there and the implementation choices they've made.

4.1 Numerical Methods

In this section I aim to summarize the basic theory in the area of numerical methods that would be required to understand the schemes that comprise PIC codes and the problems they pose. The presentation will be a short review of the concepts developed in the second chapter of the book by Leimkuhler and Reich 2004.

4.1.1 Introduction to Numerical Methods for Solving Differential Equations

We aim to understand how to find numerical solutions for a system of k ordinary differential equations with initial condition

$$\frac{d\mathbf{u}}{dt} = \mathbf{f}(\mathbf{u}), \quad \mathbf{u}(t_0) = \mathbf{u}_0 \in \mathbb{R}^k, \quad (4.1)$$

where t_0 is the initial time, \mathbf{u}_0 is the initial value of our solution and \mathbf{f} is a function that relates the elements in the solution vector. We can always set the time such that we have $t_0 = 0$ for simplicity.

We usually refer to the solution \mathbf{u} as a trajectory. If the solution can be determined by integration in time starting from an appropriate initial condition, the differential equation defines a one-parameter group of propagation maps $\phi_t : \mathbb{R}^k \rightarrow \mathbb{R}^k$. The group properties are given by the property that solving the problem from t_0 to t_1 and then from t_1 to t_2 is the same as solving from t_0 directly to t_2 . Thus, the composition of those maps inherits the properties of

the addition of real numbers. Note that this is just the *phase flow* of the equation in the way we defined it in section 3.6.

Solving equation (4.1) numerically means to discretize the time domain and find a scheme that would be able to propagate the trajectory within sizable error. Thus one obtains a set of values for the solution function at fixed points in time and those values can be eventually interpolated to estimate the values in between them. The simplest way to discretize the domain is to have a fixed small time Δt step such that $t_1 = t_0 + \Delta t$, $t_2 = t_1 + \Delta t$, and so on. More complex discretizations can be done if we know specific properties of the solution or if we are interested to increase the accuracy over some interval at the cost of decreasing it for another interval, but in what follows we will only deal with the simple equidistant discretization.

4.1.2 One-Step Methods

In general, one can choose to include at each iteration as many of the previously computed points on the trajectory. For example, if we want to use k previous points we have to find an appropriate scheme that computes \mathbf{u}_{n+1} in terms of $\mathbf{u}_{n-k+1}, \mathbf{u}_{n-k+2}, \dots, \mathbf{u}_n$ and the corresponding values of the derivative function $\mathbf{f}(\mathbf{u}_{n-k+1}), \mathbf{f}(\mathbf{u}_{n-k+2}), \dots, \mathbf{f}(\mathbf{u}_n)$. Here we denoted the point $\mathbf{u}(t_i)$ simply by \mathbf{u}_i . A linear multistep method of order k is, as the name suggests, a linear such recurrence relation. We are interested specifically in linear maps since they can be represented as matrices and under a matrix formalism they are trivial to implement in code.

This subsection is dedicated to one-step methods, that is for the case $k = 1$. We have as such to find an infinitesimal flow map that gives $\mathbf{u}_{i+1} = \phi_{\Delta t} \mathbf{u}_i$ for each i . Finding any point on the trajectory is then simply a matter of applying the infinitesimal map multiple times to the initial condition

$$\mathbf{u}_n = \phi_{\Delta t}^n \mathbf{u}_0 .$$

Here I denoted with $\phi_{\Delta t}^n$ the composition of $\phi_{\Delta t}$ with itself n times.

We have the following analytical equation between two consecutive points

$$\mathbf{u}_{i+1} - \mathbf{u}_i = \int_0^{\Delta t} d\tau \mathbf{f}(\mathbf{u}(t_i + \tau)) . \quad (4.2)$$

In order to find a one step-method we have to approximate the integral with a sum, which is done by using an appropriate quadrature rule

$$\mathbf{u}_{i+1} \approx \mathbf{u}_i + \sum_{j=1}^s b_j \mathbf{f}(\mathbf{u}(t_i + \tau_j)) \Delta t , \quad (4.3)$$

where b_j are the weights and τ_j are the quadrature points.

Here are some basic examples:

Explicit Euler Scheme

Obtained by setting $s = 1$, $b_1 = 1$, and $\tau_1 = 0$.

$$\mathbf{u}_{i+1} \approx \mathbf{u}_i + \mathbf{f}(\mathbf{u}_i) \Delta t + \mathcal{O}(\Delta t^2) . \quad (4.4)$$

Implicit Euler Scheme

Obtained by setting $s = 1$, $b_1 = 1$, and $\tau_1 = \Delta t$.

$$\mathbf{u}_{i+1} \approx \mathbf{u}_i + \mathbf{f}(\mathbf{u}_{i+1})\Delta t + \mathcal{O}(\Delta t^2). \quad (4.5)$$

Trapezoid Rule

Obtained by setting $s = 2$, $b_1 = b_2 = \frac{1}{2}$, and $\tau_1 = 0$, $\tau_2 = \Delta t$.

$$\mathbf{u}_{i+1} \approx \mathbf{u}_i + \frac{1}{2} [\mathbf{f}(\mathbf{u}_i) + \mathbf{f}(\mathbf{u}_{i+1})] \Delta t + \mathcal{O}(\Delta t^3). \quad (4.6)$$

Implicit Midpoint Rule

Obtained by setting $s = 1$, $b_1 = 1$, and $\tau_1 = \frac{\Delta t}{2}$, using $\mathbf{u}(t_i + \frac{\Delta t}{2}) \approx \frac{1}{2}(\mathbf{u}_i + \mathbf{u}_{i+1})$. Numerous more complex methods can be obtained by improving the latter approximation.

$$\mathbf{u}_{i+1} \approx \mathbf{u}_i + \mathbf{f}\left(\frac{\mathbf{u}_i + \mathbf{u}_{i+1}}{2}\right) \Delta t + \mathcal{O}(\Delta t^3). \quad (4.7)$$



It is important to note that while these methods are designed with first order ODE systems in mind, they can be often employed in higher order ODE systems. For example let us analyze the systems that can arise from Newton's second law

$$\frac{d^2\mathbf{r}}{dt^2} = \mathbf{F}(\mathbf{r}). \quad (4.8)$$

By defining $\mathbf{v} = \frac{d\mathbf{r}}{dt}$ we can transform it in the following system of first order equations

$$\frac{d\mathbf{v}}{dt} = \mathbf{F}(\mathbf{r}) \quad (4.9a)$$

$$\mathbf{v} = \frac{d\mathbf{r}}{dt}. \quad (4.9b)$$

This can be rewritten to look more like equation (4.1) through an inspired notation

$$\mathbf{u} = \begin{bmatrix} \mathbf{r} \\ \mathbf{v} \end{bmatrix} \quad (4.10a)$$

$$\mathbf{f}(\mathbf{u}) = \begin{bmatrix} \mathbf{v} \\ \mathbf{F}(\mathbf{r}) \end{bmatrix}. \quad (4.10b)$$

4.1.3 Error Estimation

One of the two main aspects that one needs to study when they propose to use a numerical scheme is accuracy. It basically refers to the error of the numerical solution compared to the real solution.

Error can arise when using the methods described so far from two mechanism: the difference between the approximation used and the Taylor expansion of the function (truncation error), and the accumulation of error caused by the discretization of the trajectory (round off error). The order of a method is defined by the power in the first Taylor coefficient neglected by

the scheme minus one. In the examples above, the Euler methods are of order 1, while the Trapezoid and Midpoint Rules have order 2. The order of the method shows the dependence of the global error with respect to the step-size of the discretization of the domain. So for an order 1 method, the error is linear in step-size, for an order 2, the error is quadratic polynomial in step-size, and so on.

Having all this in mind, developing a more accurate numerical scheme means to have the numerical solution just as close to the real solution for a larger time-step, or, conversely, having the numerical solution closer to the real solution for the same step-size.

4.1.4 Runge-Kutta Methods

The Runge-Kutta method is a generalization of the type of methods used before. As such, the schemes given as examples of one-step methods are actually particular cases of the more general Runge-Kutta method. The explicit Runge-Kutta for equation (4.1) in particular is the following

$$\mathbf{u}_{n+1} = \mathbf{u}_n + \Delta t \sum_{i=1}^s b_i \mathbf{f}(\mathbf{U}_i) \quad (4.11a)$$

$$\mathbf{U}_i = \mathbf{u}_n + \Delta t \sum_{j=1}^s a_{ij} \mathbf{f}(\mathbf{U}_j), \quad i = \overline{1, s} \quad (4.11b)$$

$$a_{i,j} = 0 \text{ for } j \geq i. \quad (4.11c)$$

This time around, each scheme is defined by a choice of s , b_i weights and the Runge-Kutta matrix a_{ij} . Note that in all our considerations so far related to equation (4.1) the function \mathbf{f} does not depend on time. This is because we are not interested in that possibility for the purpose of our PIC study. The Boris push propagates the particles over a small time interval while keeping the fields constant, then the Maxwell solver advances the fields in time taking into account the new particle positions. Nonetheless, for the sake of completion, I mention that including the time dependence would mean converting $\mathbf{f}(\mathbf{U}_j)$ in equation (4.11b) with $\mathbf{f}(t_n + c_i \Delta t, \mathbf{U}_j)$ and $c_1 = 0$. Thus, in order to have a scheme, now we would also need the set of c_i parameters which are commonly referred to as nodes. The list of all appropriate components for one scheme is presented in literature in Butcher tables. Since each scheme has its own unique table, the numerical properties (accuracy and stability can be computed using the tables. A more in depth explanation on how these tables work can be found in the book by Butcher 2008.

4.1.5 Leapfrog Algorithm

In specific situations we can apply the approximation methods discussed so far to separate parts of the solution. This is the mindset for creating partitioned Runge-Kutta methods. As an example, suppose our initial system of ODE (equation (4.1)) can be separated as such

$$\frac{d\mathbf{u}}{dt} = \mathbf{f}_1(\mathbf{u}, \mathbf{v}) \quad (4.12a)$$

$$\frac{d\mathbf{v}}{dt} = \mathbf{f}_2(\mathbf{u}, \mathbf{v}). \quad (4.12b)$$

To have a partitioned Runge-Kutta scheme we have to use two different regular Runge-Kutta schemes, one for each subset of equations, so to say

$$\mathbf{u}_{n+1} = \mathbf{u}_n + \Delta t \sum_{i=1}^s b_i^u \mathbf{f}_1(\mathbf{U}_i, \mathbf{V}_i) \quad (4.13a)$$

$$\mathbf{v}_{n+1} = \mathbf{v}_n + \Delta t \sum_{i=1}^s b_i^v \mathbf{f}_2(\mathbf{U}_i, \mathbf{V}_i) \quad (4.13b)$$

$$\mathbf{U}_i = \mathbf{u}_n + \Delta t \sum_{j=1}^s a_{ij}^u \mathbf{f}_1(\mathbf{U}_i, \mathbf{V}_i), \quad i = \overline{1, s} \quad (4.13c)$$

$$\mathbf{V}_i = \mathbf{v}_n + \Delta t \sum_{j=1}^s a_{ij}^v \mathbf{f}_2(\mathbf{U}_i, \mathbf{V}_i), \quad i = \overline{1, s}. \quad (4.13d)$$

In the perspective of the discussion at the end of section 4.1.2, we can see that this method is useful in solving equations of motion described by Newton's second law. In this context, the scheme in (4.13) is referred to as a Runge-Kutta-Nyström method.

In our endeavours, for equations of the form

$$\frac{d\mathbf{r}}{dt} = \mathbf{v} \quad (4.14a)$$

$$M \frac{d\mathbf{v}}{dt} = -\nabla_{\mathbf{r}} V(\mathbf{r}), \quad (4.14b)$$

we are interested in the Störmer-Verlet method

$$\mathbf{r}_{n+1} = \mathbf{r}_n + \Delta t \mathbf{v}_{n+\frac{1}{2}} \quad (4.15a)$$

$$M \mathbf{v}_{n+\frac{1}{2}} = M \mathbf{v}_n - \frac{\Delta t}{2} \nabla_{\mathbf{r}} V(\mathbf{r}_n) \quad (4.15b)$$

$$M \mathbf{v}_{n+1} = M \mathbf{v}_{n+\frac{1}{2}} - \frac{\Delta t}{2} \nabla_{\mathbf{r}} V(\mathbf{r}_{n+1}). \quad (4.15c)$$

A different scheme can be derived by playing around with the realations of this method. From equation (4.15a) we can extract the mid-step velocity as

$$\mathbf{v}_{n+\frac{1}{2}} = \frac{\mathbf{r}_{n+1} - \mathbf{r}_n}{\Delta t} \quad (4.16a)$$

$$\mathbf{v}_{n-\frac{1}{2}} = \frac{\mathbf{r}_n - \mathbf{r}_{n-1}}{\Delta t}, \quad (4.16b)$$

for two consecutive steps. By lowering equation (4.15c) with 1, we have

$$M \mathbf{v}_n = M \mathbf{v}_{n-\frac{1}{2}} - \frac{\Delta t}{2} \nabla_{\mathbf{r}} V(\mathbf{r}_n), \quad (4.17)$$

which replaced in equation (4.15b) gives a reccurence relation for the mid-step velocity

$$M \frac{\mathbf{v}_{n+\frac{1}{2}} - \mathbf{v}_{n-\frac{1}{2}}}{\Delta t} = -\nabla_{\mathbf{r}} V(\mathbf{r}_n). \quad (4.18)$$

We now insert in this equation (4.16) to finally obtain the leapfrog scheme

$$M \frac{\mathbf{r}_{n+1} - 2\mathbf{r}_n + \mathbf{r}_{n-1}}{\Delta t^2} = -\nabla_{\mathbf{r}} V(\mathbf{r}_n). \quad (4.19)$$

Since these two schemes are closely connected by equation (4.16), they have the same order. Since I haven't really given an example so far for how one can find the order of a numerical scheme, I will present in the following the proof for the fact that the leapfrog method is of second order.

Let us expand the position function in two ways around a fixed moment in time t

$$\mathbf{r}(t + \Delta t) = \mathbf{r}(t) + \frac{d\mathbf{r}(t)}{dt} \frac{\Delta t}{1!} + \frac{d^2\mathbf{r}(t)}{dt^2} \frac{\Delta t^2}{2!} + \frac{d^3\mathbf{r}(t)}{dt^3} \frac{\Delta t^3}{3!} + \mathcal{O}(\Delta t^4) \quad (4.20a)$$

$$\mathbf{r}(t - \Delta t) = \mathbf{r}(t) - \frac{d\mathbf{r}(t)}{dt} \frac{\Delta t}{1!} + \frac{d^2\mathbf{r}(t)}{dt^2} \frac{\Delta t^2}{2!} - \frac{d^3\mathbf{r}(t)}{dt^3} \frac{\Delta t^3}{3!} + \mathcal{O}(\Delta t^4). \quad (4.20b)$$

Adding these up we have

$$\mathbf{r}(t + \Delta t) + \mathbf{r}(t - \Delta t) = \mathbf{r}(t) + \frac{d^2\mathbf{r}(t)}{dt^2} \Delta t^2 + \mathcal{O}(\Delta t^4), \quad (4.21)$$

or, moving the derivative to the left and dividing by Δt^2

$$\frac{d^2\mathbf{r}(t)}{dt^2} = \frac{\mathbf{r}(t + \Delta t) - 2\mathbf{r}(t) + \mathbf{r}(t - \Delta t)}{\Delta t^2} + \mathcal{O}(\Delta t^2). \quad (4.22)$$

Note that we just recovered the second derivative approximation that generates the leapfrog scheme, so our proof is finished.

4.1.6 Stability

In order to understand the concept of stability, let us study the behaviour of some integration schemes in solving the most basic and the most important system of equations in physics – the linear harmonic oscillator

$$\frac{dx}{dt} = v \quad (4.23a)$$

$$\frac{dv}{dt} = -\omega^2 x. \quad (4.23b)$$

The figure below illustrates the phase space representation of the solutions obtained via five different numerical methods (with the frequency set to 1 for simplicity). The plots of the analytic solution is given as well for reference. The Julia code used for these small simulations can be found in the Appendix for the reader interested in seeing an example on how to use these methods in practice.

We can see a clear distinction in the solutions obtained. The trapezoid method and Störmer-Verlet method are very close to the real circular solution. On the opposite spectrum, the implicit and explicit Euler methods show a clearly undesired behaviour, much different from the others. The semi-implicit Euler method does a decent job, but the shape is a bit oblate. Even so, this scheme has a useful property, namely it is volume preserving. This means that the volume in phase space of the solution obtained is constant over an arbitrarily large number of periods. In contrast, the phase space volume of the implicit and explicit Euler integrators isn't even well

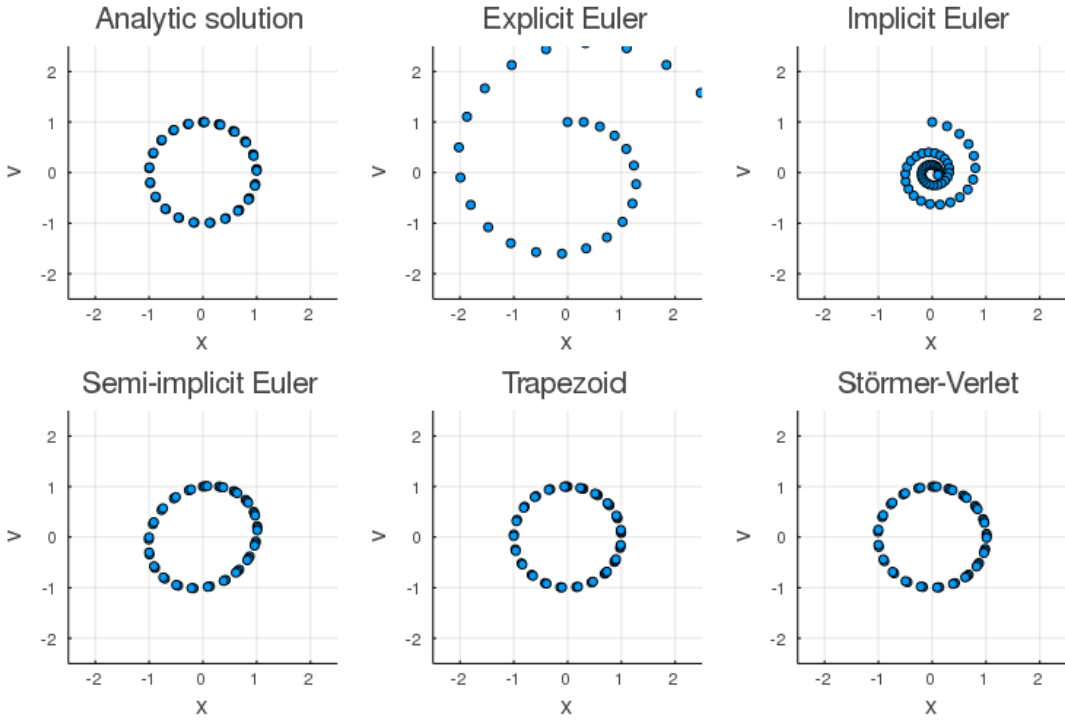


Figure 4.1: Phase space plots of the solution for the harmonic oscillator equations using different numerical methods. The angular frequency is $\omega = 1$, the total time of the simulation is 15 and the time-step is 0.3.

defined because the solution diverges too fast. The difference though does not lay in volume preservence, but in what we call *asimptotic stability*. The best way to study this property is mathematically. While a picture like that in figure 4.1 gives a good visual hint to what asimptotic stability of a scheme is, it was especially exaggerated by choosing a large time-step. If one reruns those simulations with a time step of 0.01 instead of 0.3, almost all plots will start looking like a circle. That doesn't mean that we fixed our methods, but rather that by increasing the accuracy we made the imperfections manifest over a much larger time scale. Indeed, if we increase the total duration of the simulation enough, we would see that thing are still bad for the first two Euler methods. This is shown in figure 4.2.

So how can we study this asimptotic stability? Let us rewrite the linear harmonic oscillator equation (4.23) in matrix form

$$\frac{d}{dt} \begin{bmatrix} x \\ v \end{bmatrix} = \begin{bmatrix} 0 & 1 \\ -\omega^2 & 0 \end{bmatrix} \begin{bmatrix} x \\ v \end{bmatrix}. \quad (4.24)$$

We can actually do better than this and find a flow chart, since we know the most general analytic solution for our problem

$$x = A \sin(\omega t) + B \cos(\omega t) \quad (4.25a)$$

$$v = \omega A \cos(\omega t) - \omega B \sin(\omega t). \quad (4.25b)$$

At time $t = 0$ these equations become simply $x_0 = B$ and $v_0 = \omega A$. So, using the initial

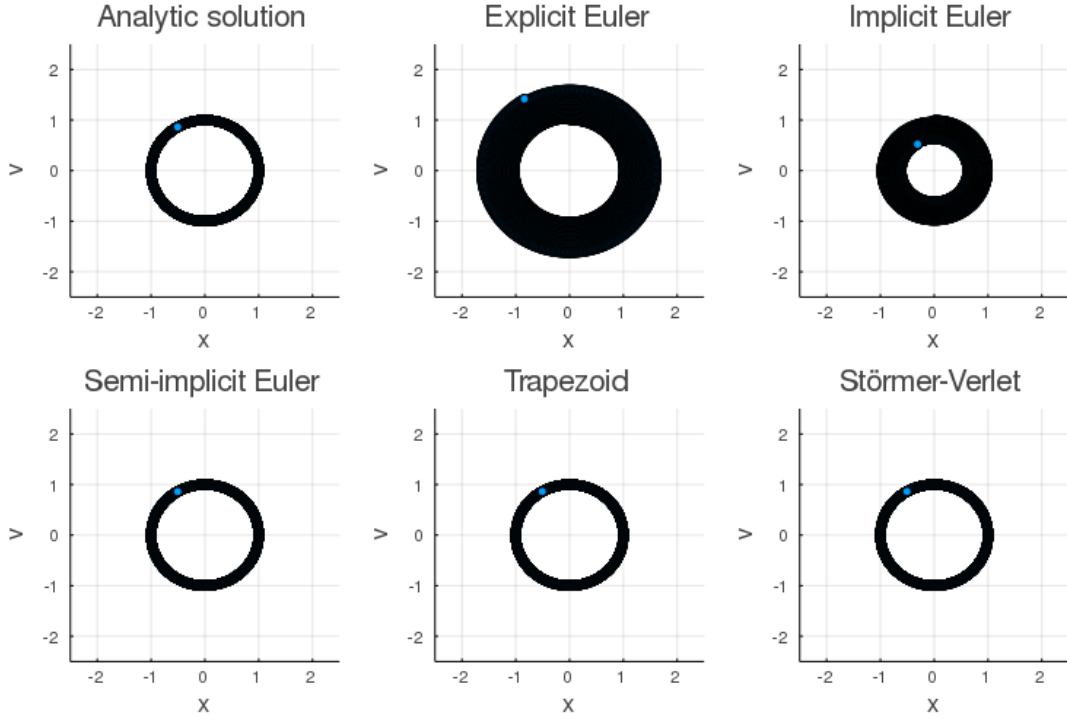


Figure 4.2: Phase space plots of the solution for the harmonic oscillator equations using different numerical methods. The angular frequency is $\omega = 1$, but this time around the total time of the simulation is 100 and the time-step is 0.01.

conditions we now have

$$x = x_0 \cos(\omega t) + v_0 \frac{1}{\omega} \sin(\omega t) \quad (4.26a)$$

$$v = -x_0 \omega \sin(\omega t) + v_0 \cos(\omega t), \quad (4.26b)$$

or, in matrix form

$$\begin{bmatrix} x \\ v \end{bmatrix} = \begin{bmatrix} \cos(\omega t) & \frac{1}{\omega} \sin(\omega t) \\ -\omega \sin(\omega t) & \cos(\omega t) \end{bmatrix} \begin{bmatrix} x_0 \\ v_0 \end{bmatrix} \quad (4.27a)$$

$$\phi_t = \begin{bmatrix} \cos(\omega t) & \frac{1}{\omega} \sin(\omega t) \\ -\omega \sin(\omega t) & \cos(\omega t) \end{bmatrix}, \quad (4.27b)$$

where we denoted by ϕ_t the analytical flow map. There is a new way to see numerical methods now. Coming up with a new scheme is equivalent to finding a different approximation for the infinitesimal version of this map. But before we delve into this topic, let us find the eigenvalues of ϕ_t . The computation is quite straightforward

$$\lambda \begin{bmatrix} x_0 \\ v_0 \end{bmatrix} = \begin{bmatrix} \cos(\omega t) & \frac{1}{\omega} \sin(\omega t) \\ -\omega \sin(\omega t) & \cos(\omega t) \end{bmatrix} \begin{bmatrix} x_0 \\ v_0 \end{bmatrix}$$

$$v_0(\lambda - \cos(\omega t)) = -x_0 \omega \sin(\omega t)$$

$$v_0 \frac{1}{\omega} \sin(\omega t) = x_0(\lambda - \cos(\omega t)).$$

Dividing these last two equations gives

$$\begin{aligned} (\lambda - \cos(\omega t))^2 &= -\sin^2(\omega t) \\ \Rightarrow \lambda^2 - 2\lambda \cos(\omega t) + 1 &= 0, \end{aligned}$$

which gives the solution

$$\lambda_{1,2} = e^{\pm i\omega t}. \quad (4.28)$$

Now let us look at the methods. The explicit Euler method has the following infinitesimal flow map and its eigenvalues

$$\phi_{\Delta t}^{Euler} = \begin{bmatrix} 1 & \Delta t \\ -\omega^2 \Delta t & 1 \end{bmatrix} \quad (4.29a)$$

$$\lambda_{1,2}^{Euler} = 1 \pm i\omega\Delta t, \quad (4.29b)$$

which is obviously just a first order approximation of ϕ_t and its eigenvalues. Now we can give the definition of stability and see why this scheme is not stable for our problem.

Definition 1. A numerical method is stable if the solution it gives for a linear problem has an asymptotically bounded growth.

This basically assures that the error does not blow up. While this is an intuitive definition, there is a better way to go about things mathematically. Without going into details about forward and backward stability, we can mention the concept of mixed stability. The idea is the following: looking at equation (4.1) let us take \mathbf{f} be the analytic propagation function and $\tilde{\mathbf{f}}$ the one given by the scheme, while \mathbf{z} and $\tilde{\mathbf{z}}$ are the analytic and numeric solution, respectively, at the same point in time. The method has mixed stability if the quantity $\frac{\|\tilde{\mathbf{f}}(\mathbf{z}) - \mathbf{f}(\tilde{\mathbf{z}})\|}{\|\mathbf{f}(\tilde{\mathbf{z}})\|}$ is within machine error for an $\tilde{\mathbf{z}}$ with relative error within machine error.

For the interested reader, a list of relevant mathematical definitions related to stability can be found in the presentation by E. Liu 2020. However, we will restrict ourselves to an important and powerful result. The growth of the error after applying the infinitesimal flow map n is proportional to the n^{th} power of the corresponding eigenvalues. In this context we can formulate the following theorem.

Theorem 1. A sufficient condition for a method to have asymptotic stability is to have the eigenvalues of its matrix laying in the closed unit disc (unit circle included) in the complex plane, and, if any eigenvalue lies on the unit circle it must be simple (not repeated).

A quick look at $\lambda_{1,2}^{Euler}$ reveals that their modulus is larger than 1. Because of this, the growth of the error in the explicit Euler method is exponential. In fact, in this case, there is no time-step we can choose to make it stable. A point has to be made though: instability does not deny convergence. As discussed in the beginning of the section, depending on how small of a time-step we choose for a specific simulation duration we can make the instability effects negligible for a long simulation time. But this will always come at the cost of requiring more computational power. Stable algorithms are useful in the sense that we can reduce the strain on our computer without obtaining diverging errors.

As we saw in the beginning of this section, there are other methods that are stable for the linear harmonic oscillator problem. However, an unconditionally stable scheme is hard to come

about. Most of the time we can find a certain condition for our method to be stable. As an example, let us look at the Störmer-Verlet method.

In the context of equation (4.23), equations (4.15a) to (4.15c) become

$$x_{n+1} = x_n + v_{n+\frac{1}{2}} \Delta t \quad (4.30a)$$

$$v_{n+\frac{1}{2}} = v_n - x_n \frac{\omega^2 \Delta t}{2} \quad (4.30b)$$

$$v_{n+1} = v_{n+\frac{1}{2}} - x_{n+1} \frac{\omega^2 \Delta t}{2}, \quad (4.30c)$$

or

$$x_{n+1} = x_n \left(1 - \frac{\omega^2 \Delta t^2}{2} \right) + v_n \Delta t \quad (4.31a)$$

$$v_{n+1} = -x_n \left(1 - \frac{\omega^2 \Delta t^2}{4} \right) \omega^2 \Delta t + v_n \left(1 - \frac{\omega^2 \Delta t^2}{2} \right), \quad (4.31b)$$

which gives the infinitesimal flow map

$$\phi_{\Delta t}^{SV} = \begin{bmatrix} 1 - \frac{\omega^2 \Delta t^2}{2} & \Delta t \\ -\left(1 - \frac{\omega^2 \Delta t^2}{4}\right) \omega^2 \Delta t & 1 - \frac{\omega^2 \Delta t^2}{2} \end{bmatrix}. \quad (4.32)$$

In order to make solving for eigenvalues easier let us employ the notation $\eta = \frac{\omega^2 \Delta t^2}{2}$. Then, we have

$$\lambda x_0 = x_0(1 - \eta) + v_0 \Delta t \quad (4.33a)$$

$$\lambda v_0 = -2 \frac{x_0}{\Delta t} \eta \left(1 - \frac{\eta}{2}\right) + v_0(1 - \eta), \quad (4.33b)$$

followed by

$$x_0(\lambda + \eta - 1) = v_0 \Delta t \quad (4.34a)$$

$$2x_0 \eta \left(1 - \frac{\eta}{2}\right) = -(\lambda + \eta - 1)v_0 \Delta t. \quad (4.34b)$$

Dividing these leads to the final equation for the eigenvalues

$$\lambda^2 - 2(1 - \eta)\lambda + 1 = 0. \quad (4.35)$$

The discriminant of this equation is $4\eta(\eta - 2)$ and, consequently, the eigenvalues are

$$\lambda_{1,2} = 1 - \eta \pm \sqrt{\eta(\eta - 2)}. \quad (4.36)$$

Note that their product is 1. We are now interested in the modulus of these. For $\eta > 2$ the solutions are real and the modulus of one of them is easily found to be greater than unity. Indeed, if $\eta = 2 + \alpha$, $\alpha > 1$

$$|\lambda_{1,2}| = \left| 1 - \eta \pm \sqrt{\eta(\eta - 2)} \right| = \left| -1 - (\alpha \mp \sqrt{\alpha^2 + 2\alpha}) \right| > 1, \quad (4.37)$$

since $\alpha + \sqrt{\alpha^2 + 2\alpha} > 0$. If $\eta < 2$ the eigenvalues are complex and are conjugates of each other, such that their modulus is 1. Thus, we conclude that the method is stable for $\eta < 2$, which translates to

$$\Delta t < \frac{2}{\omega} = \frac{T}{\pi}. \quad (4.38)$$

4.2 The Relevant Equations

Particle-in-cell codes are nowadays the most popular tool for simulating plasma systems. One of the best references for what they are, how they work and how reliable the results that can be obtained are is the book by Birdsall and Langdon 1995, which describes the main numerical methods used and some of their properties. However, Particle-in-cell codes have evolved greatly in the last two decades and new techniques and optimizations have been produced and even put in practice. Even so, with the exception of quasistatic codes, they are still involved in solving the same physical equations. As such, it is useful for anyone interested in working with such software to know and understand the principles behind.

In general, PIC codes have four main components:

1. A Maxwell solver which propagates the Maxwell equations (which are relativistically invariant by themselves) in time and space on the grid

$$\nabla \cdot \mathbf{E} = \frac{\rho}{\epsilon_0} \quad (4.39a)$$

$$\nabla \cdot \mathbf{B} = 0 \quad (4.39b)$$

$$\nabla \times \mathbf{E} = -\frac{\partial \mathbf{B}}{\partial t} \quad (4.39c)$$

$$\nabla \times \mathbf{B} = \mu_0 \mathbf{j} + \frac{1}{c^2} \frac{\partial \mathbf{E}}{\partial t}; \quad (4.39d)$$

2. A field gatherer that interpolates the electromagnetic field at the particle positions on the grid;
3. A particle pusher that advances the positions and velocities of each particle under the action of the Lorentz force (which we will write in its relativistic form)

$$\frac{d\mathbf{p}_\alpha}{dt} = q_\alpha \left(\mathbf{E} + \frac{\mathbf{p}_\alpha}{m_\alpha \gamma_\alpha} \times \mathbf{B} \right) \quad (4.40a)$$

$$\gamma_\alpha = \sqrt{1 + \left(\frac{\mathbf{p}_\alpha}{m_\alpha c} \right)^2}, \quad (4.40b)$$

where α indexes each particle;

4. A current and charge depositor which computes the current and charge densities on the grid by interpolating the particle distributions.

The main appeal of this approach is its self-consistency. That is, the total fields used are both those that are part of the electromagnetic waves that are introduced in the system (in general laser beams) and those generated by the charged particles that compose the plasma. As such we also include the long range Coulombian interaction between particles. The short

range interaction, namely collisions between particles, is by default neglected since we usually simulate rarefied plasmas, but many codes now come with additional routines that include these processes. Additional routines are now developed with the advent of the high intensity laser technologies because at the corresponding energies reached by the particles quantum electrodynamical effects become relevant. Although there are quite a few PIC codes that include QED routines, there is still a long way until these algorithms reach the efficiency and stability that of those four main ones described above. As such, the implementation of QED effects in numerical plasma simulations is currently a hot research topic.

It is mandatory to mention that while the four steps above outline a microscopic model, PIC simulations are not completely microscopic due to technological limitations regarding computing power. Instead of working with one virtual particle for one real particle, it is customary to use macro-particles. A macro-particle represents many particles of the same species (from 10^6 to 10^{11} depending on the properties of our plasma) moving collectively. These particles are obviously not localized at a single point, but rather they have a shape function attached to them to make the derivation of currents and charge densities more consistent. For a long time the use of macro-particles was not supported by argument and was a source of criticism towards PIC methods. The defense was built only on the excuse that the simulations give very accurate statistical results. Things are different nowadays. We can now explain (quite easily in fact) that the macro-particles themselves can be interpreted as a statistical ensemble of real particles. The secret lies in the Vlasov equation.

4.2.1 The Connection with the Vlasov Equation

Let us revisit the Vlasov equation, which we derived in section 3.6

$$\frac{\partial \rho}{\partial t} + \mathbf{f} \cdot \frac{\partial \rho}{\partial \mathbf{p}} + \mathbf{v} \cdot \frac{\partial \rho}{\partial \mathbf{r}} = 0, \quad (4.41)$$

where ρ was the distribution function that describes the entire system of particles, $\mathbf{p} = (\mathbf{p}_1, \mathbf{p}_2, \dots)$ and $\mathbf{v} = (\mathbf{v}_1, \mathbf{v}_2, \dots)$, $\mathbf{r} = (\mathbf{r}_1, \mathbf{r}_2, \dots)$ the momenta, the velocities, and the positions of the particles, and $\mathbf{f} = (\mathbf{f}_1, \mathbf{f}_2, \dots)$ the forces acting on each particle.

The main argument in the following discussion is a relativistic upgrade of the one in C. S. Liu, Tripathi, and Eliasson 2020. For consistency with the equations we outlined for the PIC method, I rewrite this equation in its relativistic form and considering all forces to be of the Lorentz type

$$\frac{\partial \rho}{\partial t} + \sum_{\alpha} \left[q_{\alpha} \left(\mathbf{E}_{\alpha} + \frac{\mathbf{p}_{\alpha}}{m_{\alpha} \gamma_{\alpha}} \times \mathbf{B}_{\alpha} \right) \frac{\partial \rho}{\partial \mathbf{p}_{\alpha}} + \frac{\mathbf{p}_{\alpha}}{m_{\alpha} \gamma_{\alpha}} \frac{\partial \rho}{\partial \mathbf{r}_{\alpha}} \right] = 0, \quad (4.42)$$

where α indexes all the particles in the system and the fields E_{α} and B_{α} are to be computed at the position of particle α .

The key insight now is: imposing that the particles move under the Newton-Lorentz equation (4.40a) implies having a stationary solution for the distribution function. That is, the equations

$$\frac{d\mathbf{p}_{\alpha}}{dt} = q_{\alpha} \left(\mathbf{E} + \frac{\mathbf{p}_{\alpha}}{m_{\alpha} \gamma_{\alpha}} \times \mathbf{B} \right) \quad (4.43a)$$

$$\frac{d\mathbf{r}_{\alpha}}{dt} = \frac{\mathbf{p}_{\alpha}}{m_{\alpha} \gamma_{\alpha}}, \quad (4.43b)$$

reduce the Vlasov equation as follows

$$\frac{\partial \rho}{\partial t} + \sum_{\alpha} \left(\frac{\partial \rho}{\partial \mathbf{p}_{\alpha}} \frac{d\mathbf{p}_{\alpha}}{dt} + \frac{\partial \rho}{\partial \mathbf{r}_{\alpha}} \frac{d\mathbf{r}_{\alpha}}{dt} \right) = \frac{d\rho}{dt} = 0. \quad (4.44)$$

Of course this is not an equivalency. While equation (4.43) implies that the distribution function of the entire system is stationary, the reverse is not true, unless we do a rough approximation and suppose that the total distribution can be separated in a sum of independent single particle distribution functions. By employing this latter approximation we would unavoidably neglect some intrinsic interactions that take place in our system. Nonetheless, this problem does not affect the validity of our Particle-in-cell method. The thing is that while equation (4.43) doesn't describe all the complete stationary solution of the Vlasov equation, it still describes at least one particular stationary solution. Working with superparticles is like studying the evolution of an ensemble of these solutions. Thus, by including a relevant (yet not large enough to give unreasonable simulation times) number of superparticles we obtain a statistically realistic solution. Some even call PIC a Monte-Carlo method because of this.

The reverse approach is used in numerical studies of plasma physics using Vlasov codes (VC). These approaches simply try to solve the Vlasov equation as it is in order to obtain exact solutions (exact up to numerical errors). If one has the total distribution function, then every statistical piece of information about the system is known. Some basics about how this can be achieved and computational optimization can be found in Silin 2020. However, directly solving for such a big solution with a number of variables proportional to the real number of particles in the system takes a lot of time if we try to simulate realistically sized systems.

An approach based on the splitting of the distribution function is not completely flawed. One can try to get closer to reality by using a better approximation by expanding the total distribution in a series that contains single-particle terms, two-particle terms, and so on. While it is true that this improves the solutions greatly, the cost in computation time is equally great and much refinement would have to be done.

The presentation so far should not give the reader the impression that PIC is the superior approach. In fact, numerical heating is a common problem of PIC codes and the stability conditions for the simulations are quite restrictive, which together with the computational limitations reduce the amount of experiments you can run. An easy to follow rough sketch of the trade off between PIC and VC and a discussion on when is one better than the other is found in Bertrand *et al.* 2005.

4.3 Methods used in Particle-in-cell simulations

4.3.1 The Boris Push

It is time now to tackle the first method in the context of Particle-in-cell simulations. It is discussed in Birdsall and Langdon 1995, there are different ways to implement particles pushers, either by partially separating the action of the electric and magnetic fields (Buneman 1967), or by separating them completely (Boris 1970). Along the years, even more alternatives have surfaced. A nice up-to-date review of the currently relevant relativistic schemes for particle dynamics in electromagnetic fields is Ripperda *et al.* 2018. In this section we will present and analyze the Boris push, since it is widely implemented in the currently available PIC codes. The popularity of this specific scheme stems from its practical performance. Since its initial proposal, the Boris push was observed to have good accuracy over long integration times in simulations. The explanation for why it works so well was given only recently in Qin *et al.*

2013. They studied only the properties of the non-relativistic scheme. Because of this, we will also start with the classical case, which is simpler, in order to gain some intuition.

Classical Boris Push

We aim to solve the following equations

$$\frac{d\mathbf{r}}{dt} = \mathbf{v} \quad (4.45a)$$

$$\frac{d\mathbf{v}}{dt} = \frac{q}{m} (\mathbf{E} + \mathbf{v} \times \mathbf{B}) . \quad (4.45b)$$

We will employ the Störmer-Verlet method

$$\mathbf{r}_{n+1} = \mathbf{r}_n + \mathbf{v}_{n+\frac{1}{2}} \Delta t \quad (4.46a)$$

$$\mathbf{v}_{n+\frac{1}{2}} = \mathbf{v}_n + \frac{q}{m} \frac{\Delta t}{2} [\mathbf{E} + \mathbf{v} \times \mathbf{B}]_{\mathbf{r}=\mathbf{r}_n} \quad (4.46b)$$

$$\mathbf{v}_n = \mathbf{v}_{n+\frac{1}{2}} + \frac{q}{m} \frac{\Delta t}{2} [\mathbf{E} + \mathbf{v} \times \mathbf{B}]_{\mathbf{r}=\mathbf{r}_{n+1}} . \quad (4.46c)$$

In order to find a good evaluation for the quantities enclosed in square brackets we need to play around a bit with these equations. By lowering the third one by one step and replacing it in the second one we get

$$\frac{\mathbf{v}_{n+\frac{1}{2}} - \mathbf{v}_{n-\frac{1}{2}}}{\Delta t} = \frac{q}{m} [\mathbf{E} + \mathbf{v} \times \mathbf{B}]_{\mathbf{r}=\mathbf{r}_n} . \quad (4.47)$$

Let us now take equation (4.46a) at two consecutive steps

$$\mathbf{r}_n = \mathbf{r}_{n-1} + \mathbf{v}_{n-\frac{1}{2}} \Delta t \quad (4.48a)$$

$$\mathbf{r}_{n+1} = \mathbf{r}_n + \mathbf{v}_{n+\frac{1}{2}} \Delta t \quad (4.48b)$$

and add them to obtain

$$\frac{\mathbf{r}_{n+1} - \mathbf{r}_{n-1}}{\Delta} = \frac{\mathbf{v}_{n+\frac{1}{2}} + \mathbf{v}_{n-\frac{1}{2}}}{2} , \quad (4.49)$$

which is what we will use as an approximation for the velocity at $\mathbf{r} = \mathbf{r}_n$. We finally reach the following scheme

$$\frac{\mathbf{r}_{n+1} - \mathbf{r}_n}{\Delta t} = \mathbf{v}_{n+\frac{1}{2}} \quad (4.50a)$$

$$\frac{\mathbf{v}_{n+\frac{1}{2}} - \mathbf{v}_{n-\frac{1}{2}}}{\Delta t} = \frac{q}{m} \left(\mathbf{E}_n + \frac{\mathbf{v}_{n+\frac{1}{2}} + \mathbf{v}_{n-\frac{1}{2}}}{2} \times \mathbf{B}_n \right) . \quad (4.50b)$$

This is the Boris push, but it is not yet the final algorithm. In order to be able to implement this scheme in an actual code, we need a way to separate $\mathbf{v}_{n+\frac{1}{2}}$ and $\mathbf{v}_{n-\frac{1}{2}}$ from the second equation. There are many equivalent ways to do so, but Boris originally came up with a method to separate the action of the electric and magnetic fields by employing the following three equations

$$\mathbf{v}^- = \mathbf{v}_{n-\frac{1}{2}} + \frac{q}{m} \mathbf{E}_n \frac{\Delta t}{2} \quad (4.51a)$$

$$\frac{\mathbf{v}^+ - \mathbf{v}^-}{\Delta t} = \frac{q}{m} \frac{\mathbf{v}^+ + \mathbf{v}^-}{2} \times \mathbf{B}_n \quad (4.51b)$$

$$\mathbf{v}_{n+\frac{1}{2}} = \mathbf{v}^+ + \frac{q}{m} \mathbf{E}_n \frac{\Delta t}{2}, \quad (4.51c)$$

where the second step is to be rewritten in the following way:

$$\mathbf{v}^+ = \mathbf{v}^- + (\mathbf{v}^- + \mathbf{v}^- \times \mathbf{t}) \times \mathbf{s} \quad (4.52a)$$

$$\mathbf{t} = \frac{q}{2m} \mathbf{B}_n \Delta t \quad (4.52b)$$

$$\mathbf{s} = \frac{2}{1 + t^2} \mathbf{t}. \quad (4.52c)$$

The full classical Boris push code recipe is described by equations (4.50a), (4.51a), (4.51c) and (4.52) put together. Note that we basically work only with mid-step velocities. But we can always recover the actual velocities from equation (4.46b) like this

$$\mathbf{v}_n = \mathbf{v}_{n+\frac{1}{2}} - \frac{q}{m} \frac{\Delta t}{2} \left(\mathbf{E}_n + \frac{\mathbf{v}_{n+\frac{1}{2}} + \mathbf{v}_{n-\frac{1}{2}}}{2} \times \mathbf{B}_n \right). \quad (4.53)$$

Such an equation is useful in order to get the initial conditions for the mid-step velocities from the initial conditions given for the velocity.

We introduced equations (4.51) and (4.52) out of nowhere, but it is quite straightforward to see that by eliminating v^- and v^+ we simply recover equation (4.50b). This is just a convenient way to write for a machine to understand, but is simply a reorganization of the equation (4.50b). It does not influence numerical properties. That is, all the numerical properties of the algorithm lie in equation (4.50). There is a geometrical interpretation to the break up described by equation (4.51). v^- and v^+ give the drift motion due to electric field, equation (4.51) described a rotation under the effect of a constant magnetic field. For a more in depth description with images to help visualization I recommend the Master Thesis of Micluță-Câmpleanu 2019.

Relativistic Boris Push

The relativistic version should discretize equation (4.40a) in the same way we presented so far. If we make the notation $\mathbf{u} = \gamma \mathbf{v}$, the equations of the algorithm are now simply

$$\frac{\mathbf{r}_{n+1} - \mathbf{r}_n}{\Delta t} = \frac{\mathbf{u}_{n+\frac{1}{2}}}{\gamma_{n+\frac{1}{2}}}, \quad \gamma_{n+\frac{1}{2}} = \sqrt{1 + \left(\frac{u_{n+\frac{1}{2}}}{c} \right)^2} \quad (4.54a)$$

$$\mathbf{u}^- = \mathbf{u}_{n-\frac{1}{2}} + \frac{q}{m} \mathbf{E}_n \frac{\Delta t}{2} \quad (4.54b)$$

$$\mathbf{u}^+ = \mathbf{u}^- + (\mathbf{u}^- + \mathbf{u}^- \times \mathbf{t}) \times \mathbf{s}, \quad \mathbf{t} = \frac{q}{2m\gamma_n} \mathbf{B}_n \Delta t, \quad \mathbf{s} = \frac{2}{1 + t^2} \mathbf{t} \quad (4.54c)$$

$$\gamma_n = \sqrt{1 + \left(\frac{\mathbf{u}^-}{c} \right)^2} = \sqrt{1 + \left(\frac{\mathbf{u}^+}{c} \right)^2} \quad (4.54d)$$

$$\mathbf{u}_{n+\frac{1}{2}} = \mathbf{u}^+ + \frac{q}{m} \mathbf{E}_n \frac{\Delta t}{2}. \quad (4.54e)$$

4.3.2 Symplecticity and Volume Conservation Theory

In terms of accuracy, the Boris push remains at its core a twist on the Störmer-Verlet method, so it can be easily shown that it is a second order scheme. But there are things that are not inherited this way. We already saw that the Störmer-Verlet and leapfrog integrators are very similar. It is a known fact that the leapfrog scheme is one of the simplest symplectic methods and as such it has outstanding conservation properties. But we can not expect the Boris push to be the same. The thing that throws everything off is the dependence on velocity that we have introduced in the expression of the force. Even so, the Boris push still has a strength in that it is volume preserving. It is also important to mention that it conserves energy exactly in the absence of the electric field. This may not seem that great in itself, since the electric field is never vanishing in practical simulations, but it was a hint towards the idea that it might be volume preserving. In what follows we will delve a bit into the concept of symplecticity and see how we can find out if a scheme has this property. Of course, our example for this theory will be the Boris push algorithm.

In order to give a concrete mathematical definition for symplecticity we have to define a handy tool first, as presented on p. 164 in Arnold 1997.

Definition 2. Let M^{2n} , $n \in \mathbb{N}$, be a differentiable manifold with an even number of dimensions (this is general, so we can use any such manifold, but for our numerical methods related endeavours we really only need to talk about \mathbb{R}^{2n}). **An exterior form of degree two** (or a **2-form**) on this manifold is a map $\omega_2 : M^n \times M^n \rightarrow M$ that is bilinear and skew symmetric:

$$\begin{aligned}\omega_2(\lambda_1 \xi_1 + \lambda_2 \xi_2, \xi_3) &= \lambda_1 \omega_2(\xi_1, \xi_3) + \lambda_2 \omega_2(\xi_2, \xi_3) \\ \omega_2(\xi_1, \xi_2) &= -\omega_2(\xi_2, \xi_1),\end{aligned}$$

$\forall \lambda_1, \lambda_2 \in M$, $\xi_1, \xi_2, \xi_3 \in M^n$. If we also have the extra property that $\omega_2(\xi_1, \xi_2) = 0$, $\forall \xi_2$ implies $\xi_1 = 0$ we say that the 2-form is non-degenerate.

Note that the even dimensionality of our manifold is an important aspect of the definition. It is also important to remark that all the concepts we discuss here in this chapter play an important role in analytical mechanics, since the phase space is always even dimensional.

In a two dimensional space, the determinant of the matrix obtained by the augmentation of two vectors gives the area of the parallelogram described by the two vectors (Golomb 1985). The determinant in this context is also a basic example of a 2-form. This is not a mere coincidence. In general, a differential 2-form at a point (an exterior 2-form on the tangent space at that point) computes a local oriented differential area there. This observation is in a way valid for any k-form, but we are not interested in developing too much geometry in this text.

I mentioned the tangent space. This concept is actually necessary to understand in order to move forward, so let us present a short definition adapted to our interests (Weisstein 2020a):

Definition 3. Let x be a point in our manifold M^{2n} . If we attach a copy of \mathbb{R}^{2n} tangential to M^{2n} at x we obtain a structure called **the tangent space** of M^{2n} at x and we denote it by $T_x M$.

As any concept in differential geometry, it is easy to understand it in spaces with a small number of dimensions. The simplest to visualize in my opinions is the 2D surface of a sphere. If we choose any point on the sphere and stick at that point an infinite plane we obtain the tangent space at that point. The idea of the tangent space is something that people are actually used with from calculus. Say we have a curve on our manifold that passes through x . The

derivative of the curve at \mathbf{x} is a vector in the tangent space. Coming back to our 2D example, on a sphere surface the derivative of a curve on it at a point is tangent to the sphere, so basically a straight arrow tangent to the sphere at that point. But clearly that arrow is not *on* the sphere. It is on the tangent plane part of the tangent space. This is really an extension of the idea in calculus that the derivative gives the slope of the function at a point.

Definition 4. A symplectic form on M^{2n} is a smooth closed non-degenerate 2-form ω_2 on M^{2n} such that the alternating bilinear map $\omega_2^{\mathbf{x}} : T_{\mathbf{x}} M^{2n} \times T_{\mathbf{x}} M^{2n} \rightarrow \mathbb{R}$ defined by the expression of ω_2 at every point $\mathbf{x} \in M^{2n}$ is also non-degenerate.

This may seem quite an abstract and hard to digest idea, so let us dismiss it with a particularization relevant for our problem at hand. If our manifold is \mathbb{R}^{2n} then any 2-form $\omega_2 : \mathbb{R}^{2n} \times \mathbb{R}^{2n} \rightarrow \mathbb{R}$ is symplectic simply if $\omega_2(\mathbf{x}, \mathbf{x}) = 0$ for any \mathbf{x} in \mathbb{R}^n (Weisstein 2020b).

Definition 5. A linear map $A : M^n \rightarrow M^n$ is called *symplectic* if there exists a symplectic form $\omega_2 : M^n \times M^n \rightarrow M$ such that $\omega_2(A\xi, A\eta) = \omega_2(\xi, \eta), \forall \xi, \eta \in M^n$.

For real manifolds we can reformulate this in the following way:

Definition. A linear map $A : \mathbb{R}^n \rightarrow \mathbb{R}^n$ is called *symplectic* if there exists a 2-form ω_2 on \mathbb{R}^{2n} with $\omega_2(\mathbf{x}, \mathbf{x}) = 0, \forall \mathbf{x} \in \mathbb{R}^n$ such that $\omega_2(A\xi, A\eta) = \omega_2(\xi, \eta), \forall \xi, \eta \in \mathbb{R}^n$.

An equivalent condition can be given in matrix form

$$A^T J A = J, \quad (4.55)$$

where $J = \begin{bmatrix} 0_n & I_n \\ -I_n & 0_n \end{bmatrix}$ and I_n is the n -dimensional unitary matrix (remark: $J^{-1} = -J$).

Taking the determinant of each side in the identity 4.55 results that the determinant of the matrix A is ± 1 . We can do better. It is always 1. The proof usually involves using the Pfaffian, but it is possible to avoid this (Rim 2018). Let us make use of the fact that $A^T A$ is symmetric (note that $(A^T A)^T = A^T (A^T)^T = A^T A$). Since $\det(A) \neq 0$, A is invertible, so $A^T A$ is also positive definite.

As a side note we should mention that the simple fact that we found that A is invertible lets us compute the inverse. Indeed,

$$A^T J A = J \Rightarrow A^T J A A^{-1} = A^T J = J A^{-1} \Rightarrow A^{-1} = J^{-1} A^T J. \quad (4.56)$$

We will do a little trick now. $A^T A$ is both symmetric and positive definite. This means that its eigenvalues are real and positive. If \mathbf{v} is an eigenvector of $A^T A$ and λ the corresponding eigenvalue. Then $(A^T A + I_{2n})\mathbf{v} = (\lambda + 1)\mathbf{v}$. This means that the eigenvalues of $A^T A + I_{2n}$ are greater than one. Since the determinant is the product of eigenvalues, we have

$$\det(A^T A + I_{2n}) > 1.$$

We can extract an A^T now

$$A^T A + I_n = A^T (A + (A^T)^{-1}) = A^T (A + J^{-1} A J),$$

such that

$$0 < 1 < \det(A) \det(A + J^{-1} A J). \quad (4.57)$$

Let us write our matrix as $A = \begin{bmatrix} a & b \\ c & d \end{bmatrix}$, with $a, b, c, d \in \mathbb{R}^n$. Now

$$\begin{aligned} A + J^{-1}AJ &= \begin{bmatrix} a & b \\ c & d \end{bmatrix} + \begin{bmatrix} 0_n & -I_n \\ I_n & 0_n \end{bmatrix} \begin{bmatrix} a & b \\ c & d \end{bmatrix} \begin{bmatrix} 0_n & I_n \\ -I_n & 0_n \end{bmatrix} = \\ &= \begin{bmatrix} a & b \\ c & d \end{bmatrix} + \begin{bmatrix} 0_n & -I_n \\ I_n & 0_n \end{bmatrix} \begin{bmatrix} -b & a \\ -d & c \end{bmatrix} = \\ &= \begin{bmatrix} a & b \\ c & d \end{bmatrix} + \begin{bmatrix} d & -c \\ -b & a \end{bmatrix} = \begin{bmatrix} a+d & b-c \\ -(b-c) & a+d \end{bmatrix}. \end{aligned}$$

Denoting $B \equiv a + d$ and $C \equiv b - c$ we can make use of the following decomposition

$$A + J^{-1}AJ = \begin{bmatrix} \frac{1}{\sqrt{2}}I_n & \frac{1}{\sqrt{2}}I_n \\ \frac{i}{\sqrt{2}}I_n & -\frac{i}{\sqrt{2}}I_n \end{bmatrix} \begin{bmatrix} B + iC & 0_n \\ 0_n & B - iC \end{bmatrix} \begin{bmatrix} \frac{1}{\sqrt{2}}I_n & \frac{1}{\sqrt{2}}I_n \\ \frac{i}{\sqrt{2}}I_n & -\frac{i}{\sqrt{2}}I_n \end{bmatrix}^T,$$

Which we can use in equation (4.57)

$$0 < \det(A) \det(B + iC) \det(B - iC) = \det(A) |\det(B + iC)|,$$

which concludes that $\det(A) > 0$.

Together with the fact $\det(A)$ can only take the values ± 1 this completes the proof that **the determinant of the associated matrix of a symplectic linear map is 1**.

This is the complete set of mathematical definitions and nomenclature that develop the concept of symplectic maps. But a question still remains: what difference does it make if a map is symplectic? Well, symplecticity is a generalization of area-preservance (the image of a subset of our manifold through an area-preserving map has the same volume as the subset itself; in this thesis we use volume and area preservence interchangably). In practice it is useful to use the following result in order to decide if this property holds: **a linear map is area-preserving if and only if its associated matrix has the determinant equal to 1**. The proof is omitted since it can be easily found in many places across the internet (also, note that area-preservance is a necessary, but not sufficient condition for symplecticity, considering our previous discussion). Now, looking at phase space, if a linear map is symplectic then, informally, the sum of areas projected on the planes $(\mathbf{q}_i, \mathbf{p}_i)$, $i = \overline{1, n}$ is conserved (Weisstein 2020c), so we can have a lot more quatities conserved. Symplecticity, in this perspective, could be related to generalized angular momenta conservation. Indeed, it has been shown that there are symplectic algorithms (Störmer-Verlet schemese, or modifications of it) which conserve angular momentum exactly (M.-Q. Zhang and Skeel 1995). We must mention that energy conservation is better than symplecticity. In general energy conservation sits above symplecticity, which sits above area-preservance. This may not seem that obvious, since all these three conservation properties are identical in two dimensions and the 2D phase space (1D system) is pretty much the only one our mind can really visualize (a 2D system would have a 4D phase space). The advantage of symplectic or at least volume preserving algorithms is that the energy drift is not diverging and is quite small.

We still have to make one more step in order to study the properties of the Boris push. The problem is that the map that describes this scheme is not linear, so we can not directly use what we presented so far. We simply have to define simplecticity for a larger class of mappings (p. 183 Hairer, Lubich, and Wanner 2006).

Definition 6. A map $f : \mathbb{R}^{2n} \rightarrow \mathbb{R}^{2n}$ is symplectic if its Jacobian matrix is symplectic.

In a similar manner we can define a area-preservance for a wider selection of maps.

Definition 7. A map $f : \mathbb{R}^{2n} \rightarrow \mathbb{R}^{2n}$ is area-preserving if the determinant of its Jacobian matrix is equal to 1.

No matter how we look at all these things, what actually do every time is to check the condition 4.55 for a matrix. We usually call the matrices that solve this identity symplectic. It turns out that for a fixed n the set of all the symplectic matrices form a group (the identity element is I_{2n} , the inverse is given by equation (4.56), proving closure and associativity is trivial). In fact, it is a Lie group commonly denoted as $Sp(2n, \mathbb{R})$. The tangent space at the identity element defines its Lie algebra.

4.3.3 Conservation Properties of the Boris push

In order to check the conservation properties of the Boris push we need to find a way to express equation (4.50) as a matrix equation between the position and velocity at a step and those at the next step. For this we will use the hat map (while it is connected to group theory, we introduce it just as a tool).

Definition 8. For a vector $\mathbf{v} = (v_1, v_2, v_3) \in \mathbb{R}^3$ the corresponding hat map is the matrix

$$\hat{\mathbf{v}} = \begin{bmatrix} 0 & -v_3 & v_2 \\ v_3 & 0 & -v_1 \\ -v_2 & v_1 & 0 \end{bmatrix}.$$

Proposition 1. The vector product of two vectors \mathbf{u} and \mathbf{v} can be expressed with the help of the hat map in the following way

$$\mathbf{u} \times \mathbf{v} = \hat{\mathbf{u}}\hat{\mathbf{v}}.$$

With this preparation we can extract from the Boris push equations

$$\frac{\mathbf{r}_{n+1} - \mathbf{r}_n}{\Delta t} = \mathbf{v}_{n+\frac{1}{2}} \quad (4.58a)$$

$$\frac{\mathbf{v}_{n+\frac{1}{2}} - \mathbf{v}_{n-\frac{1}{2}}}{\Delta t} = \frac{q}{m} \left(\mathbf{E}_n + \frac{\mathbf{v}_{n+\frac{1}{2}} + \mathbf{v}_{n-\frac{1}{2}}}{2} \times \mathbf{B}_n \right) \quad (4.58b)$$

the step update into a more convenient matrix notation

$$\mathbf{r}_{n+1} = \mathbf{r}_n + \Delta t \mathbf{v}_{n+\frac{1}{2}} \quad (4.59a)$$

$$\left(I_3 + \frac{1}{2} \frac{q\Delta t}{m} \hat{\mathbf{B}}_n \right) \mathbf{v}_{n+\frac{1}{2}} = \left(I_3 - \frac{1}{2} \frac{q\Delta t}{m} \hat{\mathbf{B}}_n \right) \mathbf{v}_{n-\frac{1}{2}} + \frac{q\Delta t}{m} \mathbf{E}_n, \quad (4.59b)$$

where I_3 is the three dimensional identity matrix and

$$\hat{\mathbf{B}}_n = \begin{bmatrix} 0 & -B_n^3 & B_n^2 \\ B_n^3 & 0 & -B_n^1 \\ -B_n^2 & B_n^1 & 0 \end{bmatrix}.$$

Since the determinant of $\left(I_3 + \frac{1}{2} \frac{q\Delta t}{m} \hat{\mathbf{B}}_n \right)$ is simply $1 + \left(\frac{1}{2} \frac{q\Delta t}{m} B_n^1 \right)^2 + \left(\frac{1}{2} \frac{q\Delta t}{m} B_n^2 \right)^2 + \left(\frac{1}{2} \frac{q\Delta t}{m} B_n^3 \right)^2 \neq 0$ it has an inverse, so we can further reduce equation (4.59b) to

$$\mathbf{v}_{n+\frac{1}{2}} = \left(I_3 + \frac{1}{2} \frac{q\Delta t}{m} \hat{\mathbf{B}}_n \right)^{-1} \left(I_3 - \frac{1}{2} \frac{q\Delta t}{m} \hat{\mathbf{B}}_n \right) \mathbf{v}_{n-\frac{1}{2}} + \frac{q\Delta t}{m} \left(I_3 + \frac{1}{2} \frac{q\Delta t}{m} \hat{\mathbf{B}}_n \right)^{-1} \mathbf{E}_n. \quad (4.60)$$

For convenience we will make the notation

$$R \equiv \left(I_3 + \frac{1}{2} \frac{q\Delta t}{m} \hat{\mathbf{B}}_n \right)^{-1} \left(I_3 - \frac{1}{2} \frac{q\Delta t}{m} \hat{\mathbf{B}}_n \right), \quad (4.61)$$

so the system of equations for our scheme is now

$$\mathbf{r}_{n+1} = \mathbf{r}_n + \Delta t R \mathbf{v}_{n-\frac{1}{2}} + \frac{q\Delta t^2}{m} \left(I_3 + \frac{1}{2} \frac{q\Delta t}{m} \hat{\mathbf{B}}_n \right)^{-1} \mathbf{E}_n \quad (4.62a)$$

$$\mathbf{v}_{n+\frac{1}{2}} = R \mathbf{v}_{n-\frac{1}{2}} + \frac{q\Delta t}{m} \left(I_3 + \frac{1}{2} \frac{q\Delta t}{m} \hat{\mathbf{B}}_n \right)^{-1} \mathbf{E}_n. \quad (4.62b)$$

The Jacobi matrix of this scheme is

$$\frac{\partial(\mathbf{r}_{n+1}, \mathbf{v}_{n+\frac{1}{2}})}{\partial(\mathbf{r}_n, \mathbf{v}_{n-\frac{1}{2}})} = \begin{bmatrix} \frac{\partial \mathbf{r}_{n+1}}{\partial \mathbf{r}_n} & \frac{\partial \mathbf{r}_{n+1}}{\partial \mathbf{v}_{n-\frac{1}{2}}} \\ \frac{\partial \mathbf{v}_{n+\frac{1}{2}}}{\partial \mathbf{r}_n} & \frac{\partial \mathbf{v}_{n+\frac{1}{2}}}{\partial \mathbf{v}_{n-\frac{1}{2}}} \end{bmatrix} = \begin{bmatrix} I_3 + \Delta t \frac{\partial \mathbf{v}_{n+\frac{1}{2}}}{\partial \mathbf{r}_n} & R \Delta t \\ \frac{\partial \mathbf{v}_{n+\frac{1}{2}}}{\partial \mathbf{r}_n} & R \end{bmatrix}. \quad (4.63)$$

We now have to check if

$$\left[\frac{\partial(\mathbf{r}_{n+1}, \mathbf{v}_{n+\frac{1}{2}})}{\partial(\mathbf{r}_n, \mathbf{v}_{n-\frac{1}{2}})} \right]^T J \frac{\partial(\mathbf{r}_{n+1}, \mathbf{v}_{n+\frac{1}{2}})}{\partial(\mathbf{r}_n, \mathbf{v}_{n-\frac{1}{2}})} = J. \quad (4.64)$$

Under the notation

$$\frac{\partial(\mathbf{r}_{n+1}, \mathbf{v}_{n+\frac{1}{2}})}{\partial(\mathbf{r}_n, \mathbf{v}_{n-\frac{1}{2}})} = \begin{bmatrix} A_1 & A_2 \\ A_3 & A_4 \end{bmatrix}, \quad (4.65)$$

this identity can be expressed as

$$\begin{aligned} & \left[\frac{\partial(\mathbf{r}_{n+1}, \mathbf{v}_{n+\frac{1}{2}})}{\partial(\mathbf{r}_n, \mathbf{v}_{n-\frac{1}{2}})} \right]^T \begin{bmatrix} 0 & I_3 \\ -I_3 & 0 \end{bmatrix} \frac{\partial(\mathbf{r}_{n+1}, \mathbf{v}_{n+\frac{1}{2}})}{\partial(\mathbf{r}_n, \mathbf{v}_{n-\frac{1}{2}})} = \begin{bmatrix} A_1^T & A_3^T \\ A_2^T & A_4^T \end{bmatrix} \begin{bmatrix} 0 & I_3 \\ -I_3 & 0 \end{bmatrix} \begin{bmatrix} A_1 & A_2 \\ A_3 & A_4 \end{bmatrix} = \\ & = \begin{bmatrix} A_1^T & A_3^T \\ A_2^T & A_4^T \end{bmatrix} \begin{bmatrix} A_3 & A_4 \\ -A_1 & -A_2 \end{bmatrix} = \begin{bmatrix} A_1^T A_3 - A_3^T A_1 & A_1^T A_4 - A_3^T A_2 \\ A_2^T A_3 - A_4^T A_1 & A_2^T A_4 - A_4^T A_2 \end{bmatrix} = \begin{bmatrix} 0 & I_3 \\ -I_3 & 0 \end{bmatrix}, \end{aligned}$$

which leads to the following system of matrix equations

$$(A_1^T A_3)^T = A_1^T A_3 \quad (4.66a)$$

$$(A_2^T A_4)^T = A_2^T A_4 \quad (4.66b)$$

$$(A_1^T A_4 - A_3^T A_2)^T = A_1^T A_4 - A_3^T A_2 = I_3. \quad (4.66c)$$

It is quite impossible to work with these equations, since they can be written for any electromagnetic fields. However, if we want to show that the Boris push is not symplectic, a particular

example that doesn't satisfy these identities is enough. Indeed, if we make the choice that the electric and magnetic fields do not depend on position, then $\frac{\partial \mathbf{v}_{\mathbf{n}+\frac{1}{2}}}{\partial \mathbf{r}_n} = 0$, so the A matrices become

$$A_1 = I_3 \quad (4.67a)$$

$$A_2 = R\Delta t \quad (4.67b)$$

$$A_3 = 0 \quad (4.67c)$$

$$A_4 = R. \quad (4.67d)$$

With this choice, equation (4.66c) leads to the obvious contradiction

$$A_1^T A_4 - A_3^T A_2 = R = I_3, \quad (4.68)$$

so the Boris push is not symplectic. But is it area-preserving? To see this we only have to compute the determinant of the Jacobian (4.63) and see if it is equal to 1.

$$\left| \frac{\partial(\mathbf{r}_{\mathbf{n}+1}, \mathbf{v}_{\mathbf{n}+\frac{1}{2}})}{\partial(\mathbf{r}_n, \mathbf{v}_{\mathbf{n}-\frac{1}{2}})} \right| = \begin{vmatrix} I_3 + \Delta t \frac{\partial \mathbf{v}_{\mathbf{n}+\frac{1}{2}}}{\partial \mathbf{r}_n} & R\Delta t \\ \frac{\partial \mathbf{v}_{\mathbf{n}+\frac{1}{2}}}{\partial \mathbf{r}_n} & R \end{vmatrix} \xrightarrow{\text{row1} - \Delta t \text{row2}} \begin{vmatrix} I_3 & 0_3 \\ \frac{\partial \mathbf{v}_{\mathbf{n}+\frac{1}{2}}}{\partial \mathbf{r}_n} & R \end{vmatrix} = |R|. \quad (4.69)$$

Let us denote $\frac{1}{2} \frac{q\Delta t}{m} \hat{\mathbf{B}}_n$ by Ω . By direct calculation we can show that

$$\det(I_3 + \Omega) = \det(I_3 - \Omega) = 1 + \left(\frac{1}{2} \frac{q\Delta t}{m} B_n^1 \right)^2 + \left(\frac{1}{2} \frac{q\Delta t}{m} B_n^2 \right)^2 + \left(\frac{1}{2} \frac{q\Delta t}{m} B_n^3 \right)^2, \quad (4.70)$$

such that

$$|R| = \det((I_3 + \Omega)^{-1}(I_3 - \Omega)) = \det((I_3 + \Omega)^{-1}) \det(I_3 - \Omega) = \frac{\det(I_3 - \Omega)}{\det(I_3 + \Omega)} = 1. \quad (4.71)$$

This concludes the proof that the Boris push is area-preserving.

We will not bother to study also the relativistic algorithm since it is pretty much the same thing with a few changes. In the article by R. Zhang *et al.* 2015, the authors claim to provide a *new* particle pusher that is volume preserving (since, as they say, the relativistic Boris push is not), but it turns out that their original scheme is exactly that of Boris. Nonetheless, the article proves area-preservation for the relativistic Boris push.

4.3.4 The FDTD Maxwell Solver

Since an actual study of the numerical properties of even one single Maxwell solving algorithm is incredibly long due to the large expressions used, we will resume only to presenting the simplest algorithm and its properties. After all, many others are just improved versions of this one.

First of all, we should remark that solving the complete set of Maxwell's equations is too much. But, fortunately, we can actually use just two of them together with the continuity

equation:

$$\frac{\partial \mathbf{B}}{\partial t} = -\nabla \times \mathbf{E} \quad (4.72a)$$

$$\frac{\partial \mathbf{E}}{\partial t} = c^2 \nabla \times \mathbf{B} - c^2 \mu_0 \mathbf{j} \quad (4.72b)$$

$$\frac{\partial \rho}{\partial t} = -\nabla \cdot \mathbf{j}. \quad (4.72c)$$

So what happens with the others? In the case of $\nabla \cdot \mathbf{B} = 0$, if it is satisfied initially, then it remains satisfied all the time as long as equation (4.72a) is satisfied all the time

$$\frac{\partial(\nabla \cdot \mathbf{B})}{\partial t} = \nabla \cdot \frac{\partial \mathbf{B}}{\partial t} = -\nabla \cdot (\nabla \times \mathbf{E}) = 0.$$

As for $\nabla \cdot \mathbf{E} = \frac{\rho}{\varepsilon_0}$, it is valid if it is satisfied initially as long as equations (4.72b) and (4.72c) are satisfied all the time

$$\frac{\partial}{\partial t} \left(\nabla \cdot \mathbf{E} - \frac{\rho}{\varepsilon_0} \right) = \nabla \cdot \frac{\partial \mathbf{E}}{\partial t} - c^2 \mu_0 \frac{\partial \rho}{\partial t} = c^2 \nabla \cdot (\nabla \times \mathbf{B}) - c^2 \mu_0 \left(\frac{\partial \rho}{\partial t} - \nabla \cdot \mathbf{j} \right) = 0.$$

In all our previous discussions on numerical methods for solving differential equations we only had to discretize the time domain in order to obtain the integration scheme. This time it is not enough, since we also have derivatives with respect to all three spatial coordinates. The standard approach to discretize the fields in this case is to use a Yee staggered grid (Kane Yee 1966), illustrated in figure 4.3. This choice is extremely convenient when it comes to computing curls, since we can relate them to a circulation integral around one face.

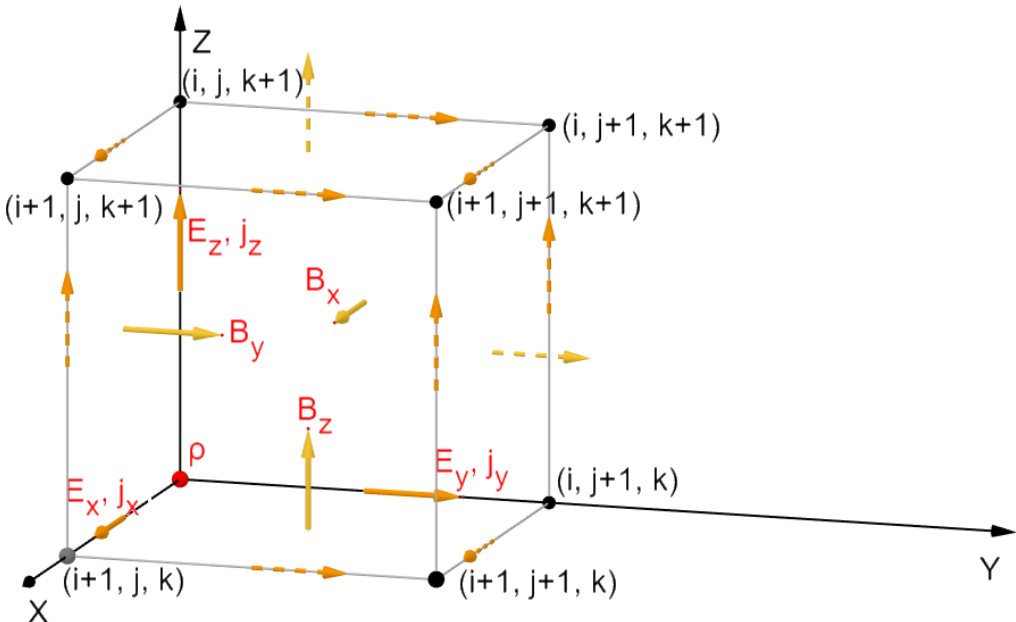


Figure 4.3: The Yee staggered grid for the FDTD solver

We will now provide an example of how to use the Yee grid to discretize the Maxwell equations. Let us look at the bottom side of the cube, which is connected to equation (4.72a).

If the discretization steps are Δx , Δy , and Δz , then we can equate the circulation of the electric field to the time derivative of the magnetic field flux

$$\begin{aligned} & \left(E_x^n \left(i + \frac{1}{2}, j, k \right) - E_x^n \left(i + \frac{1}{2}, j + 1, k \right) \right) \Delta x + \left(E_y^n \left(i + 1, j + \frac{1}{2}, k \right) - E_y^n \left(i, j + \frac{1}{2}, k \right) \right) \Delta y = \\ & = - \frac{B_z^{n+\frac{1}{2}} \left(i + \frac{1}{2}, j + \frac{1}{2}, k \right) - B_z^{n-\frac{1}{2}} \left(i + \frac{1}{2}, j + \frac{1}{2}, k \right)}{\Delta t} \Delta x \Delta y, \end{aligned}$$

where n is the index of time discretization. Note that since the time variation of one field depends on the other field, it is better to discretize the differentiated field at half integer time steps to have a leapfrog like time derivative. Now we can divide by the area of the side $\Delta x \Delta y$ to obtain

$$\begin{aligned} & - \frac{E_y^n \left(i + 1, j + \frac{1}{2}, k \right) - E_y^n \left(i, j + \frac{1}{2}, k \right)}{\Delta x} + \frac{E_x^n \left(i + \frac{1}{2}, j + 1, k \right) - E_x^n \left(i + \frac{1}{2}, j, k \right)}{\Delta y} = \\ & = \frac{B_z^{n+\frac{1}{2}} \left(i + \frac{1}{2}, j + \frac{1}{2}, k \right) - B_z^{n-\frac{1}{2}} \left(i + \frac{1}{2}, j + \frac{1}{2}, k \right)}{\Delta t}. \end{aligned}$$

All other equations are deduced similarly. In order to present all of them we will employ the following notation (Lehe 2016a):

$$\begin{aligned} F_\alpha^n(i, j, k) & \equiv F_{\alpha i, j, k}^n \\ \frac{F_{\alpha i, j, k}^{n+\frac{1}{2}} - F_{\alpha i, j, k}^{n-\frac{1}{2}}}{\Delta t} & \equiv \partial_t F_\alpha|_{i, j, k}^n \\ \frac{F_{\alpha i+\frac{1}{2}, j, k}^n - F_{\alpha i-\frac{1}{2}, j, k}^n}{\Delta x} & \equiv \partial_x F_\alpha|_{i, j, k}^n \\ \frac{F_{\alpha i, j+\frac{1}{2}, k}^n - F_{\alpha i, j-\frac{1}{2}, k}^n}{\Delta y} & \equiv \partial_y F_\alpha|_{i, j, k}^n \\ \frac{F_{\alpha i, j, k+\frac{1}{2}}^n - F_{\alpha i, j, k-\frac{1}{2}}^n}{\Delta z} & \equiv \partial_z F_\alpha|_{i, j, k}^n, \end{aligned}$$

where $\alpha \in \{t, x, y, z\}$ and $F \in \{E, B\}$. With this, equation (4.72a) becomes

$$\partial_t B_x|_{i, j+\frac{1}{2}, k+\frac{1}{2}}^n = -\partial_y E_z|_{i, j+\frac{1}{2}, k+\frac{1}{2}}^n + \partial_z E_y|_{i, j+\frac{1}{2}, k+\frac{1}{2}}^n \quad (4.73a)$$

$$\partial_t B_y|_{i+\frac{1}{2}, j, k+\frac{1}{2}}^n = -\partial_z E_x|_{i+\frac{1}{2}, j, k+\frac{1}{2}}^n + \partial_x E_z|_{i+\frac{1}{2}, j, k+\frac{1}{2}}^n \quad (4.73b)$$

$$\partial_t B_z|_{i+\frac{1}{2}, j+\frac{1}{2}, k}^n = -\partial_x E_y|_{i+\frac{1}{2}, j+\frac{1}{2}, k}^n + \partial_y E_x|_{i+\frac{1}{2}, j+\frac{1}{2}, k}^n, \quad (4.73c)$$

equation (4.72b) becomes

$$\partial_t E_x|_{i+\frac{1}{2}, j, k}^{n+\frac{1}{2}} = c^2 \partial_y B_z|_{i+\frac{1}{2}, j, k}^{n+\frac{1}{2}} - c^2 \partial_z B_y|_{i+\frac{1}{2}, j, k}^{n+\frac{1}{2}} - c^2 \mu_0 j_x|_{i+\frac{1}{2}, j, k}^{n+\frac{1}{2}} \quad (4.74a)$$

$$\partial_t E_y|_{i, j+\frac{1}{2}, k}^{n+\frac{1}{2}} = c^2 \partial_z B_x|_{i, j+\frac{1}{2}, k}^{n+\frac{1}{2}} - c^2 \partial_x B_z|_{i, j+\frac{1}{2}, k}^{n+\frac{1}{2}} - c^2 \mu_0 j_y|_{i, j+\frac{1}{2}, k}^{n+\frac{1}{2}} \quad (4.74b)$$

$$\partial_t E_z|_{i, j, k+\frac{1}{2}}^{n+\frac{1}{2}} = c^2 \partial_x B_y|_{i, j, k+\frac{1}{2}}^{n+\frac{1}{2}} - c^2 \partial_y B_x|_{i, j, k+\frac{1}{2}}^{n+\frac{1}{2}} - c^2 \mu_0 j_z|_{i, j, k+\frac{1}{2}}^{n+\frac{1}{2}}, \quad (4.74c)$$

and equation (4.72a) becomes

$$\partial_t \rho|_{i,j,k}^{n+\frac{1}{2}} + \partial_x j_x|_{i,j,k}^{n+\frac{1}{2}} + \partial_y j_y|_{i,j,k}^{n+\frac{1}{2}} + \partial_z j_z|_{i,j,k}^{n+\frac{1}{2}} = 0. \quad (4.75)$$

Obtaining the charge density ρ is the job of the current deposition scheme. In order for everything to be correct we also have to impose the following initial conditions to the electromagnetic field (not the standard choice, but rather an illustrative one related to the previous discussion about the Gauss laws)

$$\partial_x B_x|_{i+\frac{1}{2},j+\frac{1}{2},k+\frac{1}{2}}^{\frac{1}{2}} + \partial_y B_y|_{i+\frac{1}{2},j+\frac{1}{2},k+\frac{1}{2}}^{\frac{1}{2}} + \partial_z B_z|_{i+\frac{1}{2},j+\frac{1}{2},k+\frac{1}{2}}^{\frac{1}{2}} = 0 \quad (4.76a)$$

$$\partial_x E_x|_{i,j,k}^0 + \partial_y E_y|_{i,j,k}^0 + \partial_z E_z|_{i,j,k}^0 = \frac{\rho_{i,j,k}^0}{\epsilon_0}. \quad (4.76b)$$

4.3.5 Stability of the FDTD Scheme

In this subsection we want to analyze the stability of the FDTD scheme. However, working directly with the 3D equations is quite difficult due to their length. We will instead try to study the 1D scheme and then use it as a model to offer the 3D result.

It is hard to imagine what it means to have 1D Maxwell equations, since the definitions of divergence and curl don't make that much sense in 1D spaces. By reducing to 1D, we really mean to simply take the directions of the electric and magnetic fields fixed, like it is done in Lehe 2016b. Let us take E along the x -axis and B along the y -axis. In this case, our system's spacial dimension is only the z -axis. The field equations of the FDTD scheme become

$$\partial_t B_y|_{k+\frac{1}{2}}^n = -\partial_z E_x|_{k+\frac{1}{2}}^n \quad (4.77a)$$

$$\partial_t E_x|_k^{n+\frac{1}{2}} = c^2 \partial_z B_y|_k^{n+\frac{1}{2}}. \quad (4.77b)$$

The current term disappears since there is no j_x . We can also rewrite more explicitly these relations (I dropped the subscripts of the fields since they are redundant as we fixed the directions)

$$\frac{B_{k+\frac{1}{2}}^{n+\frac{1}{2}} - B_{k+\frac{1}{2}}^{n-\frac{1}{2}}}{\Delta t} = -\frac{E_{k+1}^n - E_k^n}{\Delta z} \quad (4.78a)$$

$$\frac{1}{c^2} \frac{E_k^{n+1} - E_k^n}{\Delta t} = -\frac{B_{k+\frac{1}{2}}^{n+\frac{1}{2}} - B_{k-\frac{1}{2}}^{n+\frac{1}{2}}}{\Delta z}. \quad (4.78b)$$

We can combine these to obtain a propagation relation that uses the same second derivative numerical approximation we have encountered before when talking about the leapfrog algorithm

$$\begin{aligned} \frac{1}{c^2} \frac{E_k^{n+1} - E_k^n}{\Delta t^2} - \frac{1}{c^2} \frac{E_k^n - E_k^{n-1}}{\Delta t^2} &= -\frac{B_{k+\frac{1}{2}}^{n+\frac{1}{2}} - B_{k-\frac{1}{2}}^{n+\frac{1}{2}}}{\Delta z \Delta t} + \frac{B_{k+\frac{1}{2}}^{n-\frac{1}{2}} - B_{k-\frac{1}{2}}^{n-\frac{1}{2}}}{\Delta z \Delta t} = \\ &= -\frac{B_{k+\frac{1}{2}}^{n+\frac{1}{2}} - B_{k+\frac{1}{2}}^{n-\frac{1}{2}}}{\Delta z \Delta t} + \frac{B_{k-\frac{1}{2}}^{n+\frac{1}{2}} - B_{k-\frac{1}{2}}^{n-\frac{1}{2}}}{\Delta z \Delta t} = \frac{E_{k+1}^n - E_k^n}{\Delta z^2} - \frac{E_k^n - E_{k-1}^n}{\Delta z^2} \Rightarrow \end{aligned}$$

$$\Rightarrow \frac{1}{c^2} \frac{E_k^{n+1} - 2E_k^n + E_k^{n-1}}{\Delta t^2} = \frac{E_{k+1}^n - 2E_k^n + E_{k-1}^n}{\Delta z^2}. \quad (4.79)$$

Back in section 4.1.6 we applied different schemes to the harmonic oscillator in order to study their stability. We will use slightly more general idea now, which still capitalizes on oscillations, namely the von Neumann analysis. We start by assuming that we obtain numerical results up to machine precision. In this case, equation (4.79) is also satisfied by the round-off error $\epsilon_k^n = N_k^n - E_k^n$, where N_k^n is the numerical solution obtained through the finite precision scheme. We let the error have a wave form (*i.e.* we use an oscillating small perturbation)

$$\epsilon_k^n = \epsilon_0 e^{i(k_w k \Delta z - \omega n \Delta t)}, \quad (4.80)$$

and look at how it evolves in time. Replacing in equation (4.79), we have

$$\begin{aligned} & \frac{1}{c^2} \frac{\epsilon_k^{n+1} - 2\epsilon_k^n + \epsilon_k^{n-1}}{\Delta t^2} = \frac{\epsilon_{k+1}^n - 2\epsilon_k^n + \epsilon_{k-1}^n}{\Delta z^2} \Rightarrow \\ & \Rightarrow \frac{\Delta z^2}{c^2 \Delta t^2} (e^{i\omega \Delta t} + e^{-i\omega \Delta t} - 2) \epsilon_0 e^{i(k_w k \Delta z - \omega n \Delta t)} = (e^{ik_w \Delta z} + e^{-ik_w \Delta z} - 2) \epsilon_0 e^{i(k_w k \Delta z - \omega n \Delta t)} \Rightarrow \\ & \Rightarrow \frac{\Delta z^2}{c^2 \Delta t^2} [\cos(\omega \Delta t) - 1] = [\cos(k_w \Delta z) - 1] \Rightarrow \\ & \Rightarrow \frac{\Delta z^2}{c^2 \Delta t^2} \sin^2\left(\frac{\omega \Delta t}{2}\right) = \sin^2\left(\frac{k_w \Delta z}{2}\right) \Rightarrow \\ & \Rightarrow \sin\left(\frac{\omega \Delta t}{2}\right) = \pm \frac{c \Delta t}{\Delta z} \sin\left(\frac{k_w \Delta z}{2}\right). \end{aligned} \quad (4.81)$$

We can now see that in order for this numerical dispersion relation to hold we must have $c \Delta t \leq \Delta z$. Otherwise, if $c \Delta t > \Delta z$, equation (4.81) can only give a complex solution for ω . This would in turn change the complex exponential in the ansatz 4.80 to a real exponential, which would eventually blow up. The conclusion now is that the stability condition for the 1D FDTD scheme is

$$c \leq \frac{\Delta z}{\Delta t}, \quad (4.82)$$

which is called in literature the Courant condition. For the 3D scheme, we would have to work with the complete set of equations. We can again obtain a numerical wave equation, do von Neumann error analysis (this time including in our ansatz oscillatory terms in all spatial direction), and we would eventually obtain a very similar result

$$c \leq \frac{\sqrt{\Delta x^2 + \Delta y^2 + \Delta z^2}}{\Delta t}. \quad (4.83)$$

4.4 Particle-in-cell in Practice

So far, even though it might seem like a lot, we have only scratched the surface of the structure of PIC codes. There are many other schemes we left out and countless improvements for speed and accuracy. Actual PIC codes are humongous well-optimized codes of thousands of lines, so

building your own code from zero is not an achievable goal unless you are willing to spend a couple of years on it. As a result, there are lots of complete PIC software already available, each one the result of years of work. There is also an aspect we haven't touched yet, and that is computational power. We still have to put in our system a couple thousands or even tens of thousands of superparticles to obtain a good statistical result. In order to do this, we really need our code to be parallelized and ready to run on servers and clusters. This section aims to offer an overview of these aspects, as well as some indications on how to prepare simulations with such software in general.

4.4.1 Conditions and Restrictions for a Successful Simulation

Before even discussing the codes, I want to put all the conditions one must check for the input parameters (in principle the discretization step-sizes) that are mandatory in order to be able to trust the results of a simulation.

Since our simulation will include electromagnetic waves that might arise in the plasma medium, we must make certain that we have at least a couple of steps per oscillation cycle in order to accurately represent it. But how can we say anything about the waves that might arise (in particular, frequency)? In the plasma chapter we discussed that any electromagnetic wave with a frequency smaller than the plasma frequency (which is proportional to the square root of the electron particle density) can not propagate through the plasma. This means that we must choose our time-step such that the plasma frequency is well represented. Since all the waves in the system will have the frequency higher than the plasma frequency, we are sure to correctly represent each wave. The condition is usually written as

$$\Delta t \leq \frac{2}{\omega_p}. \quad (4.84)$$

However, practical considerations related to energy conservation require an even more strict condition. It usually depends also on the computation power you have at your disposal, but, in practice, many usually take at least $\Delta t \leq \frac{0.1}{\omega_p}$. Further note that these inequalities actually relate the time step to the electron number density. We can relax our restriction on the time step by introducing more particles in our system. In this perspective, there is a trade off one needs to balance, since more particles slow down the simulation, while larger time steps let us advance the simulation time faster in order to reach the desired phenomena faster.

We have also discussed how the effect of charge accumulation in plasmas is completely screened over distances of a couple Debye lengths. We need to make sure that we choose the space grid such that distances of this order are accurately represented. Thus we usually want to have

$$\Delta x, \Delta y, \Delta z < 3\lambda_D. \quad (4.85)$$

This time around, the Debye length depends on the inverse of the square root of the electron number density. As such, including more particles forces us to use a finer grid.

Finally, we must also include the courant condition we just deduced at the end of the previous section

$$c \leq \frac{\sqrt{\Delta x^2 + \Delta y^2 + \Delta z^2}}{\Delta t}. \quad (4.86)$$

This together with the previous relation affect our choice of spatial step-sizes. It is important to understand the physics of the system you want to simulate in order to optimize your input

parameter. For example, if your system's evolution is of more interest along one direction compared with the others (in the case of laser wakefield acceleration, the propagation direction of the laser beam), one can make the grid finer along the important axis.

With these constraints in mind, PIC codes can be used without much thought for what happens inside them, as long as you understand the physics you want to study. However, good knowledge about the method and the specific implementation you are running are useful in order to understand the causes of any problem or unphysical solution that might arise.

4.4.2 Currently Available PIC Codes and High Performance Computing

I may have reapeated this a couple of times now, but it is extremely important to have this fact in your mind when using PIC software: Particle-in-cell simulations are resource intensive. That is due to the fact that they must solve several equations for each superparticle at each time step and they must do this selfconsistently, which requires juggling with tons of data at once. These codes are definitely not made for your every day computer or small workstation, but rather for supercomputers. As such, PIC codes must fall in the High Performance Computing area (HPC). For those that haven't dealt with this topic before, HPC refers to practices aiming to optimize the use of computing power in a way that delivers high performance in terms of processing speed, data manipulation and management, and other such aspects. This has a technical side involving advancens in building and connecting supercomputing units and a software design side in the sense that the codes must be written in such a way that they can make use of the advanced hardware implementation.

In the particular context of PIC software developement, it boils down to using various types of parallelism (the majority use the MPI–Message Passing Interface–standard, but many don't stop there, like Osiris, which uses shared memory paralelism and instruction level paralelism Fiuzza *et al.* 2011), coming up more efficient subroutines and other such aspects. A quite in depth review of everything related to this topic can be found in Micluță–Câmpeanu 2019. We will only continue by shortly presenting some really briliant and inovative codes (two of which are the state of the art in PIC).

The aforementioned **Osiris** was developed with the idea of Cohen, Kemp, and Divol 2010 in mind. They use a standard PIC algorithm which solves the complete set of Maxwell equations for low-density high-temperature regions (where kinetic effects are more relevant), while in high-density low-temperature regions (where collisions can't really be neglected) they use o reduced set of equations that boils down to Ohm's and Faraday's laws (refered to usually as a hybrid-PIC, since it combines fluid and single particle equations). The resulting code is fully relativistic and massively paralelized.

The second state of the art software is **Wrap-X** (Tarentino and Maley 1975), which is mostly designed with plasma based acceleration related simulations in mind. It actually combines three frameworks: Wrap (for modeling plasmas and accelerators), AMReX (Adaptive Mesh Refinement library) and PICSAR (which was the low level PIC primitives). It is designed to run at exa-scale, yet it uses highly accurate and stable high order methods like the PSATD field solver (Vincenti and Vay 2018).

Although not state of the art this time, **PIConGPU** (Burau *et al.* 2010) is inovative through the fact that they managed to write a fully relativistic 3D code that can run on GPU clusters, thus opening a new direction for PIC software developement.

4.5 EPOCH

In the work presented in this thesis I chose to work with EPOCH (Arber *et al.* 2015). It is primarily due to its ease of use and set up. Besides a very comprehensive and easy to follow documentation (Bennett *et al.* n.d.), there are also numerous examples of use at *Basic Examples of Using EPOCH* 2020, as well as in the theses of O’Neil 2017, Micluță-Câmpleanu 2019, and Valenta 2017.

4.5.1 Software Input

EPOCH uses input files in which one writes the simulation parameters and the objects used (the particles, laser fields, electromagnetic fields). One can also specify what routines to use for some integrators. The input file must contain several separated blocks. While some have a quite obvious connection between name and content, like boundaries, species, fields, laser, window, constants, and output, there are also a couple that are not that obvious, but are still easy to understand after you read about them, like control (which specifically contains specifications about the geometry and size of the domain, the initial conditions and the choice of routines), qed (which has information about pair production effects), subset (which contains filter configuration used to modify the output). One can also have access to a lot of the variables used in the simulation. For example, one can obtain pretty much any relevant quantity: momenta, velocities, positions, charge, mass, particle weight (*i.e.* how many real particles are in a pseudo-particle), energy, and work exerted by the fields on the particles.

Chapter 5

Results

This chapter covers the results from the numerical simulations that I've run using the EPOCH Particle-in-Cell code. The main focus of the study is to analyze the use of Laguerre-Gauss modes in laser wakefield accelerators and to compare their behaviour with that of simple Gaussian modes as well as to study the yield of photons in a structured target hit by laser as a function of geometric parameters. The simulations were performed using the computing cluster from the Departament of Computational Physics and Information Technology of the National Institute of Physics and Nuclear Engineering. The servers used had an Intel® Xeon® E 5-2640 v4 2.4 GHz (3.4 GHz Turbo Boost) processor. Each server has 10 cores per socket and 128 GB RAM memory. MPI was used for parallelization, and benchmarks showed that running with Hyper-Threading or running on two servers at once improves the computation time significantly. For all simulations I chose the latter option, the average simulation time being somewhere between half a day and a full day (the duration is so long because all the simulations were 3D).

5.1 Low intensity laser simulations

The first set of simulations was done with low intensity $1 \mu\text{m}$ wavelength lasers, namely $a_0 = 2$, or, equivalently, $I = 5.65 \times 10^{18} \text{ W/cm}^2$. Also, $w_0 = 5\lambda$ was chosen. The domain size was $60\lambda \times 30\lambda \times 30\lambda$, discretized with a grid of $1200 \times 300 \times 300$. Notice that the grid is much finer on the x direction (in our simulations this is the propagation direction) than in the y and z directions. This is done in order to reduce the computation time, since the main physical effects as well as the structures we want to observe are along the propagation direction of the laser. There are three such simulations, one with the Gauss beam, and two with the ($m = 1, p = 0$) and ($m = 2, p = 0$) Laguerre-Gauss beams. An example of input.deck file with comments about how the different profiles are implemented is given in the Appendix.

With this first set of simulations we are interested to see if coherent beams of accelerated electrons are formed and to compare the acceleration efficiency across the different laser profiles used. For the second purpose, the energy density (the product between the average energy per particle and the particle number density, computed locally at each point on the grid) of the electrons was found to be a relevant quantity. This is because, in the region of the accelerated beam, both the average electron energy and the electron number density are high compared with the rest of the electrons in the medium. As such, this energy density has visible spikes at the location of the electron beam. We can also use the maximum of this quantity at each time step to follow the acceleration process and its efficiency (while the exact values are to be taken with a grain of salt, we can extract information from trends and orders of magnitude). It is known that in the process of acceleration in LWFA, there is first an increase in the electron

beam energy and then a decrease. As such, this method is efficient over a certain region, and knowing the limits of that region is important when designing the actual accelerators. This pattern of variation is also observed in the maximum values of the electron energy density taken at each step. In the following figures, details related to this and other aspects are illustrated. All figures have the corner facing the reader clipped in order to see inside the structures formed (the structures are highly symmetrical).

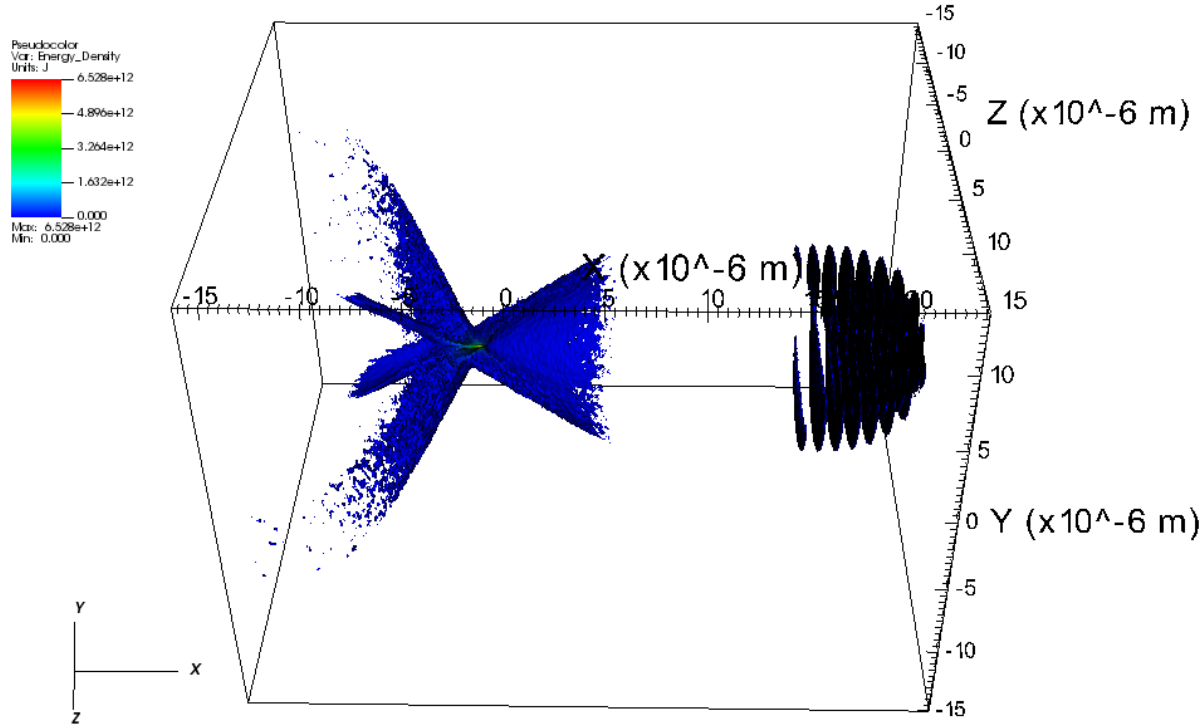


Figure 5.1: A pseudocolor plot cut with isosurfaces of the electron energy density that shows more levels for low values. This is done in order to observe the plasma wave electrons, such that the beam, as well as the bubble shape and the laser position can be seen clearly. We see that since the intensity is low, the bubble is not depleted completely, and we can clearly see the electrons interacting with the laser. At high intensity, the ponderomotive force is much larger and the electrons are pushed outside the laser region very fast, so the bubble is depleted of electrons.

As shown in figure 5.1, there is a singular clear coherent beam of accelerated electrons. Close-ups on the beam are shown in figure 5.2. In contrast, figure 5.5 reveals that the plasma wave generated by the passing of the laser through the plasma is much more complicated for the Laguerre modes. There is no longer a clear bubble-beam-bubble pattern visible, and as such we can see no longer a clear electron beam forming on the propagation axis. However, figures 5.3 and 5.4 shed light on this matter. It seems that there are electron beams forming, but there are two of them for $m=1$ and four of them for $m=4$. We connect this occurrence with the topology of the profiles. It is clear what we mean by this if we first take a look at figures 5.6 and 5.7. We can see that the plots of the magnitude of the electric field (which reflect the geometrical shape of each profile, since the field of the particles is screened by plasma mechanisms) show one connected structure in the case of the Gauss beam, but in the case of the Laguerre profiles there are disjointed structures. The number of disjointed structures is equal to the number of electron beams forming and is also equal to $2m$. This, together with the visual hints in figures 5.3 and 5.4

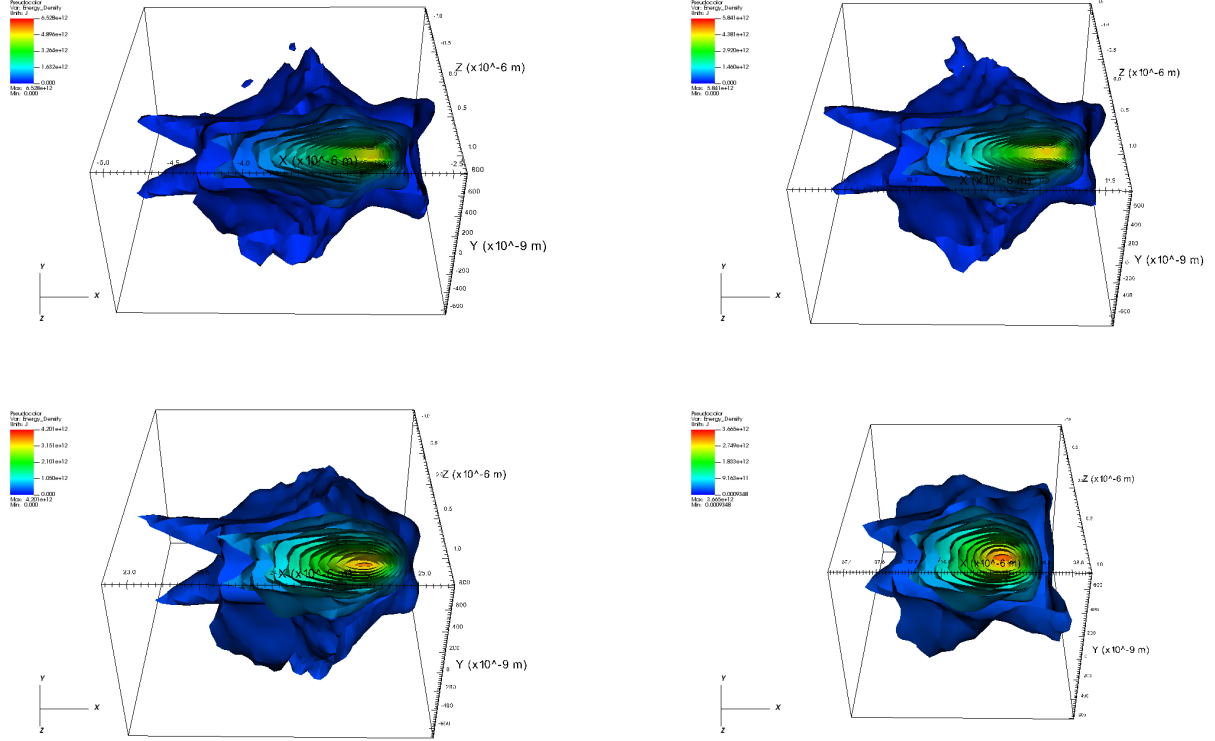


Figure 5.2: A series of pseudocolor plots of the electron energy density using isosurfaces showing the electron beam at different moments in time: 200 fs (top-right), 250 fs (top-left), 300 fs (bottom-right), 350 (bottom-left).

(the electron beams are formed behind each structure) suggest that the independent effect of each structure is not strongly influenced the other structures, so each of them acts like a Gauss beam on its own.

Maximum Value of Electron Energy Density					
Gauss m=0		Laguerre m=1		Laguerre m=2	
Enrgy Value (10^{10} J/m 3)	Simulation Time (fs)	Enrgy Value (10^{10} J/m 3)	Simulation Time (fs)	Enrgy Value (10^{10} J/m 3)	Simulation Time (fs)
652.8	200	34.3	180	11	160
584.1	250	28.1	230	9.9	210
420.1	300	18.4	280	6.2	260
366.5	350	8.4	330	8.8	310
500.6	400	4.7	380	2.66	360

Table 5.1: A table with the maximum value of electron energy density at different time steps. The first value for each profile was taken to be the overall maximum in the simulation, which corresponds to the moment of time in which the acceleration has peaked. After that, values are taken in intervals of 50 fs. The data reflects the post acceleration energy loss part of the LWFA process.

One possible physical explanation for this effect would be related to the intensity of the lasers. Since the intensity is quite low, so is the ponderomotive force. Because of this, there are still electrons remaining in the laser region, which oscillate in the laser's fields until they get out,

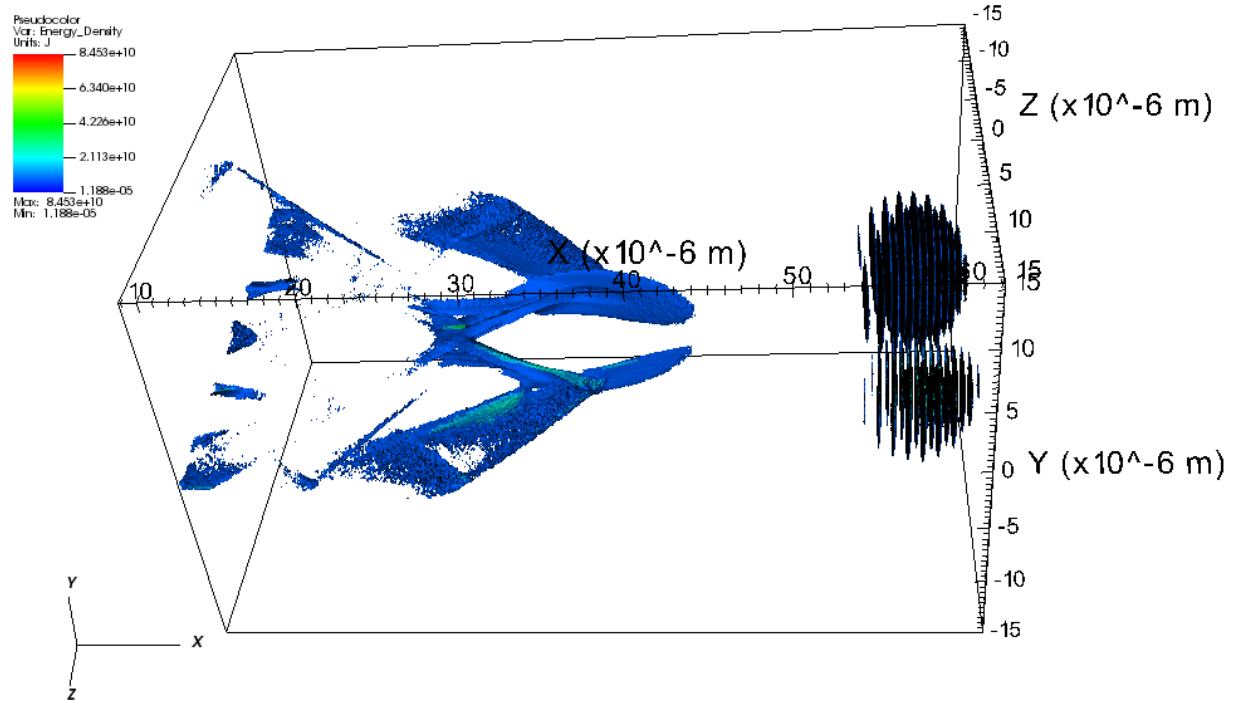


Figure 5.3: A pseudocolor plot cut with isosurfaces (10) of the electron energy density for the $m=1$, $p=0$ Laguerre-Gauss mode (330 fs).

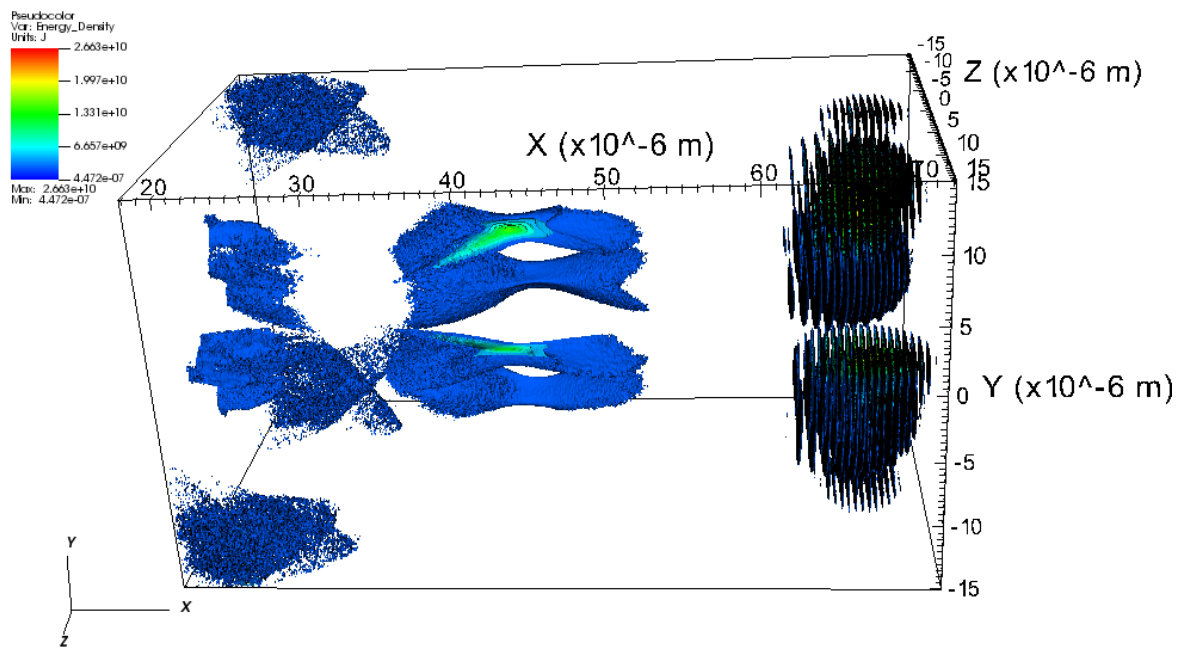


Figure 5.4: A pseudocolor plot cut with isosurfaces (10) of the electron energy density for the $m=2$, $p=0$ Laguerre-Gauss mode (360 fs).

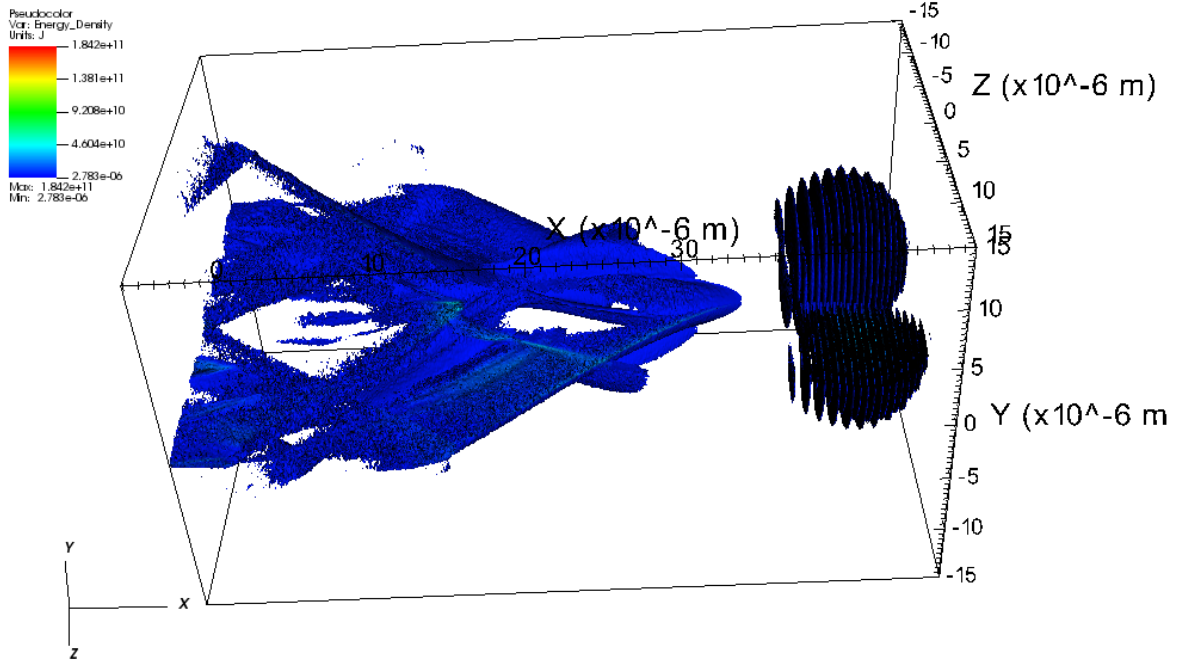


Figure 5.5: A pseudocolor plot cut with isosurfaces (50) of the electron energy density for the $m=1$, $p=0$ Laguerre-Gauss mode (280 fs). We made a large number of isosurfaces to see the much more complicated patterns of the low energy electrons compared to the very simple one in the case of the regular Gauss profile.

and are almost equally probable to leave through the outside as well through the in between region. We say almost because in figures 5.8 and 5.9 we can see a small ponderomotive force component towards the center region. These electrons could leave through the space in between the lumps of the Laguerre beams, as visible in figure 5.5. Also, there is no ponderomotive force in the space between the structures as shown in figures 5.8 and 5.9, so thermal electrons passing through there don't interact strongly with the laser. This effect is expected to disappear at higher intensities, since the laser region is expected to be depleted of electrons extremely fast. Nonetheless, the effect in itself could possess practical application. This study suggests that for intensities of the order of 10^{18} W/cm^2 , by utilizing Laguerre-Gauss modes, it is possible to obtain multiple beams of accelerated electrons arranged in well defined patterns. In table 5.1, we show values of the electron energy density in order to compare the acceleration efficiency across different profiles. By analyzing the data, we saw that the maximum value of this quantity follows the pattern of acceleration followed by slow down, which is characteristic to LWFA. The values in the table start with the overall maximum (the peak of acceleration) and follow the energy loss in time after that. We can see that by increasing m with one unit at a time we see a loss of energy density in the beams of about one order of magnitude. So, there is a trade off between the number of beams achieved in this manner and the efficacy of the accelerator. This supports the theory that each of the structures in the Laguerre beams acts as an almost independent weaker Gaussian beam at low intensities.

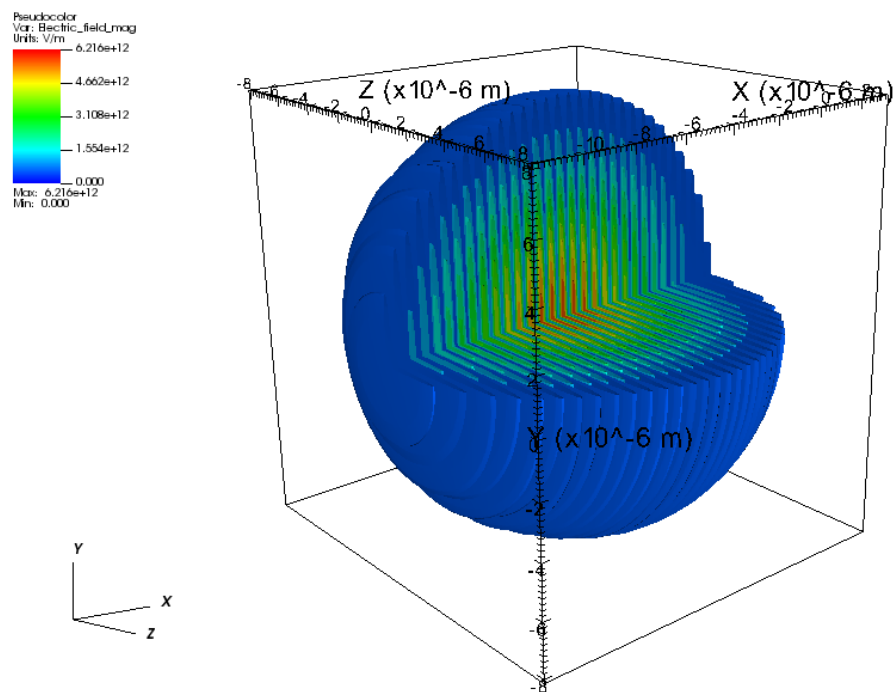


Figure 5.6: A pseudocolor plot cut with isosurfaces of the magnitude of the electric field vector at each of the grid points in the case of the simple Gaussian profile. This plot indicates the shape of the profile.

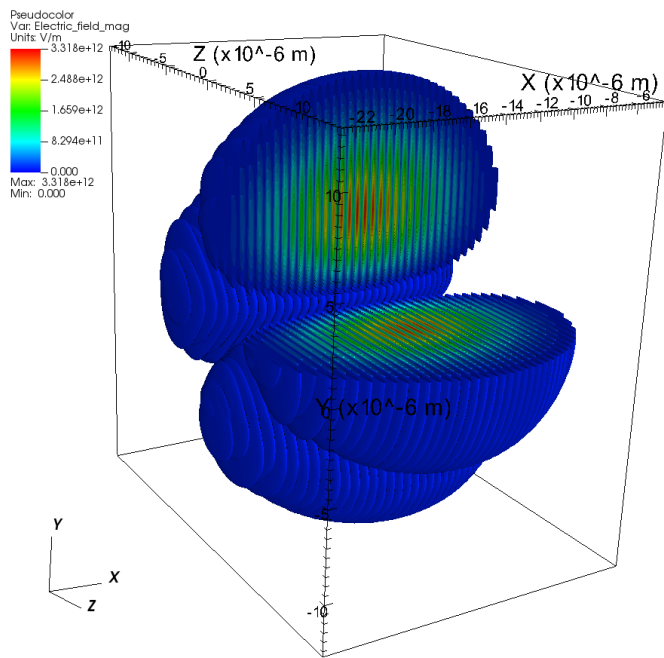
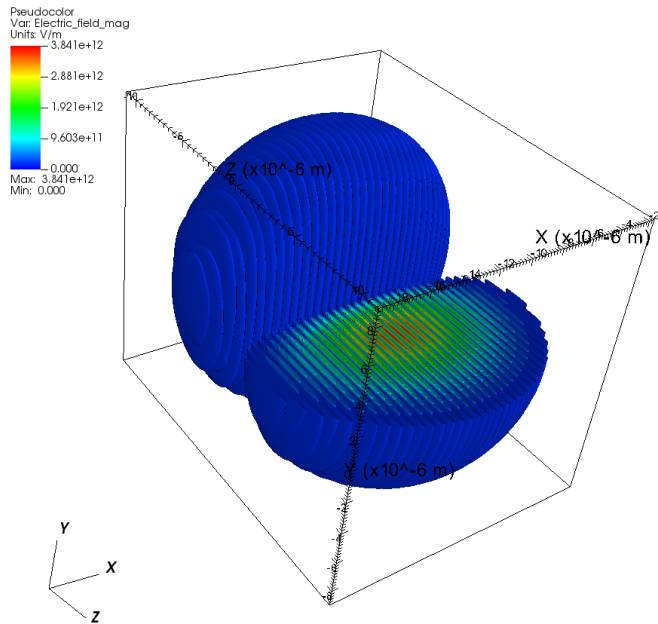


Figure 5.7: A series of pseudocolor plots cut with isosurfaces of the magnitude of the electric field vector at each of the grid points in the case of the $m=1$, $p=0$ (top) and the $m=2$, $p=0$ Laguerre-Gauss profiles. This plot indicates the shape of the profiles.

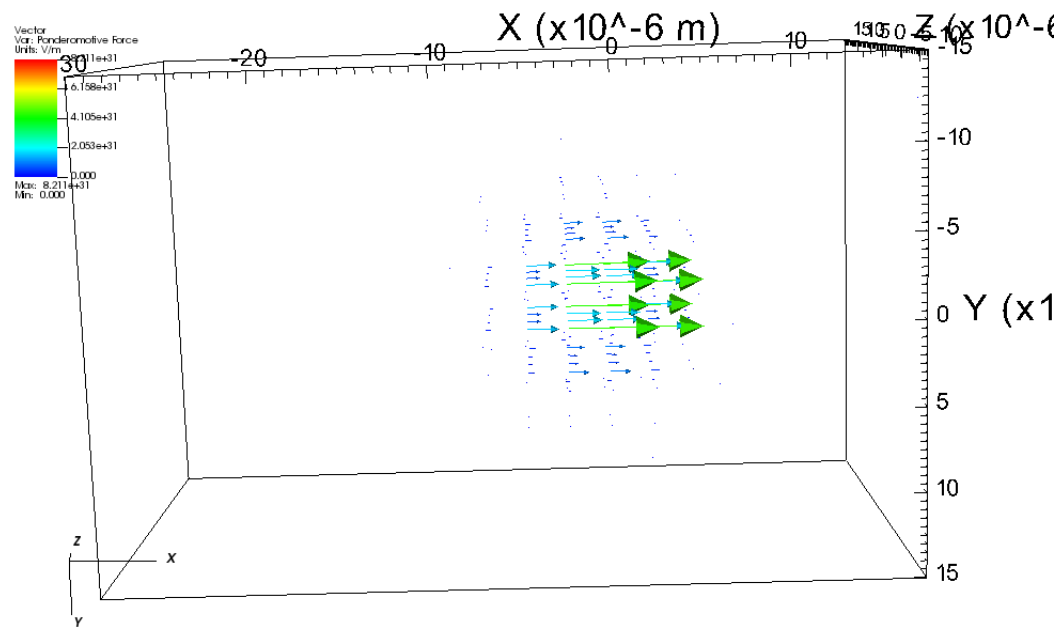
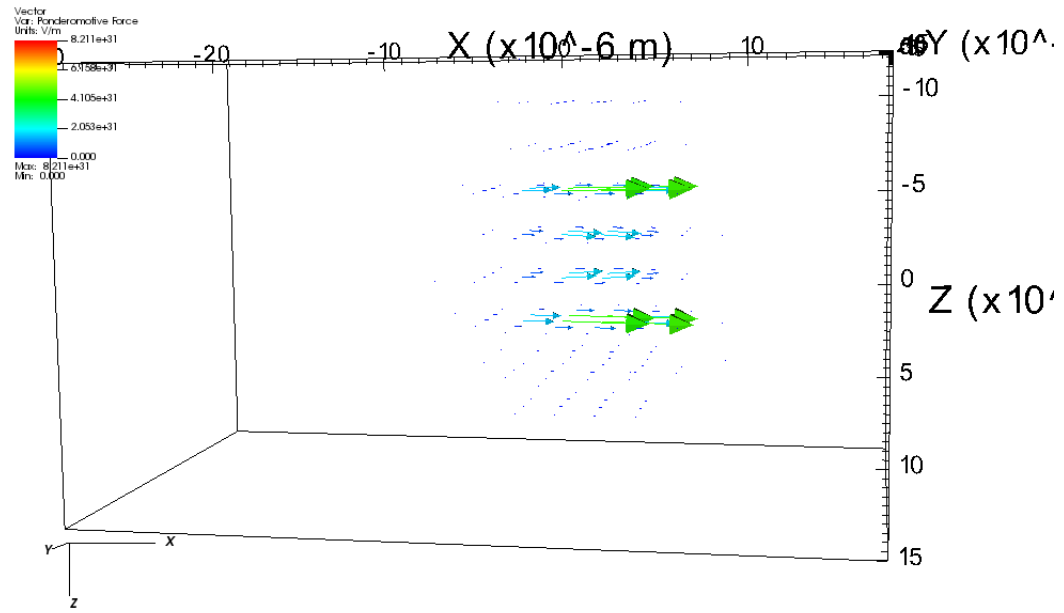


Figure 5.8: Vector plots showing the ponderomotive force for the $m=1$ Laguerre profile from different angles.

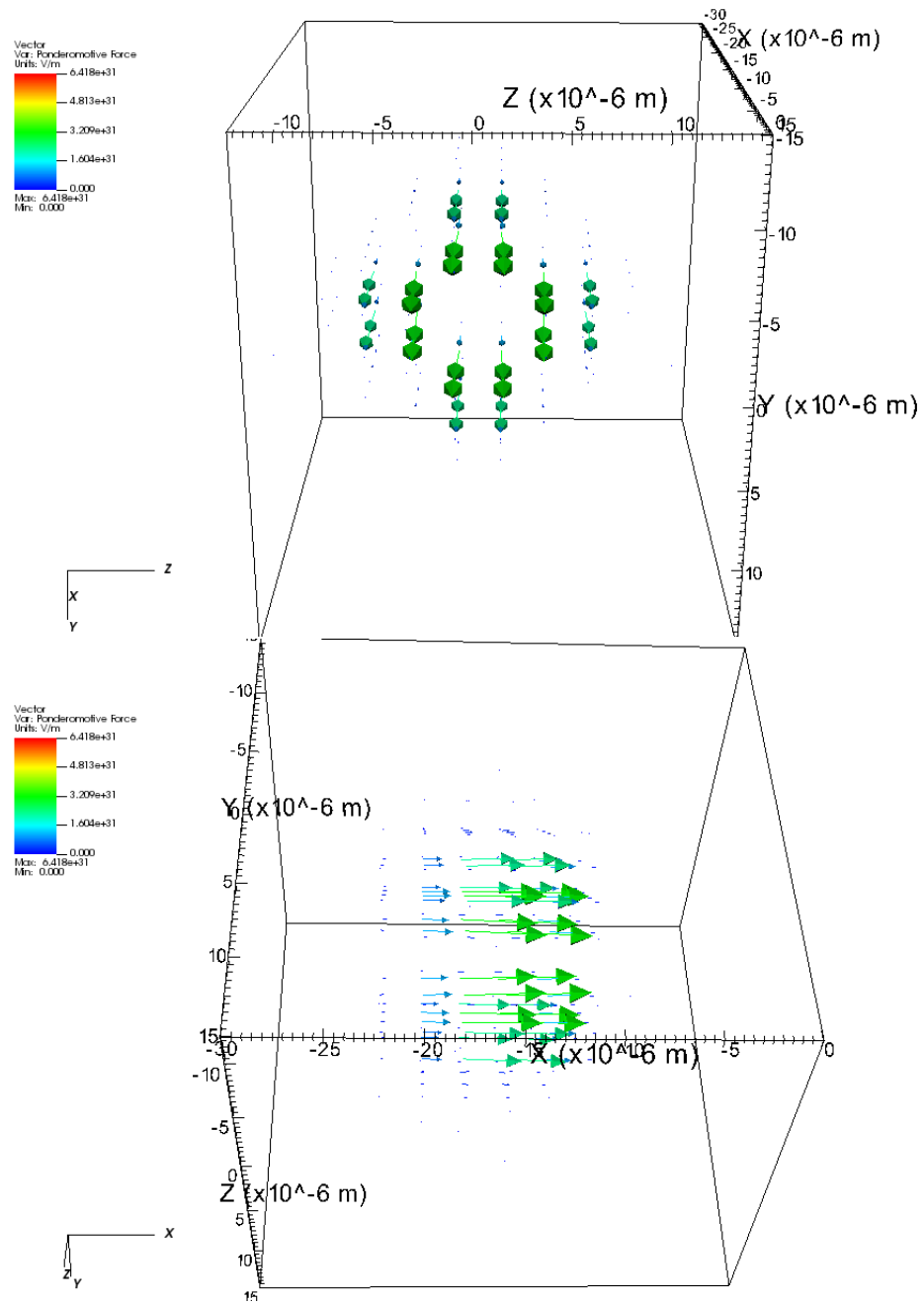


Figure 5.9: Vector plots showing the ponderomotive force for the $m=2$ Laguerre profile from different angles.

5.2 Higher intensity laser simulations

In the second set of simulations, we aimed to have laser intensities of the order of 10^{22} W/cm^2 . In order to do this, changes in the simulations parameters have to be made (The laser shape spreads transversally with increases in electric field amplitude, so the domain size must be changed, which in turn requires the reevaluation of the grid discretization). We settled for a $\lambda = 0.8 \mu\text{m}$, $a_0 = 70$, and $w_0 = 7\lambda$ laser ($I = 1.082 \times 10^{22} \text{ W/cm}^2$). The domain was taken to be $100\lambda \times 50\lambda \times 50\lambda$, with a grid of $1000 \times 250 \times 250$. This time around we only look at the regular Gauss profile and the first Laguerre mode ($m=1$). We aim again to compare the effects of the two profiles and see the differences that arise with the increase in intensity. The methods used for analysis are similar to those in the previous section. The input.deck file for the EPOCH simulation is also made available in the Appendix.

In figure 5.10 we show the density of electrons for the two simulations in order to visualize the plasma wave pattern formed. We can clearly see the formation of beams as well as the bubbles in front and behind it. This time, the bubble is clearly depleted. We can see also that the pattern repeats itself, there being a secondary bunch of electrons behind the second bubble and so on. This is a well known occurrence. However, only the first bunch of electrons is well accelerated, being both dense and energetic. This time around, the Laguerre-Gauss mode also forms one coherent accelerated beam of electrons instead of multiple ones. This is also visible in figure 5.11, where we look at the energy density to see better the shape and structure of the electron bunches. We can see that the Laguerre generated beam has a kind of doughnut shape, compared to the Gauss generated one, which has more flat transversal sections. In order to understand better the difference in shapes, we indicate figures 5.12 and 5.13. They show the electric field magnitude in two manners, illustrating the shape of the laser profiles. We can again see the separation of two clear structures in the Laguerre-Gauss beam, which this time around is not large enough to make the structures act independently, but causes the doughnut shape of the electron beam. The disturbances seen at the tail of the laser bumps are in the electron bunch region, and reflect the electric fields generated by high densities of electrons. We also plotted the ponderomotive force for the Laguerre mode figure 5.14 for visual comparison with the previous simulation.

	Maximum Value of Electron Energy Density	
	Gauss $m=0$	Laguerre $m=1$
Simulation Time (fs)	Energy Value (10^{18} J/m^3)	Energy Value (10^{18} J/m^3)
150	1.47	1.59
180	2.67	3.04
210	2.65	2.35
240	3.68	2.05
270	3.53	1.83
300	2.70	2.00

Table 5.2: A table with the maximum value of electron energy density at different time steps.

Finally, we again make use of the values of electron energy density to compare acceleration efficiency. Due to the changes in initial parameters and the reduction in the simulation duration (for run time reduction), we can not see the entirety of the two acceleration for both profiles, but we catch the region around the peak for both. We therefore show in section 5.2 simultaneous

values. The main observation is that this time around the order of magnitude is the same, which suggest the by using Laguerre-Gauss modes at high intensities should not affect the acceleration efficiency substantially.

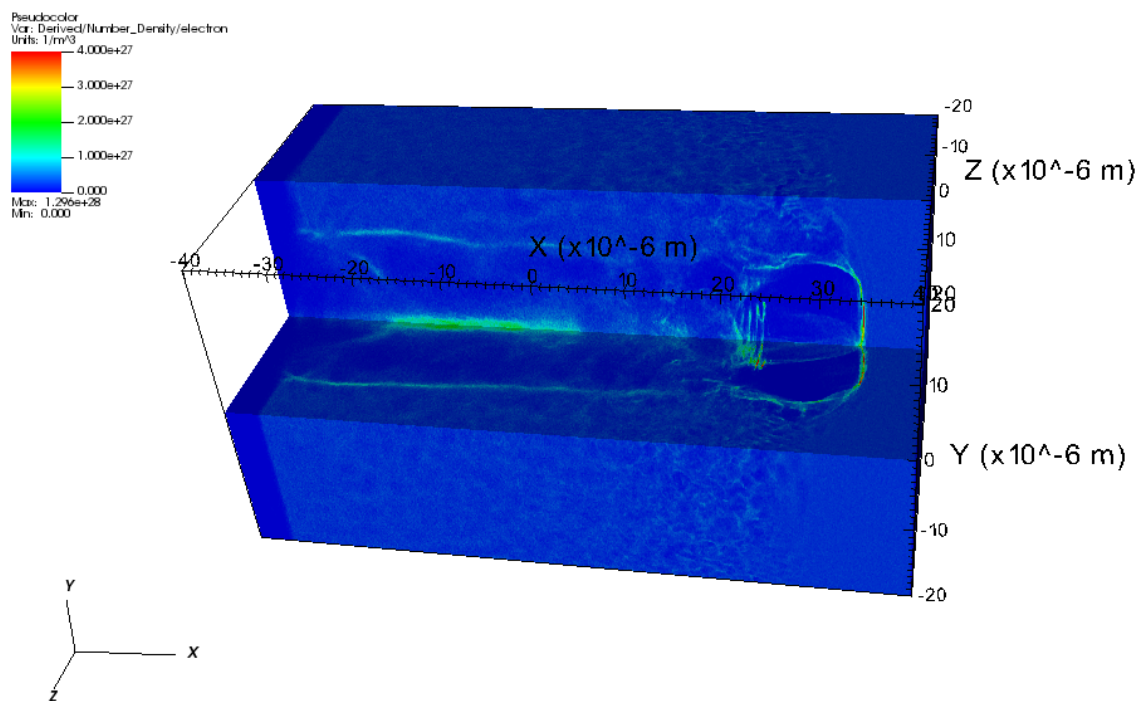
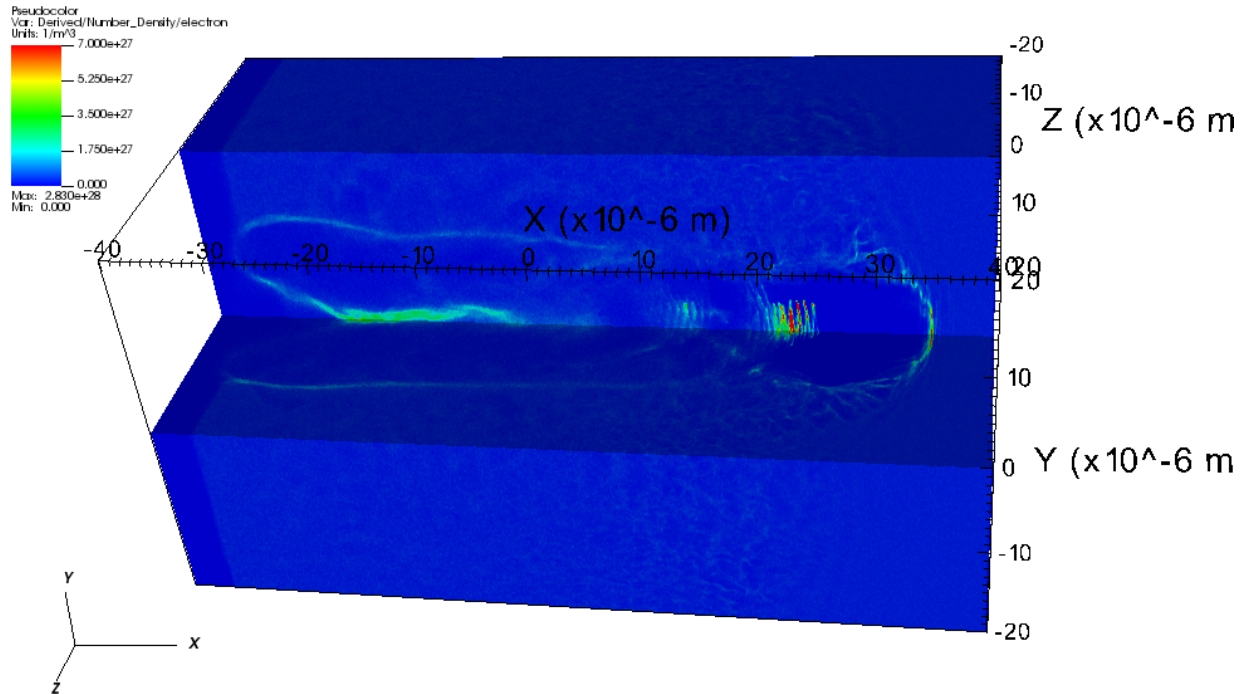
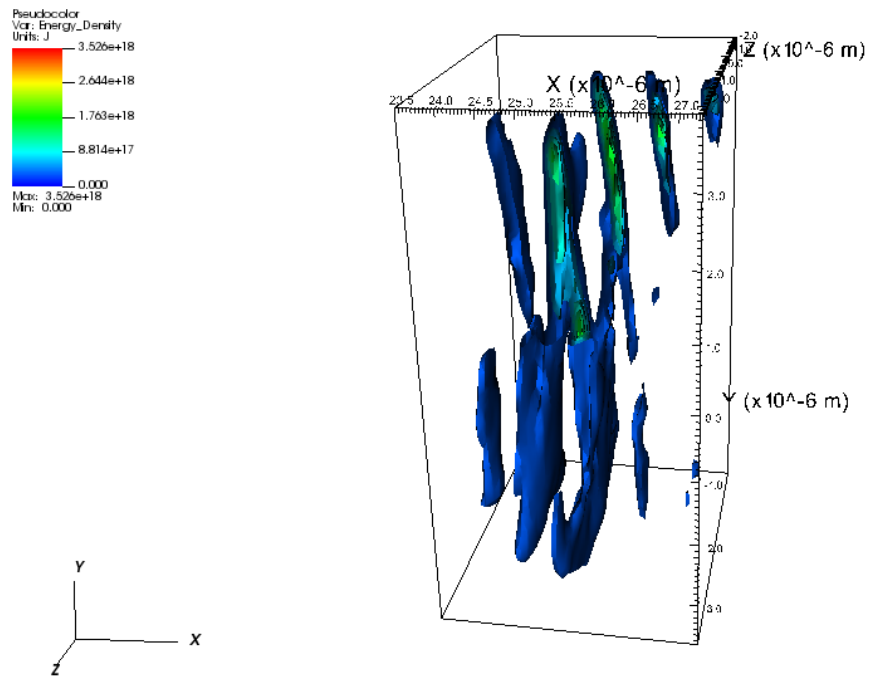


Figure 5.10: Plots of the number density of electrons across the entire simulation domain at 255 fs into the run: top - Gauss, Bottom - Laguerre. The upper limit of the color bar was set below the actual maximum value in the data in order to emphasize the low density fluctuations for visual clarity.



DB: 0018.sdf
Cycle: 1305 Time: 2.70121e-13

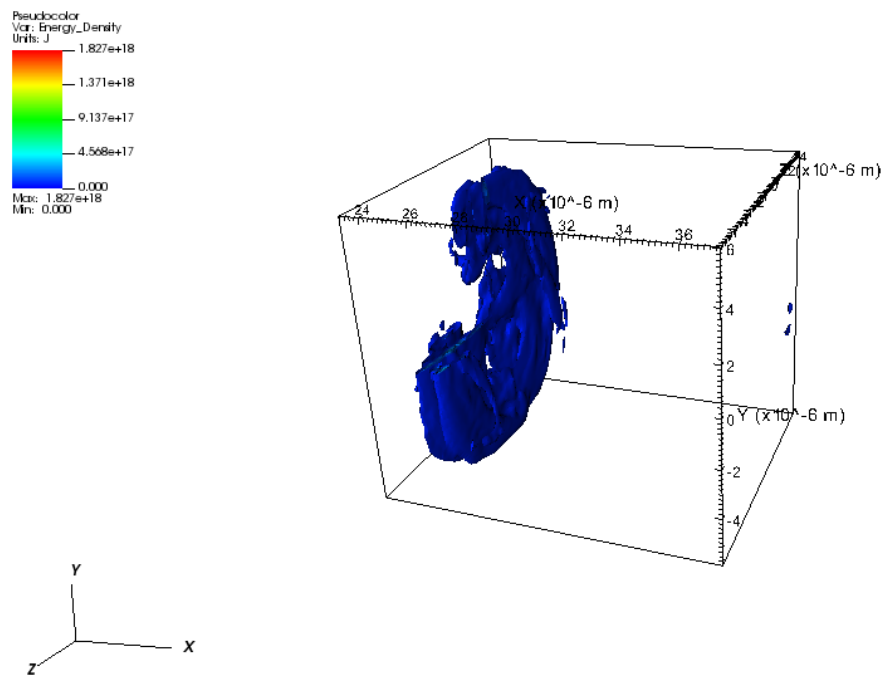


Figure 5.11: Pseudocolor plots of isosurfaces of the electron energy density at 270 fs into the run: top - Gauss, Bottom - Laguerre.

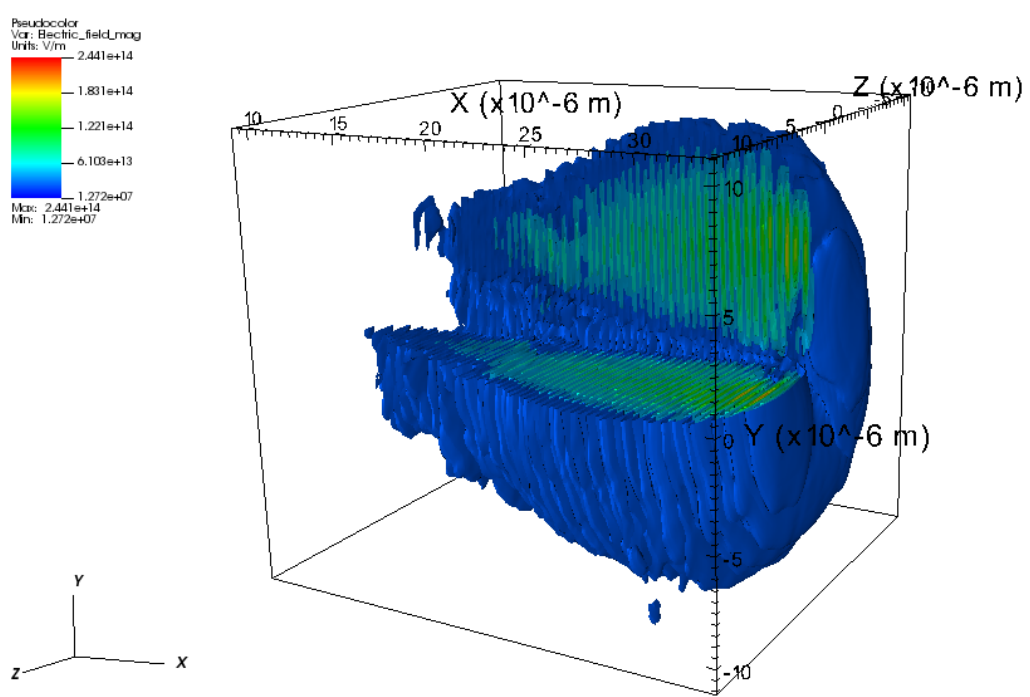
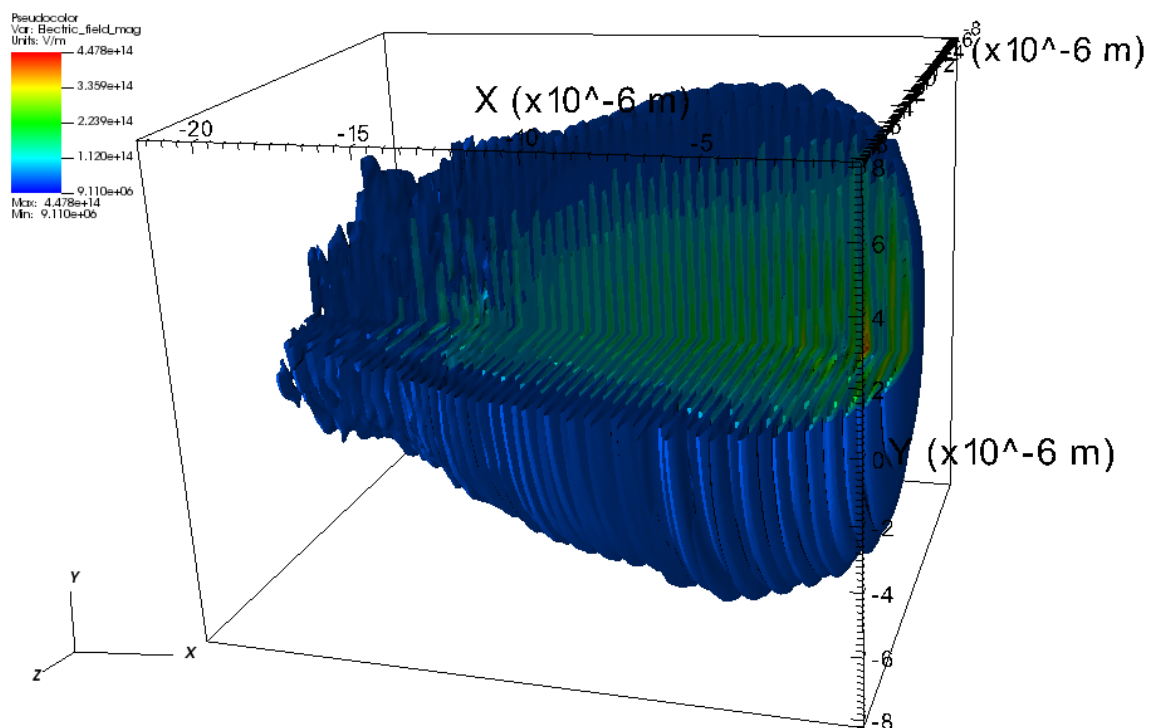


Figure 5.12: Plots of isosurfaces of the the electric field magnitude: top - Gauss, Bottom - Laguerre.

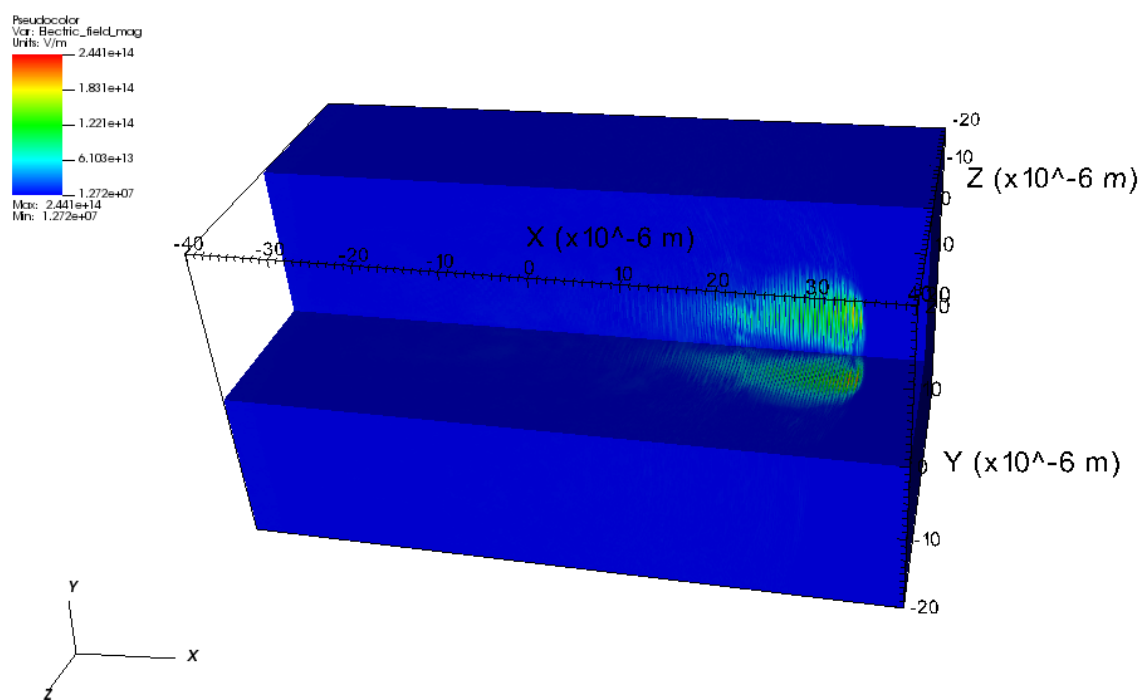
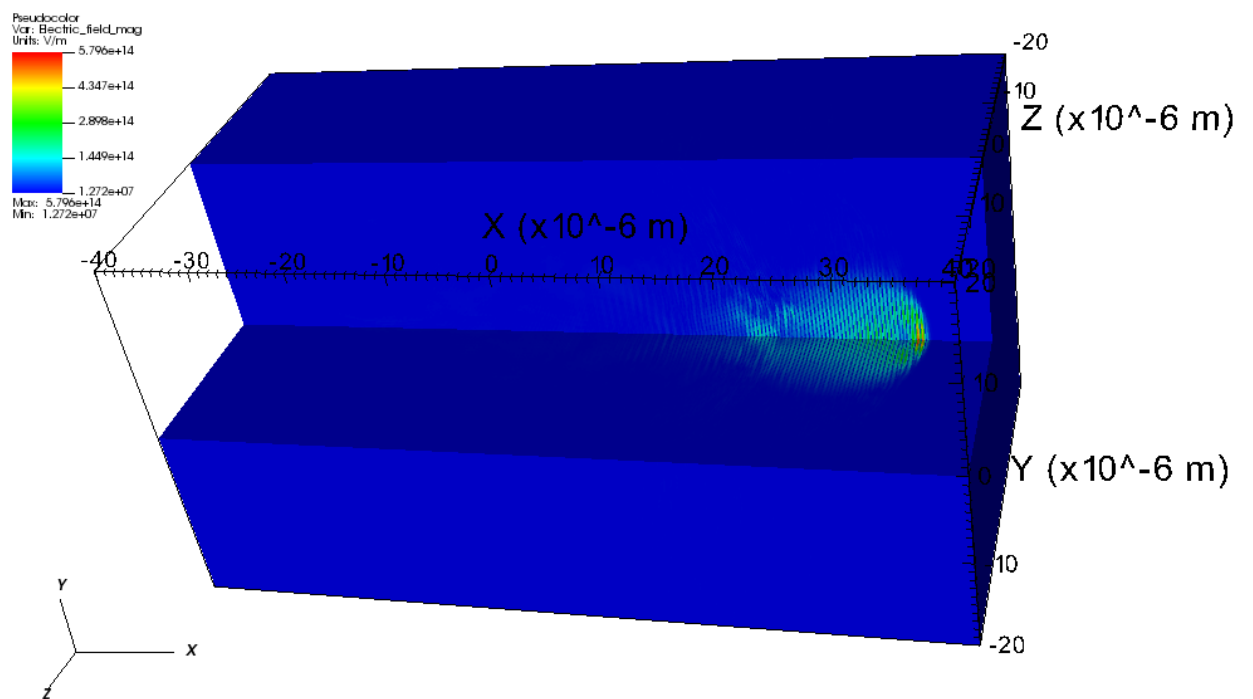


Figure 5.13: Plots of the the electric field magnitude in the volume: top - Gauss, Bottom - Laguerre.

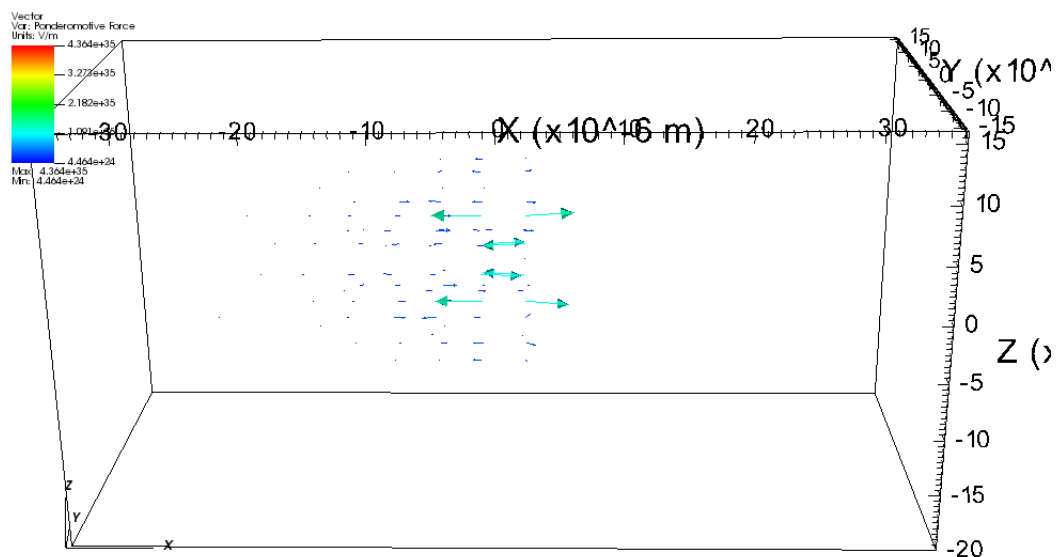
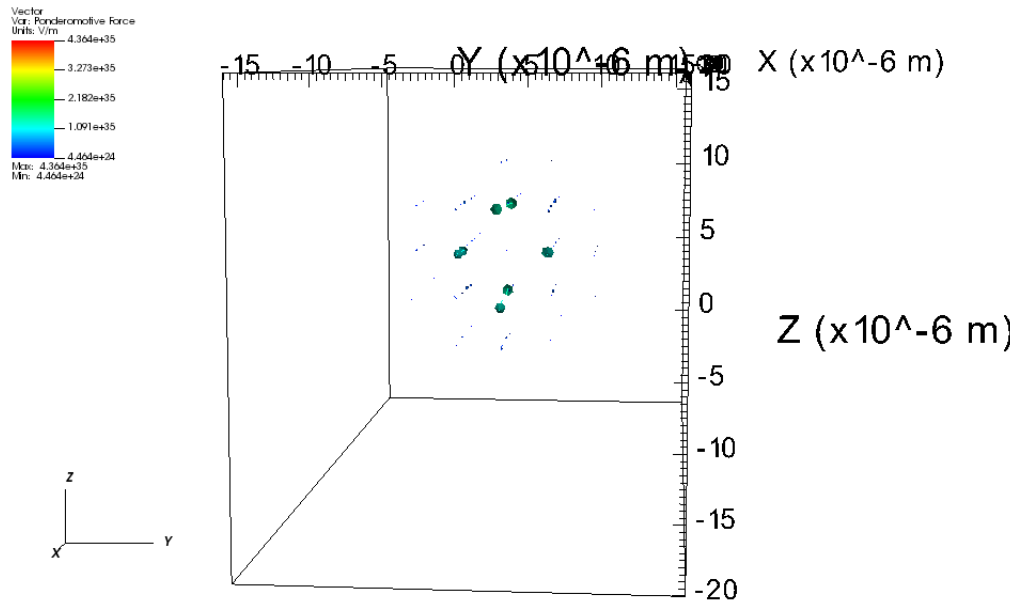


Figure 5.14: Vector plots showing the ponderomotive force for the $m=1$ Laguerre profile from different angles.

5.3 Structured targets

This study surrounds certain aspects of the production of gamma -beams using the interaction between a laser pulse and a plasma medium with a predesigned structure. To be more specific, we simulate the passage of a simple Gaussian pulse through a pipe-like overdense carbon plasma structure using a Particle-in-Cell code (EPOCH). The plasma pipe consists of a cylindrical bulk region, with the density $100 n_{crit}$, surrounding a cylindrical channel, with the density $20 n_{crit}$ (see figure 5.15). The channel diameter is comparable with the laser beam waist radius, such that most of the energy transferred from it to the plasma goes into the channel region. The propagation of the laser through the channel drives a longitudinal electron current (see figure 5.18), which in turn generates and sustains a quasistatic azimuthal magnetic field. By deflecting the highly energetic electrons, this field induces the production of synchrotron photons. The result is a gamma-beam with a relatively small divergence. For more details related to this see the article by T. Wang *et al.* 2020, which is the one that lead us to doing this study. This type of technique has the advantage of being easier to implement experimentally than the change in laser profile used in the previous two sections.

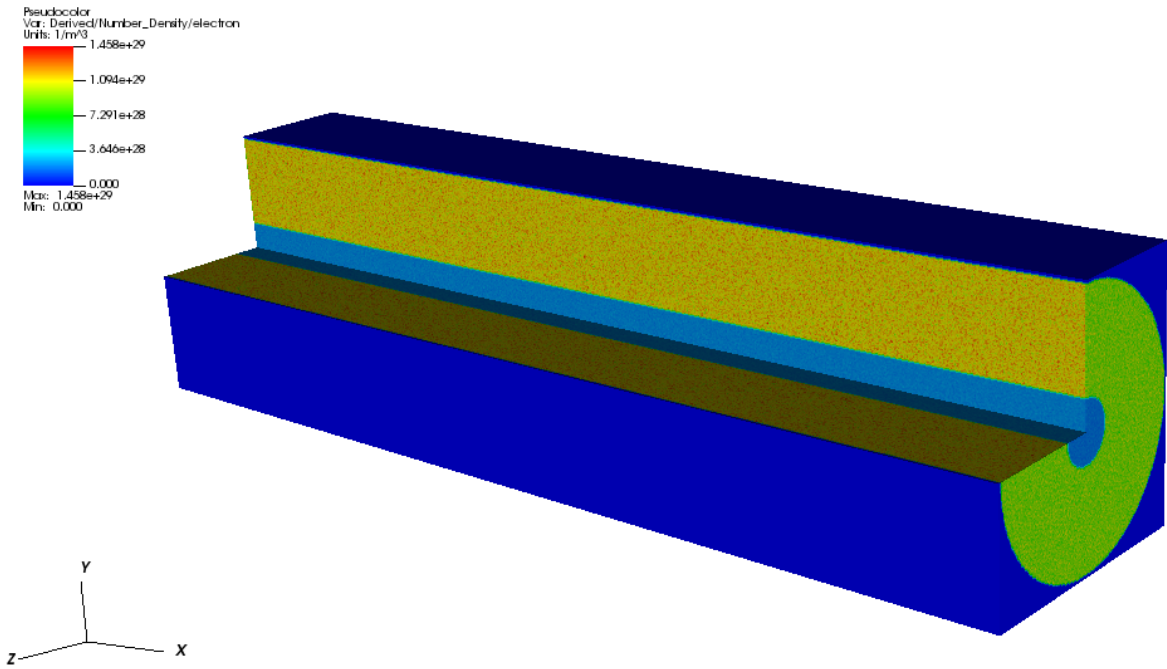


Figure 5.15: A plot of the electron number density at the beginning of the simulation showcasing the structure of the carbon plasma used for the numerical experiments.

We aim to study the variation of the gamma yield with the change in the internal radius of the pipe (*i.e.* the channel radius), while keeping the external radius fixed. For the parametrization of the laser we chose the defining parameters to be: $a_0 = 190$, $\lambda_0 = 1 \mu\text{m}$, which lead to a peak intensity of $5 \times 10^{22} \text{ W/ cm}^2$. We remark that this value of laser peak intensity is in general relevant for the new Petawatt laser infrastructures around the world. We also chose the beam waist radius to be $w_0 = 1.3 \mu\text{m}$, which sets the power of our laser to 1 PW. The laser was focalized at $x = 0.0$ and the pulse duration was 35 fs. The exterior radius of the pipe was fixed to $4 \mu\text{m}$, while the interior radius was given the values: $0.5w_0$, $0.7w_0$, $1.0w_0$, and

$1.2w_0$. The total length of the pipe was set to $33 \mu\text{m}$ and the total simulation time was chosen to be 110 fs. In all simulations the plasma was initialized as being fully ionized, since studies in the literature suggest that at the intensity and the power we work with the initially neutral medium would become fully ionized almost instantly. For the grid, we used a distretization of $30/\mu\text{m}$ in all three spatial directions. Since we are only interested to look at the energy of the produced photons, we have set them in the simulation to not propagate in time (that is, after they are produced, they are registered and not used further in the simulation), thus reducing greatly the simulation time. The average simulation time was 26 hours. An example input.deck is again available in the Appendix, this time together with a short indication on how to enable the QED effects in EPOCH.

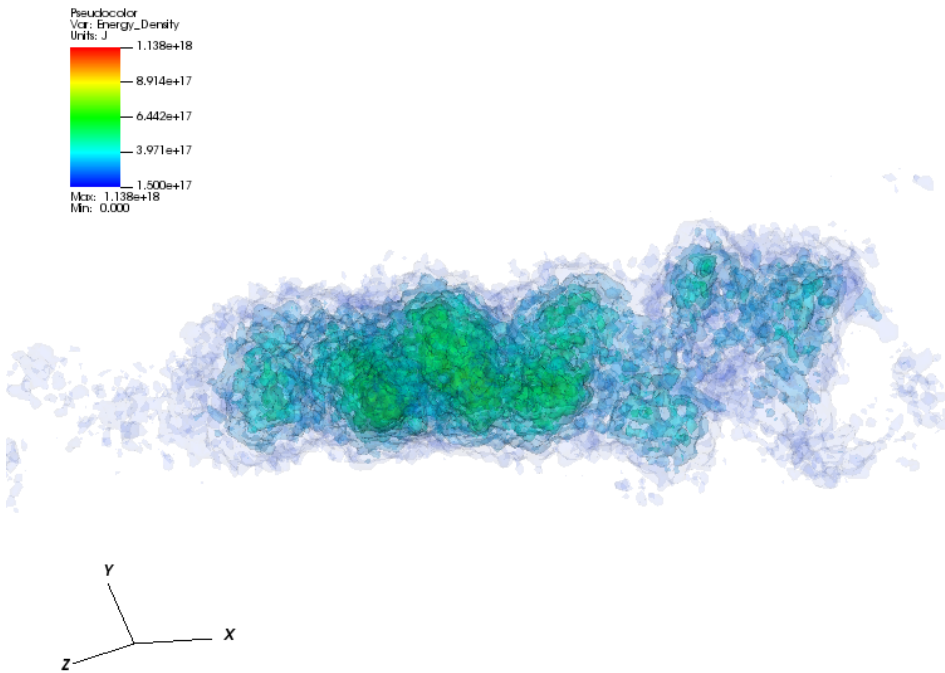


Figure 5.16: A plot of the electron energy density (average electron energy multiplied by the number density) that showcases the electron current generated in the channel.

In figure 5.17 we show the energy distribution in volume of the photon energy for the photons generated up to 100 fs into the simulation. By analyzing the data, we find that photons are generated, as expected, predominantly inside the channel region. From the transversal section we can observe better the internal structure of the photon bulk. We can clearly see that it hints towards the spherical projections given in ?? on page 3.

In order to compare the photon production as a function of channel radius, we look at the average particle energy per grid cell. We count all the cells that contain an average energy larger than a certain lower limit. The results are shown in figure 5.19. In this plot, by efficiency we actually mean the number of grid cell with average energy above a ceratain value divided by the total number of grid cells that contain non-zero values of photon energy. This is used as a way to estimate the fraction of photons above certain energies from the total number of photons produced in the simulation. We can see that both graphs show an increase with the increase of the channel radius. This trend is more pronounced in the low energy samples. We also note that the cuves are concave, which suggests that further increase of the channel radius will not

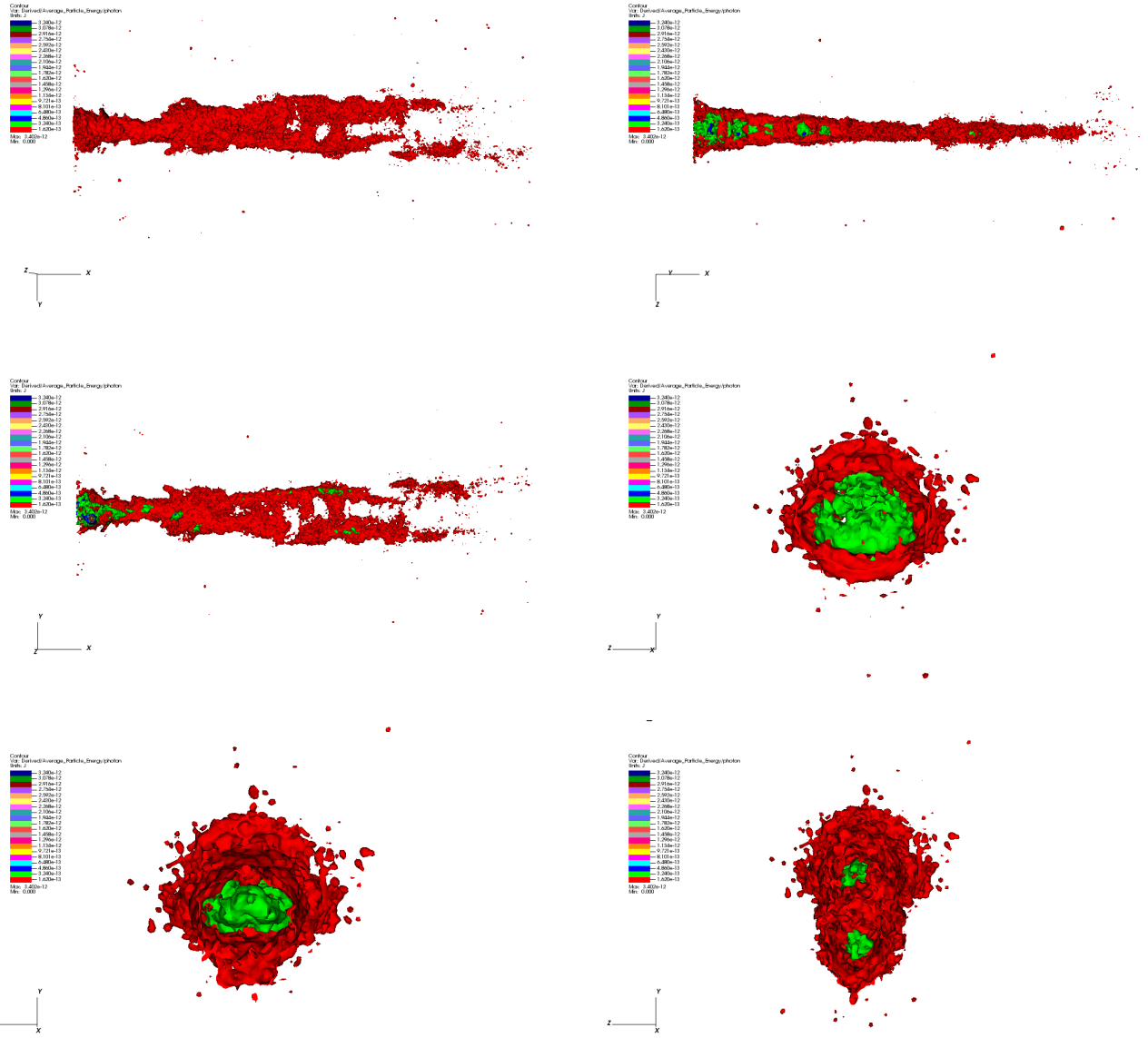


Figure 5.17: A series of contour plots of the average photon energy showcasing all the photons produced up to 100fs into the simulation. Different plots show different clips of the photon bulk. They are displayed in the following order: top left - uncut view; top right - cut through the middle in the x-z plane; middle left - cut through the middle in the x-y plane; middle right - transversal cut 1 μm in from the entry plane of the laser; bottom left - - transversal cut 3 μm in from the entry plane of the laser.

continue to increase the synchrotron photon yield. This is expected, since further increase in the radius would make the channel much thicker than the laser beam.

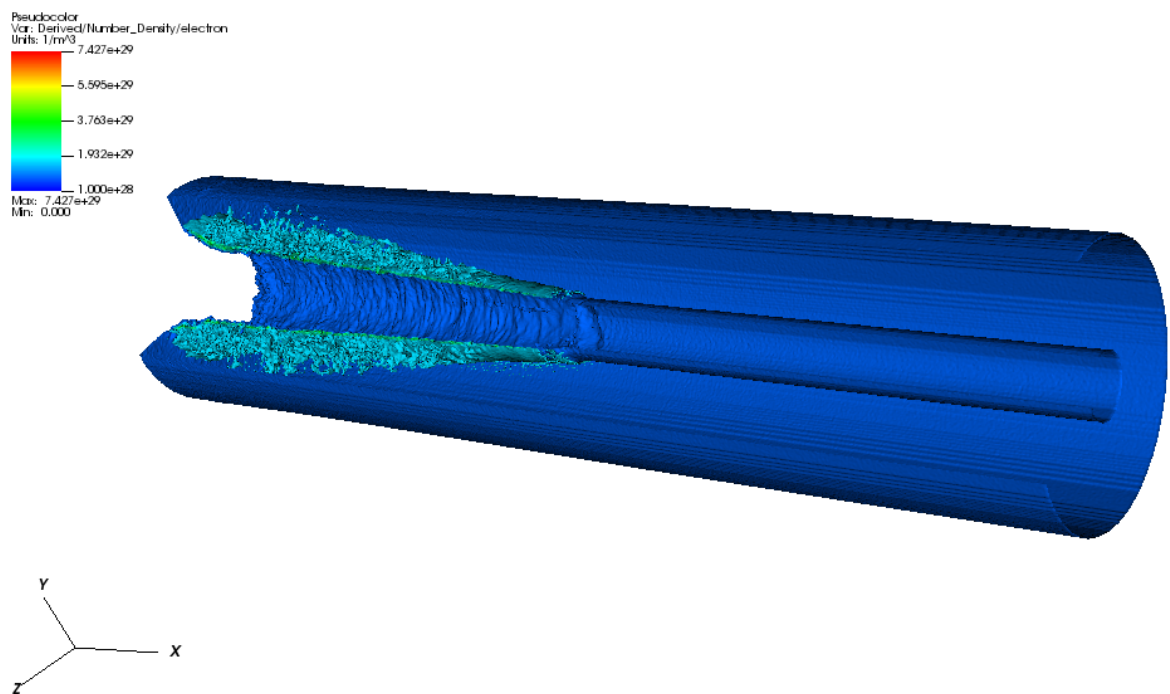


Figure 5.18: A plot of the electron number density 100 fs into the simulation that showcases how the passage of the laser through the plasma affects the structure of our plasma pipe. Some channel electrons spread inside the bulk region.

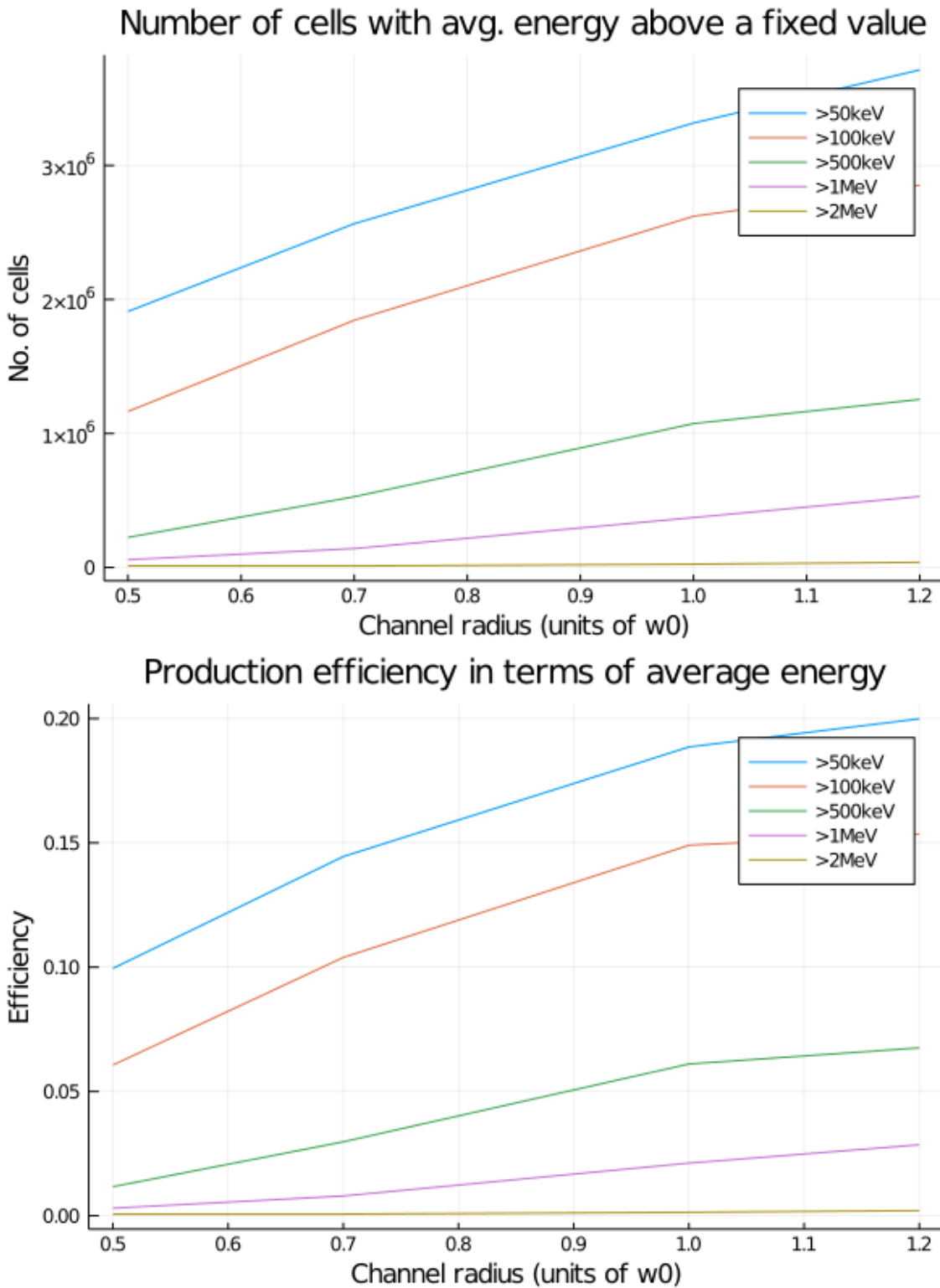


Figure 5.19: Plots comparing the production yield of different photon energies in terms of the channel radius. Top: the number of cells with average photon energy above 50 keV, 100 keV, 500 keV, 1 Mev, and 2 MeV, respectively. Bottom: the production efficiency for different energies above the same lower limits as in the previous plot.

Chapter 6

Conclusions

To sum everything up, this thesis tackled a part of the field of high-intensity laser-plasma interaction, which is one of great interest nowadays given the new high power laser infrastructures that have been constructed in the past couple of years under the ELI project. We have introduced the required theoretical considerations together with examples and throughout calculations. After explaining the formalism used in describing laser beams, the properties that make plasma the perfect candidate for the applications we want to study, and the inner working of the numerical method used, we presented the original results obtained regarding two applications of great importance from both theoretical and experimental physics: laser wakefield acceleration and the use of structured targets to obtain γ -rays. We have found that at low intensities, in a laser wakefield accelerator, we can obtain multiple beams distributed in a controllable pattern by using Laguerre-Gauss modes. The number of beams is found to be equal to twice the order of the mode (the m number), the cost being a reduction in the maximum energy of the accelerated electron beam of about one order of magnitude. We have also made use of the quantum electrodynamics effects that are available in the PIC code (EPOCH) in order to study the generation of high-energy γ -beams by passage of a high-intensity laser through a structured plasma target shaped like a pipe. We have found that if we keep the exterior radius of the pipe fixed and vary the inside radius, the photon yield increases with the increase in internal radius up to a certain threshold. This suggests that this is a valid direction in the search for optimizing such technology. The data suggests that the optimal radius should be close to the waist radius of the laser beam.

Appendix

Small Simulation of Electron Dynamics in a Laser Pulse

```
using Plots

x(t; c, a0, ω) = c*a0/ω*(cos(ω*t)-1)
z(t; c, a0, ω) = c*a02/4*(t - sin(2*ω*t)/(2*ω))

function plot_electron_motion(c, a0, ω)
    kwargs = (c = c, a0 = a0, ω = ω)

    t = 0:(2*6.14/ω)/1000:(2*6.14/ω)
    plot(z.(t; kwargs...), x.(t; kwargs...), xlabel="z", ylabel="x", legend=false)
end

plot_electron_motion(c, a0, ω)

savefig("relativistic_electron_cont_pulse.png")

function plot_electron_finite_pulse(c, a0, ω, τ0)
    a(τ; a0, τ0, ω) = a0*exp(-(τ/τ0)2)*sin(ω*τ)
    kwargs = (a0 = a0, τ0 = τ0, ω = ω)
    τ = 0
    dτ = 6.14/ω/1000
    x = 0
    z = 0
    trans = []
    long = []
    for t in τ:dτ:5*τ0
        push!(trans, x)
        push!(long, z)
        x = x + c*a(t; kwargs...)*dτ
        z = z + c*a(t; kwargs...)*a(t; kwargs...)*dτ/2
    end
    plot(long, trans, xlabel="z", ylabel="x", legend=false)
end

c = 3*108
a0 = 20
ω = 2*3.14*4*1014
τ0 = 30*10-15

plot_electron_finite_pulse(c, a0, ω, τ0)
savefig("relativistic_electron_short_pulse.png")
```

Implementation of a Few Integrators for the Harmonic Oscillator for the Visualization of Stability

```
using Plots

# equation: dv/dt = -x; dx/dt = v

# explicit Euler
function Exp_Euler(N, Δt, icond)
    x = [icond[1]]
    v = [icond[2]]
    for i in 1:convert(Int64, N/Δt)
        push!(x, x[i] + v[i]*Δt)
        push!(v, v[i] - x[i]*Δt)
    end
    return [x, v]
end

# implicit Euler
function Imp_Euler(N, Δt, icond)
    x = [icond[1]]
    v = [icond[2]]
    for i in 1:convert(Int64, N/Δt)
        push!(x, (x[i] + v[i]*Δt)/(1 + Δt^2))
        push!(v, (v[i] - x[i]*Δt)/(1 + Δt^2))
    end
    return [x, v]
end

# semi-implicit Euler
function SImp_Euler(N, Δt, icond)
    x = [icond[1]]
    v = [icond[2]]
    for i in 1:convert(Int64, N/Δt)
        push!(v, v[i] - x[i]*Δt)
        push!(x, x[i] + v[i+1]*Δt)
    end
    return [x, v]
end

# trapezoid rule
function Trapezoid(N, Δt, icond)
    x = [icond[1]]
    v = [icond[2]]
    for i in 1:convert(Int64, N/Δt)
        push!(x, (x[i]*(1 - Δt^2/4) + v[i]*Δt)/(1 + Δt^2/4))
        push!(v, (v[i]*(1 - Δt^2/4) - x[i]*Δt)/(1 + Δt^2/4))
    end
    return [x, v]
end

# Störmer-Verlet method
function St_Ver(N, Δt, icond)
    x = [icond[1]]
    v = [icond[2]]
    for i in 1:convert(Int64, N/Δt)
        v1half = v[i] - x[i]*Δt/2
        push!(x, x[i] + v1half*Δt)
        push!(v, v1half - x[i+1]*Δt/2)
    end
    return [x, v]
end

function make_plots()
    # explicit Euler solution
    sol1 = Exp_Euler(N, Δt, icond)
    p1 = plot(sol1[1], sol1[2], seriestype = :scatter, title = "Explicit Euler")

    # implicit Euler solution
```

```

sol2 = Imp_Euler(N, Δt, icond)
p2 = plot(sol2[1], sol2[2], seriestype = :scatter, title = "Implicit Euler")

# semi-implicit Euler solution
sol3 = SImp_Euler(N, Δt, icond)
p3 = plot(sol3[1], sol3[2], seriestype = :scatter,
title = "Semi-implicit Euler")

# trapezoid solution
sol4 = Trapezoid(N, Δt, icond)
p4 = plot(sol4[1], sol4[2], seriestype = :scatter, title = "Trapezoid")

# Störmer-Verlet solution
sol5 = St_Ver(N, Δt, icond)
p5 = plot(sol5[1], sol5[2], seriestype = :scatter, title = "Störmer-Verlet")

# real solution
solrx = [sin(x) for x in 0:Δt:N]
solrv = [cos(x) for x in 0:Δt:N]
pr = plot(solrx, solrv, seriestype = :scatter, title = "Analytic solution")

l = @layout [a b c; d e f]
plot(pr,p1,p2,p3,p4,p5, layout = l, xticks = -2:2, xlims = (-2.5,2.5),
ylims = (-2.5,2.5), xlabel = "x", ylabel = "v", legend = false)
plot!(size = (750,500))
end

# initial conditions
icond = [0.0,1.0]
# number of periods and time-step
N = 15
Δt = 0.3

p = make_plots()
png(p, "stability_plots2")

```

EPOCH input.deck for low intensity simulations (m=1, p=0)

```

begin:constant
lambda0 = 1.0 * micron
temp = 0.0
a0 = 2 #normalized vector potential
dens = critical(2 * pi * c / lambda0) / 1000 #approx 1.0e24, ncrit=1.11*10^27
r = sqrt(y^2 + z^2)
phi = atan2(y,z)
w_0 = 5 * micron
m = 1
p = 0
Cpm = 1 #sqrt(p!/(m+p)!)
end:constant

begin:control
nx = 1200
ny = 300
nz = 300

# final time of simulation
t_end = 400 * femto

```

```

# size of domain
x_min = -30.0 * lambda0
x_max = -x_min
y_min = -15.0 * lambda0
y_max = -y_min
z_min = y_min
z_max = -z_min

stdout_frequency = 60
end:control

begin:boundaries
  bc_x_min = simple_laser
  bc_x_max = simple_outflow
  bc_y_min = periodic
  bc_y_max = periodic
  bc_z_min = periodic
  bc_z_max = periodic
end:boundaries

begin:laser
  boundary = x_min
  lambda = lambda0
  amp = a0 / lambda0 * 2 * pi * me*c^2/qe # E0
  profile = Cpm * (sqrt(2)*r/w_0)^m * gauss(r,0,w_0) * cos(m*phi)
  #t_start = 0.0
  #t_end = 17.0 * femto
  t_profile = gauss(time,34*femto,17*femto)
end:laser

begin:species
  name = electron
  charge = -1.0
  mass = 1.0
  #frac = 1.0
  temp = 0
  density = dens
  npart_per_cell = 5
end:species

begin:species
  #He ions
  name = ions
  charge = 2.0
  mass = 4.0 * 1830
  npart_per_cell = 2
  immobile = T
  density = 0.5 * dens

```

```

    temp = 0.0
end:species

begin:window
    move_window = T
    window_v_x = c
    #when pulse is centered in window
    window_start_time = (x_max - x_min)/c
    bc_x_min_after_move = simple_outflow
    bc_x_max_after_move = simple_outflow
end:window

begin:output
    #timesteps between output dumps
    dt_snapshot = 10.0 * femto

    # Properties on grid
    grid = always
    ex = always
    ey = always
    ez = always

    # Properties at particle positions
    particle_grid = always

    number_density = always + species
    charge_density = always + species
    average_particle_energy = always + species
end:output

```

EPOCH input.deck for higher intensity simulations (m=1, p=0)

```

begin:control
    nx = 1000
    ny = 250
    nz = 250

    # Final time of simulation
    t_end = 350 * femto

    # Size of domain
    x_min = -50 * 800 * nano
    x_max = -x_min
    y_min = -25 * 800 * nano
    y_max = -y_min
    z_min = y_min

```

```

z_max = -z_min

stdout_frequency = 60
end:control

begin:boundaries
  bc_x_min = simple_laser
  bc_x_max = open
  bc_y_min = periodic
  bc_y_max = periodic
  bc_z_min = periodic
  bc_z_max = periodic
end:boundaries

begin:constant
  lambda0 = 800 * nano
  omega = 2 * pi * c / lambda0
  T_1 = lambda0 / c

  a0 = 70
  w_0 = 7 * lambda0 # Beam waist size
  r = sqrt(y^2 + z^2)
  phi = atan2(y,z)

  m = 1
  p = 0
  Cpm = 1 #sqrt(p!/(m+p)!)
  n = 2.4e26
end:constant

begin:laser
  boundary = x_min
  lambda = lambda0
  amp = a0 / lambda0 * 2 * pi * me*c^2/qe # E0
  phase = m*phi
  profile = Cpm * (sqrt(2)*r/w_0)^m * gauss(r,0,w_0)
  t_profile = gauss(time, 0.0, 20*T_1)
end:laser

begin:species
  name = electron
  charge = -1.0
  mass = 1.0
  number_density = if((-45*lambda0 lt x) and (x lt 50*lambda0), n, 0.0)
  temperature_ev = 1e3

```

```

nparticles_per_cell = 4
end:species

begin:species
  name = helium
  charge = 2.0
  mass = 7296.3
  number_density = 0.5*number_density(electron)
  temperature_ev = 30
  nparticles_per_cell = 2
end:species

begin:output
  name = normal

  # Number of timesteps between output dumps
  dt_snapshot = 15 * femto

  # Properties on grid
  grid = always
  ex = always
  ey = always
  ez = always
  poynting_flux = always

  # Properties at particle positions
  particle_grid = always
  px = always
  py = always
  pz = always

  number_density = always + species
  average_particle_energy = always + species
  particle_energy_flux = always + species
end:output

```

Structured target

There is a short remark to be made. This input.deck uses QED effects. By default, all the QED effects in EPOCH are turned off from inside the code. So in order to use them, you will need to make changes to the makefile before compiling the EPOCH code. The documentation and other documents that mention this don't give you a clear explanation on how to do it without bothering to look at what is inside the makefile (at least at the moment of writing this - epoch-v4.17.10). For any reader who wants to just use the software with absolutely zero interaction with what is written in the makefile, just use the following linux commands

```

user@home:~# cd /$EPOCH_VERSION/epoch1d
user@home:~# sed -i 's/#DEFINES += $(D)PHOTONS/DEFINES += $(D)PHOTONS/g' Makefile
user@home:~# make clean

```

before compiling the code.

```

begin:constant
  #laser parameters
  lambda0 = 1.0 * micron
  a0 = 190
  w0 = 1.3 * micron #change it to change power

  #plasma parameters
  n_cr = critical(2 * pi *c / lambda0)
  n_bulk = 100 * n_cr
  n_ch = 20 * n_cr

  d_bulk = 3 * micron
  R_ch = 0.7 * w0
  L_ch = 33 * micron

  #general
  r = sqrt(y^2 + z^2)
  x0 = 0.0
end:constant

begin:control
  #grid
  nx = 990
  ny = 240
  nz = 240

  #simulation time
  t_end = 110 * femto

  #domain size

  x_min = 0.0
  x_max = L_ch
  y_min = - 4.0 * micron
  y_max = -y_min
  z_min = y_min
  z_max = -y_min

  stdout_frequency = 20
end:control

begin:boundaries
  bc_x_min = simple_laser

```

```

bc_x_max = simple_outflow
bc_y_min = periodic
bc_y_max = periodic
bc_z_min = periodic
bc_z_max = periodic
end:boundaries

begin:laser
boundary = x_min
lambda = lambda0
amp = a0 / lambda0 * 2 * pi * me*c^2/qe

profile = gauss(r, 0.0, w0)

t_profile = gauss(time, 0.0, 35*femto)
end:laser

begin:qed
use_qed = T
qed_start_time = 0
produce_photons = T
qed_table_location = /epoch-4.17.10/epoch3d/src/physics_packages/TABLES
end:qed

begin:species
#synchrotron photons
name = photon
nparticles = 0
dump = T
identify:photon
end:species

begin:species
#electrons
name = electron
# charge = -1.0
# mass = 1.0
temp = 0.0
dump = T
npart_per_cell = 15

number_density = if(r lt (R_ch + d_bulk), n_bulk, 0.0)
number_density = if(r lt R_ch, n_ch, number_density(electron))
number_density = if((x lt x0) and (x gt L_ch), 0.0, number_density(electron))

#for QED effects to work
identify:electron
end:species

```

```

begin:species
  #carbon ions
  name = carbon
  charge = 6.0
  mass = 12 * 1836.2
  temp = 0.0
  dump = T
  npart_per_cell = 5

  number_density = number_density(electron) / 6
end:species

begin:output
  #timesteps between output dumps
  dt_snapshot = 10.0 * femto

  # Properties on grid
  grid = always

  # Properties at particle positions
  particle_grid = always
  #px = always + species
  #py = always + species
  #pz = always + species
  #momenta and particle_energy are not defined for photons

  number_density = always + species
  average_particle_energy = always + species
end:output

```

Bibliography

- Tanaka, K. A. *et al.* (Mar. 1, 2020). “Current Status and Highlights of the ELI-NP Research Program”. In: *Matter and Radiation at Extremes* 5.2, p. 024402. ISSN: 2468-2047, 2468-080X. DOI: 10.1063/1.5093535. URL: <http://aip.scitation.org/doi/10.1063/1.5093535> (visited on 06/17/2020).
- Arber, T D *et al.* (Nov. 1, 2015). “Contemporary Particle-in-Cell Approach to Laser-Plasma Modelling”. In: *Plasma Physics and Controlled Fusion* 57.11, p. 113001. ISSN: 0741-3335, 1361-6587. DOI: 10.1088/0741-3335/57/11/113001. URL: <https://iopscience.iop.org/article/10.1088/0741-3335/57/11/113001> (visited on 05/02/2020).
- Jackson, John David (1999). *Classical Electrodynamics*. 3rd ed. New York: Wiley. 808 pp. ISBN: 978-0-471-30932-1.
- Fleisch, Daniel A. (2008). *A Student’s Guide to Maxwell’s Equations*. Cambridge, UK ; New York: Cambridge University Press. 134 pp. ISBN: 978-0-521-87761-9 978-0-521-70147-1.
- Weinberg, Steven (1972). *Gravitation and Cosmology: Principles and Applications of the General Theory of Relativity*. New York: Wiley. 657 pp. ISBN: 978-0-471-92567-5.
- Griffiths, David J. (1999). *Introduction to Electrodynamics*. 3rd ed. Upper Saddle River, N.J: Prentice Hall. 576 pp. ISBN: 978-0-13-805326-0.
- Heaviside, Oliver (1971). *Electromagnetic Theory: Including an Account of Heaviside’s Unpublished Notes for a Fourth Volume*. 3d ed. New York: Chelsea Pub. Co. 3 pp. ISBN: 978-0-8284-0237-8.
- Wang, Haifeng *et al.* (Aug. 2008). “Creation of a Needle of Longitudinally Polarized Light in Vacuum Using Binary Optics”. In: *Nature Photonics* 2.8, pp. 501–505. ISSN: 1749-4885, 1749-4893. DOI: 10.1038/nphoton.2008.127. URL: <http://www.nature.com/articles/nphoton.2008.127> (visited on 02/12/2020).
- Cicchitelli, Lorenzo, H. Hora, and R. Postle (Apr. 1, 1990). “Longitudinal Field Components for Laser Beams in Vacuum”. In: *Physical Review A* 41.7, pp. 3727–3732. ISSN: 1050-2947, 1094-1622. DOI: 10.1103/PhysRevA.41.3727. URL: <https://link.aps.org/doi/10.1103/PhysRevA.41.3727> (visited on 02/12/2020).
- Vrejoiu, C. (1987). *Electrodinamica și Teoria Relativității*. Universitatea din București, Facultatea de Fizică, Catedra de Fizică Teoretică și Matematică.
- Goldsmith, Paul F. (1998). *Quasioptical Systems: Gaussian Beam Quasioptical Propagation and Applications*. IEEE Press/Chapman & Hall Publishers Series on Microwave Technology and RF. Piscataway, NJ: IEEE Press. 412 pp. ISBN: 978-0-412-83940-5 978-0-7803-3439-7.
- Paschotta, R. (2020). “Article on ‘Gouy Phase Shift’ in the RP Photonics Encyclopedia”. In: (). URL: <https://www.rp-photonics.com> (visited on 02/17/2020).
- Dondera, Mihai (Jan. 3, 2020). “Electrons in Twisted Fields and Ponderomotive Effects”. In: *Journal of Physics B: Atomic, Molecular and Optical Physics*. ISSN: 0953-4075, 1361-6455. DOI: 10.1088/1361-6455/ab678e. URL: <https://iopscience.iop.org/article/10.1088/1361-6455/ab678e> (visited on 02/17/2020).

- Quesnel, Brice and Patrick Mora (Sept. 1, 1998). "Theory and Simulation of the Interaction of Ultraintense Laser Pulses with Electrons in Vacuum". In: *Physical Review E* 58.3, pp. 3719–3732. ISSN: 1063-651X, 1095-3787. DOI: 10.1103/PhysRevE.58.3719. URL: <https://link.aps.org/doi/10.1103/PhysRevE.58.3719> (visited on 02/15/2020).
- Abramowitz, Milton and Irene A. Stegun, eds. (2013). *Handbook of Mathematical Functions: With Formulas, Graphs, and Mathematical Tables*. 9. Dover print.; [Nachdr. der Ausg. von 1972]. Dover Books on Mathematics. New York, NY: Dover Publ. 1046 pp. ISBN: 978-0-486-61272-0.
- Bolze, Tom and Patrick Nuernberger (May 1, 2018). "Temporally Shaped Laguerre–Gaussian Femtosecond Laser Beams". In: *Applied Optics* 57.13, p. 3624. ISSN: 1559-128X, 2155-3165. DOI: 10.1364/AO.57.003624. URL: <https://www.osapublishing.org/abstract.cfm?URI=ao-57-13-3624> (visited on 03/12/2020).
- Sueda, K. et al. (2004). "Laguerre-Gaussian Beam Generated with a Multilevel Spiral Phase Plate for High Intensity Laser Pulses". In: *Optics Express* 12.15, p. 3548. ISSN: 1094-4087. DOI: 10.1364/OPEX.12.003548. URL: <https://www.osapublishing.org/oe/abstract.cfm?uri=oe-12-15-3548> (visited on 03/12/2020).
- Zeylikovich, I. et al. (July 15, 2007). "Ultrashort Laguerre-Gaussian Pulses with Angular and Group Velocity Dispersion Compensation". In: *Optics Letters* 32.14, p. 2025. ISSN: 0146-9592, 1539-4794. DOI: 10.1364/OL.32.002025. URL: <https://www.osapublishing.org/abstract.cfm?URI=ol-32-14-2025> (visited on 03/12/2020).
- S Simon, David (2016). *A Guided Tour of Light Beams: From Lasers to Optical Knots*. IOP Publishing. ISBN: 978-1-68174-437-7. DOI: 10.1088/978-1-6817-4437-7. URL: <http://iopscience.iop.org/book/978-1-6817-4437-7> (visited on 03/12/2020).
- Belinfante, F.J. (May 1940). "On the Current and the Density of the Electric Charge, the Energy, the Linear Momentum and the Angular Momentum of Arbitrary Fields". In: *Physica* 7.5, pp. 449–474. ISSN: 00318914. DOI: 10.1016/S0031-8914(40)90091-X. URL: <https://linkinghub.elsevier.com/retrieve/pii/S003189144090091X> (visited on 02/20/2020).
- Humblet, J. (July 1943). "Sur Le Moment d'impulsion d'une Onde Électromagnétique". In: *Physica* 10.7, pp. 585–603. ISSN: 00318914. DOI: 10.1016/S0031-8914(43)90626-3. URL: <https://linkinghub.elsevier.com/retrieve/pii/S0031891443906263> (visited on 02/20/2020).
- Karsch, Stefan (2018). *Applications of High Intensity Laser Pulse*. URL: https://www.physik.uni-muenchen.de/lehre/vorlesungen/sose_18/applications_of_high-intensity-laser-pulses/vorlesung/LaserMatter.pdf (visited on 02/16/2020).
- Mulser, Peter and Dieter Bauer (2010). *High Power Laser-Matter Interaction*. Springer Tracts in Modern Physics 238. Heidelberg ; New York: Springer. 416 pp. ISBN: 978-3-540-50669-0.
- Braithwaite, N St J (Nov. 1, 2000). "Introduction to Gas Discharges". In: *Plasma Sources Science and Technology* 9.4, pp. 517–527. ISSN: 0963-0252, 1361-6595. DOI: 10.1088/0963-0252/9/4/307. URL: <http://stacks.iop.org/0963-0252/9/i=4/a=307?key=crossref.59a30cfab96e90d9a38090818faa55f1> (visited on 02/25/2020).
- Arnold, V. I. (1997). *Mathematical Methods of Classical Mechanics*. 2nd ed. Graduate Texts in Mathematics 60. New York: Springer. 516 pp. ISBN: 978-0-387-96890-2.
- Feix, M. R. and Pierre Bertrand (Jan. 2005). "A Universal Model: The Vlasov Equation". In: *Transport Theory and Statistical Physics* 34.1-2, pp. 7–62. ISSN: 0041-1450, 1532-2424. DOI: 10.1080/00411450500253703. URL: <https://www.tandfonline.com/doi/full/10.1080/00411450500253703> (visited on 02/29/2020).
- Silim, I. and J. Büchner (2003). *Vlasov-Code Simulations of Collisionless Plasmas*. URL: <https://sites.ualberta.ca/~isilin/silin-gwdg.pdf> (visited on 02/29/2020).

- Basic Examples of Using EPOCH* (Feb. 7, 2020). URL: https://cfsa-pmw.warwick.ac.uk/mediawiki/index.php/EPOCH:Basic_examples (visited on 03/12/2020).
- Stix, Thomas Howard and Thomas Howard Stix (1992). *Waves in Plasmas*. New York: American Institute of Physics. 566 pp. ISBN: 978-0-88318-859-0 978-0-88318-858-3.
- Tajima, T. and J. M. Dawson (July 23, 1979). “Laser Electron Accelerator”. In: *Physical Review Letters* 43.4, pp. 267–270. ISSN: 0031-9007. DOI: 10.1103/PhysRevLett.43.267. URL: <https://link.aps.org/doi/10.1103/PhysRevLett.43.267> (visited on 03/01/2020).
- Mangles, Stuart (2020). *Introduction to Plasma Wakefield Acceleration*. URL: https://indico.cern.ch/event/758617/contributions/3146206/attachments/1751792/2838723/Wakefield_intro.pdf (visited on 03/01/2020).
- ONeil, AArion (2017). “Laser Wakefield Acceleration Simulations Using EPOCH”. Queen’s University Belfast. URL: https://pureadmin.qub.ac.uk/ws/portalfiles/portal/147720282/Aaron_O'Neill_40007530.pdf (visited on 03/01/2020).
- Leimkuhler, B. and Sebastian Reich (2004). *Simulating Hamiltonian Dynamics*. Cambridge Monographs on Applied and Computational Mathematics 14. Cambridge, UK ; New York: Cambridge University Press. 379 pp. ISBN: 978-0-521-77290-7.
- Butcher, J. C. (2008). *Numerical Methods for Ordinary Differential Equations*. 2nd ed. Chichester, England ; Hoboken, NJ: Wiley. 463 pp. ISBN: 978-0-470-72335-7.
- Liu, Eric (2020). “Conditioning and Numerical Stability”. URL: https://web.mit.edu/ehliu/Public/Yelp/conditioning_and_precision.pdf (visited on 04/13/2020).
- Birdsall, Charles K. and A. Bruce Langdon (1995). *Plasma Physics via Computer Simulation*. Repr. Plasma Physics Series. Bristol: Institute of Physics Publ. 479 pp. ISBN: 978-0-7503-0117-6.
- Liu, C. S., V. K. Tripathi, and Bengt Eliasson (Oct. 1, 2020). *High-Power Laser-Plasma Interaction*: 1st ed. Cambridge University Press. ISBN: 978-1-108-48063-5 978-1-108-63584-4. DOI: 10.1017/9781108635844. URL: <https://www.cambridge.org/core/product/identifier/9781108635844/type/book> (visited on 04/08/2020).
- Silin, Ilya (2020). *Vlasov-Code Simulations of Collisionless Plasma*. URL: <https://sites.ualberta.ca/~isilin/silin-gwdg.pdf> (visited on 04/08/2020).
- Bertrand, Pierre et al. (Jan. 2005). “Vlasov Models for Laser-Plasma Interaction”. In: *Transport Theory and Statistical Physics* 34.1-2, pp. 103–126. ISSN: 0041-1450, 1532-2424. DOI: 10.1080/00411450500255310. URL: <https://www.tandfonline.com/doi/full/10.1080/00411450500255310> (visited on 04/08/2020).
- Buneman, O (June 1967). “Time-Reversible Difference Procedures”. In: *Journal of Computational Physics* 1.4, pp. 517–535. ISSN: 00219991. DOI: 10.1016/0021-9991(67)90056-3. URL: <https://linkinghub.elsevier.com/retrieve/pii/0021999167900563> (visited on 04/13/2020).
- Boris, Jay P. (1970). “Relativistic Plasma Simulation—Optimization of a Hybrid Code”. In: Fourth Conference on Numerical Simulations of Plasmas. Naval Research Laboratory, Washington, D.C.: Defense Technical Information Center, pp. 3–67. URL: https://archive.org/details/DTIC_ADA023511/page/n633/mode/2up (visited on 04/13/2020).
- Ripperda, B. et al. (Mar. 15, 2018). “A Comprehensive Comparison of Relativistic Particle Integrators”. In: *The Astrophysical Journal Supplement Series* 235.1, p. 21. ISSN: 1538-4365. DOI: 10.3847/1538-4365/aab114. URL: <https://iopscience.iop.org/article/10.3847/1538-4365/aab114> (visited on 04/13/2020).
- Qin, Hong et al. (Aug. 2013). “Why Is Boris Algorithm so Good?” In: *Physics of Plasmas* 20.8, p. 084503. ISSN: 1070-664X, 1089-7674. DOI: 10.1063/1.4818428. URL: <http://aip.scitation.org/doi/10.1063/1.4818428> (visited on 04/17/2020).

- Micluță-Câmpeanu, Sebastian (2019). "Laser Wakefield Acceleration Studies Using Particle in Cell Method". Bucharest: University of Bucharest. 67 pp. URL: <https://github.com/SebastianM-C/MasterThesis>.
- Golomb, Solomon W. (Mar. 1985). "Proof without Words: A 2×2 Determinant Is the Area of a Parallelogram". In: *Mathematics Magazine* 58.2, pp. 107–107. ISSN: 0025-570X, 1930-0980. DOI: 10.1080/0025570X.1985.11977163. URL: <https://www.tandfonline.com/doi/full/10.1080/0025570X.1985.11977163> (visited on 04/18/2020).
- Weisstein, Eric W. (2020a). *Tangent Space*. URL: <https://mathworld.wolfram.com/TangentSpace.html> (visited on 04/18/2020).
- (2020b). *Symplectic Form*. URL: <https://mathworld.wolfram.com/SymplecticForm.html> (visited on 04/18/2020).
- Rim, Donsub (Mar. 23, 2018). "An Elementary Proof That Symplectic Matrices Have Determinant One". In: arXiv: 1505.04240 [math]. URL: <http://arxiv.org/abs/1505.04240> (visited on 04/19/2020).
- Weisstein, Eric W. (2020c). *Symplectic Map*. URL: <https://mathworld.wolfram.com/SymplecticMap.html> (visited on 04/18/2020).
- Zhang, Mei-Qing and Robert D. Skeel (Mar. 1995). "Symplectic Integrators and the Conservation of Angular Momentum". In: *Journal of Computational Chemistry* 16.3, pp. 365–369. ISSN: 0192-8651, 1096-987X. DOI: 10.1002/jcc.540160309. URL: <http://doi.wiley.com/10.1002/jcc.540160309> (visited on 04/19/2020).
- Hairer, E., Christian Lubich, and Gerhard Wanner (2006). *Geometric Numerical Integration: Structure-Preserving Algorithms for Ordinary Differential Equations*. 2nd ed. Springer Series in Computational Mathematics 31. Berlin ; New York: Springer. 644 pp. ISBN: 978-3-540-30663-4.
- Zhang, Ruili *et al.* (Apr. 2015). "Volume-Preserving Algorithm for Secular Relativistic Dynamics of Charged Particles". In: *Physics of Plasmas* 22.4, p. 044501. ISSN: 1070-664X, 1089-7674. DOI: 10.1063/1.4916570. URL: <http://aip.scitation.org/doi/10.1063/1.4916570> (visited on 04/22/2020).
- Kane Yee (May 1966). "Numerical Solution of Initial Boundary Value Problems Involving Maxwell's Equations in Isotropic Media". In: *IEEE Transactions on Antennas and Propagation* 14.3, pp. 302–307. ISSN: 0018-926X. DOI: 10.1109/TAP.1966.1138693. URL: <http://ieeexplore.ieee.org/document/1138693/> (visited on 04/25/2020).
- Lehe, Remi (June 13–17, 2016a). "Electromagnetic Particle-In-Cell Codes". US Particle Accelerator School (USPAS) Summer School (Lawrence Berkeley National Laboratory (LBNL)). URL: https://people.nscl.msu.edu/~lund/uspas/sbp_2018/lec_em_pic/A1a_EM_PIC.pdf (visited on 04/25/2020).
- (June 13–17, 2016b). "Electromagnetic Wave Propagation in Particle-In-Cell Codes". US Particle Accelerator School (USPAS) Summer School (Lawrence Berkeley National Laboratory (LBNL)). URL: https://people.nscl.msu.edu/~lund/uspas/sbp_2018/lec_em_pic/A1b_EM_Waves.pdf (visited on 04/25/2020).
- Fiuza, F *et al.* (July 1, 2011). "Efficient Modeling of Laser–Plasma Interactions in High Energy Density Scenarios". In: *Plasma Physics and Controlled Fusion* 53.7, p. 074004. ISSN: 0741-3335, 1361-6587. DOI: 10.1088/0741-3335/53/7/074004. URL: <https://iopscience.iop.org/article/10.1088/0741-3335/53/7/074004> (visited on 05/02/2020).
- Cohen, B.I., A.J. Kemp, and L. Divol (June 2010). "Simulation of Laser–Plasma Interactions and Fast-Electron Transport in Inhomogeneous Plasma". In: *Journal of Computational Physics* 229.12, pp. 4591–4612. ISSN: 00219991. DOI: 10.1016/j.jcp.2010.03.001. URL: <https://linkinghub.elsevier.com/retrieve/pii/S002199911000104X> (visited on 05/02/2020).

- Tarentino, A. L. and F. Maley (Nov. 3, 1975). "A Comparison of the Substrate Specificities of Endo-Beta-N-Acetylglucosaminidases from Streptomyces Griseus and Diplococcus Pneumoniae". In: *Biochemical and Biophysical Research Communications* 67.1, pp. 455–462. ISSN: 0006-291X. DOI: 10.1016/0006-291x(75)90337-x. pmid: 1016.
- Vincenti, Henri and Jean-Luc Vay (July 2018). "Ultrahigh-Order Maxwell Solver with Extreme Scalability for Electromagnetic PIC Simulations of Plasmas". In: *Computer Physics Communications* 228, pp. 22–29. ISSN: 00104655. DOI: 10.1016/j.cpc.2018.03.018. URL: <https://linkinghub.elsevier.com/retrieve/pii/S0010465518300900> (visited on 05/02/2020).
- Burau, Heiko *et al.* (Oct. 2010). "PICConGPU: A Fully Relativistic Particle-in-Cell Code for a GPU Cluster". In: *IEEE Transactions on Plasma Science* 38.10, pp. 2831–2839. ISSN: 0093-3813, 1939-9375. DOI: 10.1109/TPS.2010.2064310. URL: <http://ieeexplore.ieee.org/document/5556015/> (visited on 05/02/2020).
- Bennett, Keith *et al.* (n.d.). "Users Manual for the EPOCH PIC Codes". In: (), p. 98.
- Valenta, Petr (2017). "Tight-Focusing of Short Intense Laser Pulses in Particle-in-Cell Simulations of Laser-Plasma Interaction". Master's Thesis. Prague: Czech Technical University. 121 pp. URL: https://github.com/valenpe7/master_thesis (visited on 05/02/2020).
- Wang, T. *et al.* (May 11, 2020). "Power Scaling for Collimated gamma -Ray Beams Generated by Structured Laser-Irradiated Targets and Its Application to Two-Photon Pair Production". In: *Physical Review Applied* 13.5, p. 054024. ISSN: 2331-7019. DOI: 10.1103/PhysRevApplied.13.054024. URL: <https://link.aps.org/doi/10.1103/PhysRevApplied.13.054024> (visited on 06/26/2020).